TECHNISCHE UNIVERSITÄT BERLIN

Cortical Spreading Depression in reaction-diffusion models

vorgelegt von

Diplom–Physikerin Frederike Kneer
geb. in Ostfildern-Ruit

von der Fakultät IV – Elektrotechnik und Informatik
der Technischen Universität Berlin

zur Erlangung des akademischen Grades
Doktor der Naturwissenschaften
- Dr. rer. nat. -
genehmigte Dissertation

Promotionsausschuss
Vorsitzender: Prof. Dr. Manfred Opper
Gutachter: Prof. Dr. Klaus Obermayer
Gutachter: Prof. Dr. Ernest Barreto
Gutachter: Dr. Markus Dahlem

Tag der wissenschaftlichen Aussprache: 10. Juni 2016

Berlin 2016

To do harm to other animals in order to find out how we function is highly questionable.

Acknowledgements

First, I want to express my gratitude to Prof. Klaus Obermayer, the supervisor of this thesis, for giving me the opportunity to work in his Neural Information Processing Group. And I would like to thank all members of the group for creating a relaxed and cheerful working atmosphere.

I am grateful to Markus Dahlem for numerous inspiring discussions, his encouragement and for helpful suggestions on the thesis. Thank you, Markus.

Many thanks to Prof. Ernest Barreto and to Prof. Manfred Opper for agreeing to be members of my reviewing committee.

Finally, I am grateful to my parents for all their support. And a very special thanks goes to Tom. Thank you for being who you are!

Abstract

Cortical Spreading Depression (CSD) is a pathological dysfunction of brain activity that occurs during neurological diseases like e.g. migraine and stroke. In the electrocorticogram, it can be measured as a slowly propagating depression of the signal, which is associated with the depolarization of the neuronal membrane potential involving a redistribution of ions across the cell membrane. Despite substantial progress in the understanding of CSD, both biophysical processes during CSD and external influences on CSD are still incompletely known.

For control of CSD by external neuromodulation, knowledge is required about cellular processes involved in CSD and interference of CSD with external forces. This is of clinical importance because CSD causes transient neurological deficits and subsequently headache (migraine) or permanent brain damage (stroke and brain injury).

In this thesis, we first study cellular processes involved in CSD using an ion-based model (bottom-up approach).

Second, we investigate external forces on CSD in a generic neuronal model (top-down approach).

To get deeper insight in biophysical processes involved in CSD, we carefully develop a biophysical neuron model for CSD that describes transport processes on a tissue level. Therefore, we start from a Hodgkin-Huxley type model including time-dependent ion concentrations. The local model consists of two compartments, a neuron surrounded by a closed extracellular space. The transmembrane currents are assumed to be a combination of gated and leak currents, ion pumps are also included. The model is bistable; besides the physiological resting state a second stable state exists, which is a depolarized state with largely depleted ion gradients. This state characterizes the pathological depolarization during CSD.

We first investigate the robustness of this bistability for changes in strength and dynamics of the gated currents with a bifurcation analysis. We find quantitative changes, however bistability holds in a wide parameter range.

Then, we add a third compartment to the model, the astrocytes. They function as a buffer for excess ions in the extracellular space. This can, with convenient parameter values such as the size of the glial compartment and the amount of ion channels at the glial membrane, change dynamics from bistable to excitable, i.e., excitable with large depletion of ion gradients. In the local system, we identify the parameter range in which the glial buffer deletes bistability. In the monostable system, the depolarized state is transient, the systems recovers to the physiological state after each excitation.

Next, we assume the glial compartment to be a bath. The astrocytes are closely connected to the blood vessels, what gives reason to the approximation that excess ions in the astrocytes are cleared by the vasculature instantaneously. The mathematical advantage of this description, which can be derived by a limit value generation of an infinitely large glial compartment, is that we obtain a model with a reduced number of rate equations. In the reduced model, the buffer function of the astrocytes is increased. In addition, we carefully address the problem of electroneutrality. This is not negligible in this grey matter model including a net flow of ions from one side of the membrane to the other. We find that the particular mathematical description of the membrane potential determines the charge distribution. Analyzing this in detail enables us to identify an appropriate model description that accounts for electroneutrality.

To describe transport processes during CSD and, in particular, to develop hypothesis about when and why ionic homeostasis fails, we develop a spatially continuously extended neuron model. First, we couple the two-compartmental elements consisting of a neuron surrounded by an extracellular space by extracellular diffusing ions in a one-dimensional geometry. Thereby, we pay attention to electroneutral diffusion.

The bistable model spatially coupled by diffusion has propagating front solutions, i.e., solutions that connect the two stable states and propagate with constant shape and velocity.

Next, we add the glial compartment to the spatially extended neuron model. Depending on parameter values, the local elements are bistable or monostable. Analyzing whether lateral diffusion in the extracellular space contributes to relaxation we find that this is not the case. A system consisting of bistable elements spatially coupled by extracellular diffusing ions has propagating front solutions, whereas a system consisting of monostable elements has propagating pulse solutions, i.e., solutions that start and end in the same stable state and propagate with constant shape and velocity.

Next, to model ion movement through glial gap junctions, we also allow for diffusion within the glial compartment. This system has propagating pulse solutions in the whole analyzed parameter regime. The pulse width decreases due to diffusion in the glial compartment, thus our model suggests that gap junctional coupling facilitates relaxation. In addition, we address the in literature contradicting discussed role of neuronal gap junctions. Although assumed to be only rare, our model proposes that they have a strong inhibitory effect on CSD.

Grafstein proposed in 1963 to model front propagation of CSD using a generic one variable reaction-diffusion model (today known as Schlögl model). Although Grafstein's hypothesis has to be modified, the essential view of a reaction-diffusion process still holds.

To describe CSD by an effective model that also allows for analytical approximations, we use an extension of the Schlögl model with a second variable, which is known as the FitzHugh-Nagumo (FHN) model. Thereby, we investigate the role of external influences such as the curvature of the cortex or an externally applied electrical field on CSD.

First, the effect of advection on the propagation of traveling waves in a one-dimensional medium is studied. The advection term can describe an electrical field externally applied parallel to propagation direction and, in addition, advection in a one-dimensional medium is an approximation of the effect of front curvature on wave propagation in a two-dimensional medium.

In particular, the effect of advection on the critical minimal speed of traveling waves is studied. Previous theoretical studies estimated this effect on the velocity of fast waves, a stable stationary propagating solution of FHN model, and predicted the existence of a critical advection strength below which propagating waves are not supported anymore. Here, an analytical expression for the advection-velocity relation of the slow wave, an unstable stationary propagating solution of the FHN model, is derived. Then, the critical advection strength is calculated taking into account the unstable slow wave solution. We also analyze the two-variable reaction-diffusion-advection model numerically in a wide parameter range. Due to the new control parameter (advection) we can find stable wave propagation in the otherwise non-excitable parameter regime, if the advection strength exceeds a critical value. Comparing theoretical predictions to numerical results, we find that they are in good agreement. Theory provides an explanation for the observed behaviour.

Next, to investigate the influence of the geometry of the brain on CSD, we study reaction-diffusion waves on curved two-dimensional surfaces, and determine the influence of curvature upon the nucleation and propagation of spatially localized waves. We show that the stability of propagating wave segments crucially depends on the curvature of the surface. As they propagate, they may shrink to the uniform steady state or expand, depending on whether they are smaller or larger than a critical nucleus. This critical nucleus for wave propagation is modified by the curvature acting like an effective space-dependent local spatial coupling, similar to diffusion, and thus extending the regime of propagating excitation waves beyond the excitation threshold of flat surfaces. In addition, curvature can even change stability of wave segments. In particular, a negative gradient of Gaussian curvature Γ, that occurs, if the open ends of a wave segment, whose center of mass is stored at the outside of a torus surface (positive Γ), point towards the torus inside (negative Γ), allows for stable propagation of localized wave segments remaining unchanged in size and shape or oscillating periodically in size.

Zusammenfassung

Cortical Spreading Depression (CSD) ist eine pathologische Fehlfunktion der Hirnaktivität, die bei neurologischen Erkrankungen wie z.B. Migräne und Schlaganfall auftritt. Im Elektrokortikogramm kann sie als eine langsam propagierende Unterdrückung des Signals gemessen werden. Es kommt zu einer Depolarisation des neuronalen Membranpotentials, das durch eine Umverteilung der Ionen durch die Zellmembran verursacht wird. In den letzten Jahren wurden wesentliche Fortschritte im Wissen über CSD erzielt, dennoch sind sowohl biophysikalische Prozesse als auch äußere Einflüsse, die CSD auslösen können, noch unzureichend bekannt.

Um CSD durch externe Neuromodulation kontrollieren zu können, ist es erforderlich, über die zellulären Vorgänge während CSD und über die Wechselwirkung von CSD mit äußeren Einflüssen Bescheid zu wissen. Dies ist von klinischer Bedeutung, da CSD sowohl vorübergehende neurologische Defizite mit anschließenden Kopfschmerzen (Migräne) als auch dauerhafte Hirnschäden (Schlaganfall und Hirnverletzung) verursachen kann.

In dieser Arbeit haben wir zunächst mit Hilfe eines biophysikalischen Modells mit dynamischen Ionenkonzentrationen zelluläre Vorgänge untersucht, die an CSD beteiligt sind (Bottom-up-Ansatz).

Dann haben wir mit Hilfe eines generischen neuronalen Modells untersucht, wie äußere Kräfte auf CSD wirken (Top-Down-Ansatz).

Um mehr über die biophysikalischen Prozesse, die an CSD beteiligt sind, herauszufinden, entwickeln wir ein biophysikalisches Neuronenmodell für CSD, das Transportprozesse auf Gewebeniveau beschreibt. Dazu starten wir von einer Erweiterung des Hodgkin-Huxley-Modells mit zeitabhängigen Ionenkonzentrationen. Das lokale Modell besteht aus zwei Kompartiments, einem Neuron umgeben von einem geschlossenen extrazellulären Raum. Die Transmembranströme sind eine Kombination aus spannungsabhängigen Strömen und Leckströmen, Ionenpumpen sind ebenfalls enthalten. Dieses Modell ist bistabil; neben dem physiologischen Ruhezustand hat es einen zweiten stabilen Zustand mit depolarisiertem Membranpotential und weitgehend erschöpften Ionengradienten. Dieser Zustand beschreibt die pathologische Depolarisation während CSD.

Nach einer kurzen Einführung des Modells untersuchen wir, ob die Bistabilität eine robuste Eigenschaft des Systems ist. Dazu führen wir unter Variation der Stärke und Dynamik der spannungsabhängigen Ströme eine Bifurkationsanalyse durch. Trotz quantitativer Unterschiede bleibt die Bistabilität in einem weiten Parameterbereich erhalten. Dann fügen wir dem Modell ein drittes Kompartiment hinzu, die Astrozyten. Sie können überschüssige Ionen aus dem extrazellulären Raum aufnehmen. Durch die Variation von Parametern wie der Größe der Astrozyten und der Anzahl an Iononkanälen durch die Astrozytenmembran lässt sich die Dynamik des Systems von bistabil zu monostabil ändern. Das monostabile System ist anregbar. Nach einer geeigneten Anregung kommt es, bevor das physiologische Gleichgewicht wiederhergestellt wird, zu einer transienten Depolarisation des neuronalen Membranpotentials, das durch eine starke Abnahme der Ionengradienten verursacht wird. Wir bestimmen den Parameterbereicht, in dem der Ionenaustausch zwischen Extrazellulärraum und Astrozyten die Bistabilität aufhebt.

Als nächstes beschreiben wir die Astrozyten als Bad. Diese Näherung wird mit der Annahme begründet, dass überschüssige Ionen in den Astrozyten schnell von den Blutgefäßen, die direkt mit den Astrozyten verbunden sind, aufgenommen werden. Mathematisch entspricht diese Beschreibung dem Grenzwert unendlich großer Gliazellen. In dem nun bezüglich der Anzahl an Ratengleichungen reduzierten Modell wird das physiologische Gleichgewicht nach einer Störung schneller wiederhergestellt.

Bei der Entwicklung des Modells brücksichtigen wir das Problem der Elektroneutralität. Da wir ein Modell der grauen Substanz entwickeln, das einen Ionen-Fluss durch die Membran beschreibt, darf dies nicht vernachlässigt werden. Wir zeigen, dass die hier gewählte mathematische Bechreibung des Membranpotentials die Ladungsverteilung beeinflusst. Durch eine detaillierte Untersuchung dieses Zusammenhangs finden wir eine geeignete Beschreibung, die Elektroneutralität gewährleistet.

Ausserdem entwickeln wir ein räumlich ausgedehntes neuronales Modell. Damit wollen wir Transportprozesse während CSD beschreiben, um herauszufinden, wann Ionenhomöostase gewährleistet ist und wann nicht.

Als erstes koppeln wir neuronale Elemente, die aus zwei Kompartiments, Neuronen und einem Extrazellulärraum, bestehen, durch Ionendiffusion im Extrazellulärraum Ionendiffusion. Auch hier achten wir auf Elektroneutralität, durch eine elektroneutrale Beschreibung des diffusiven Ionenflusses ist diese gewährleistet. Durch die diffusive Kopplung bistabiler Elemente erhalten wir ein Medium, das Frontlösungen hat. Das sind Wellen, die die beiden stabilen Zustände verbinden und sich mit konstanter Geschwindigkeit und Form fortbewegen.

Als nächstes koppeln wir neuronale Elemente bestehend aus drei Kompartimenten, Neuronen, Astrozyten und einem Extrazellulärraum, wieder durch Diffusion im Extrazellulärraum. Je nach Parameterwahl sind die lokalen Elemente bistabil oder monostabil. Uns interessiert es, ob laterale Diffusion im Extrazellulärraum zur Ionenhomöostase

beiträgt. Wir stellen fest, dass dies nicht der Fall ist. Ein Medium bestehend aus bistabilen Elementen hat Frontlösungen, wohingegen ein Medium bestehend aus monostabilen Elementen Pulslösungen hat, also Lösungen, die im gleichen stabilen Zustand starten und enden und sich mit konstanter Form und Geschwindigkeit fortbewegen.
Da die Astrozyten durch Gap Junctions miteinander verbunden sind, haben wir auch den Einfluss von Ionendiffusion innerhalb des Gliakompartiments auf CSD untersucht. Im gesamten von uns untersuchten Parameterbereich hat dieses Medium Pulslösungen. Die Pulsbreite hängt dabei von der Stärke der Diffusion im Gliakompartiment ab. In unserem Modell trägt also der Ionenfluss durch Gap Junctions zur Ionenhomöostase bei.
Desweiteren haben wir den in der Literatur widersprüchlich diskutierten Einfluss von neuronalen Gap Junctions auf CSD untersucht. Es gibt zwar nur eine geringe Anzahl an Gap Junctions zwischen den Neuronen, dennoch ist ihre inhibitorische Wirkung auf CSD in unserem Modell beträchtlich.

Im Jahr 1963 schlug Grafstein vor, die Frontpropagation von CSD mit einem generischen Reaktions-Diffusionsmodell mit nur einer Variablen zu beschreiben. Heute ist dieses Modell als Schlögl-Modell bekannt. Grafsteins Hypothese muss zwar modifiziert werden, der wesentliche Bestandteil aber, nämlich die Beschreibung von CSD als Reaktions-Diffusionsprozess, ist noch gültig.
Um CSD mit einem geeigneten Modell zu beschreiben, das auch analytische Näherungen zulässt, verwenden wir eine Erweiterung des Schlögl Modells mit einer zweiten Variablen, das FitzHugh-Nagumo (FHN) Modell. Dies ermöglicht es uns, die Wirkung äußerer Einflüsse wie der Krümmung des Kortex oder eines extern angelegten elektrischen Felds auf CSD zu untersuchen.
Zunächst untersuchen wir den Einfluss von Advektion auf die Propagation von Wellen in einem eindimensionalen Medium. Der Advektionsterm kann ein elektrisches Feld beschreiben, das extern parallel zur Propagationsrichtung angelegt ist. Ausserdem beschreibt Advektion in einem räumlich eindimensionalen Medium näherungsweise den Einfluss der Krümmung der Wellenfront in einem räumlich zweidimensionalen Medium auf die Wellenpropagation. Insbesondere wird der Einfluss von Advektion auf die kritische minimale Geschwindigkeit von sogenannten *traveling waves* untersucht. Bisherige theoretische Arbeiten haben den Einfluss von Advektion auf die Geschwindigkeit der *fast waves*, einer stabilen stationär propagierenden Lösung des FHN Modells, näherungsweise berechnet und haben gezeigt, dass es eine kritische Advektionsstärke gibt, unterhalb von der keine stabile Wellenpropagtion möglich ist.
Hier leiten wir einen analytischen Ausdruck her, der den Einfluss von Advektion auf die Geschwindigkeit der *slow waves*, einer instabilen stationär propagierenden Lösung des FHN Modells, beschreibt. Dann berechnen wir unter Berücksichtigung der *slow waves* die kritische Advektionsstärke.

Ausserdem untersuchen wir das Reaktions-Diffusions-Advektionsmodell in einem großen Parameterbereich numerisch. Der neue Kontrollparameter (Advektion) ermöglicht stabile Wellenpropagation im sonst nicht anregbaren Parameterbereich, wenn die Advektionsstärke einen kritischen Wert übersteigt. Die theoretischen Vorhersagen und die numerischen Ergebnisse stimmen überein. Die Theorie liefert eine Erklärung für das numerisch beobachtete Verhalten.

Als nächstes untersuchen wir den Einfluss der Geometrie des Gehirns auf CSD. Wir untersuchen Wellen auf gekrümmten zweidimensionalen Flächen und bestimmen den Einfluss der Krümmung auf Keimbildung und Propagation räumlich begrenzter Wellensegmente. Wir zeigen, dass die Stabilität von Wellensegmenten maßgeblich von der Krümmung der Fläche abhängt.

Lokalisierte Wellensegmente können zum homogenen Grundzustand abklingen oder sich ausdehnen, je nachdem, ob sie kleiner oder größer als der kritische Nukleus sind. Die Größe des kritischen Nukleus hängt von der Krümmung der Fläche ab. Die Krümmung der Fläche gleicht mathematisch einer effektiv ortsabhängigen räumlichen Kopplung ähnlich der Diffusion. Damit lässt sich erklären, warum auf gekrümmten Flächen der Parameterbereich, in dem Wellenpropagation möglich ist, im Verhältnis zu ungekrümmten Flächen verschoben ist.

Ausserdem beeinflusst die Krümmung die Stabilität von Wellensegmenten. Ein negativer Gradient der Gaußschen Krümmung Γ, der auftritt, wenn die offenen Enden eines Wellensegments, dessen Schwerpunkt auf der Außenseite eines Torus (negatives Γ) liegt, richtung Torusinnenseite (positives Γ) ragen, kann lokalisierte Wellensegmente stabilisieren. Diese propagieren dann mit konstanter Form und Größe oder mit periodisch oszillierender Größe.

List of Publications

- F. Kneer, E. Schöll, and M. A. Dahlem. Nucleation of reaction-diffusion waves on curved surfaces. *New J. Phys.*, 16:053010, 2014.
- F. Kneer, K. Obermayer, and M. A. Dahlem. Analyzing critical propagation in a reaction-diffusion-advection model using unstable slow waves. *Eur. Phys. J. E*, 38:10, 2015.
- M. A. Dahlem, B. Schmidt, I. Bojak, S. Boie, F. Kneer, N. Hadjikhani, and J. Kurths. Cortical hot spots and labyrinths: why cortical neuromodulation for episodic migraine with aura should be personalized. *Front. Comp. Neurosci.*, 9:29, 2015.

Contents

Acknowledgements **i**

Abstract (English/Deutsch) **iii**

List of Publications **xi**

Contents **xiii**

1 Introduction **1**
- 1.1 Cortical Spreading Depression 1
- 1.2 Motivation 2
- 1.3 Overview of mathematical neuron models 2
- 1.4 Cellular processes during Cortical Spreading Depression 4
- 1.5 External influences on Cortical Spreading Depression 6
- 1.6 Structure of the thesis 8

2 Local dynamics of a biophysically detailed neuron model **11**
- 2.1 Bistable two-compartmental ion-based model 12
- 2.2 Robustness of the phase space structure 18
  - 2.2.1 Varying strength of gated currents 20
  - 2.2.2 Varying dynamics of gated currents 21
- 2.3 Membrane potential and electroneutrality 24
- 2.4 Glial buffer 28
  - 2.4.1 Three-compartmental ion-based model including glia cells 29
  - 2.4.2 Dynamics of the three-compartmental model 31
  - 2.4.3 Modeling glia cells as a bath 35
  - 2.4.4 Examples of time course during relaxation 37
- 2.5 Conclusion 41

3 A biophysically detailed reaction-diffusion model **43**
- 3.1 Diffusive spatial coupling of bistable two-compartmental elements 44
  - 3.1.1 Electroneutrality 46
    - 3.1.1.1 Electroneutral transmembrane currents 46
    - 3.1.1.2 Electroneutral lateral currents 50
- 3.2 Diffusive spatial coupling of three-compartmental elements 53

3.2.1 Ion movement in the extracellular space . . . 53
3.2.2 Glial gap junctions . . . 55
3.2.3 Glial bath in the reaction-diffusion model . . . 57
3.2.4 Electroneutrality . . . 60
3.3 Neuronal gap junctions . . . 60
3.4 Conclusion . . . 63

4 A generic neuronal model 67
4.1 FitzHugh-Nagumo equations . . . 67
4.2 Comparing the FitzHugh-Nagumo and the biophysically detailed model . 70
4.3 Inhomogeneous solutions in the FitzHugh-Nagumo model . . . 72

5 Critical properties of reaction-diffusion waves in one spatial dimension 75
5.1 Differential Advection . . . 76
5.2 Propagation boundary . . . 78
5.3 Advection-velocity relation of the fast and slow wave solution . . . 79
5.4 Critical velocity and critical advection strength . . . 80
5.5 Numerical validation . . . 82
5.6 Conclusion . . . 85

6 Nucleation of reaction-diffusion waves on curved surfaces 87
6.1 Methods . . . 87
6.2 Overview of wave solutions on a torus . . . 90
6.3 Ring wave break-up at saddle-node bifurcation . . . 94
6.4 Curvature-induced changes of nucleation . . . 96
6.4.1 Nucleation on the torus inside . . . 96
6.4.2 Nucleation on the torus outside . . . 97
6.5 Curvature-induced stabilisation . . . 98
6.6 Asymmetric solutions on a torus . . . 101
6.7 Conclusion . . . 103

7 Discussion 105

Bibliography 109

Appendix 117
A.1 1D description of curved 2D waves . . . 119
A.2 Critical advection strength derived from nonlinear Eikonal equation . . . 119
A.3 Calculating $c^f|_{A=0}$ and $c^s|_{A=0}$ using a singular perturbation theory . . . 120
A.3.1 Fast wave velocity $c^f|_{A=0}$ . . . 120
A.3.2 Slow wave velocity $c^s|_{A=0}$ . . . 122
A.4 Toroidal coordinates . . . 123

Chapter 1

Introduction

1.1 Cortical Spreading Depression

Cortical spreading depression (CSD) is a temporary but massive perturbation in the cortical ionic homeostasis leading to a depression of neuronal activity that spreads through the cortex and other grey matter regions in brain. CSD is an emergent phenomenon arising from the interaction of local nonlinear processes in grey matter. Neural and glial compartments, the extracellular space and the vasculature play a role in CSD.

In functional magnetic resonance imaging (fMRI) or electrocorticography (ECoG), CSD can be measured. It is associated with a voltage variation, that peaks after several seconds and is accompied by a huge rise in the extracellular potassium concentration and a massive decrease in the extracellular concentrations of sodium and chloride [1]. The fast depolarization is followed by a much slower recovery process taking up to minutes during which ion gradients are re-established towards their physiological values. The massive ionic perturbation clearly distinguishes CSD from all other brain states such as epileptic seizure activity, functional activation or the physiological resting state. The sequence of ionic perturbation and its recovery spreads with a velocity of about 0.03 - 0.1 mm/s over cortical regions.

CSD is closely related to migraine with aura, stroke and brain injuries [2]. During migraine aura, it spreads as a localized wave segment over an area of several centimeters. In stroke, CSD starts near the infarct core and then circles it. Re-entrant SD waves are believed to have the potential to worsen outcome in incremental steps with each wave circling near the infarct core, but could also have some beneficial component by stimulating blood flow in the penumbra zone far from the infarct tissue [3].

1.2 Motivation

Brain function is the collective result of a huge number of mechanisms ranging from processes at the cellular level like ion movement across the neuronal and glial membrane over interactions of neurons by synaptic connections, gap junctional coupling and diffusion of ions in the interstitial space to macroscopic properties of the brain like the curvature of the cortex. The interaction of many components and mechanisms is necessary for normal brain activity.

CSD is a pathological dysfunction of brain activity affecting an area of several square centimeters of grey matter. Despite substantial progress in the understanding of CSD, both biophysical processes during CSD and external influences on CSD are still incompletely known. However, knowledge about cellular processes involved in CSD and interference of CSD with external forces is of great relevance, not only for comprising the functionality of the human brain, but also for developing novel future therapies for this pathological states.

Computational neuroscience complements clinical neuroscience in providing the opportunity to isolate specific mechanisms that are believed to be relevant for normal brain function. Simulations and analytical insights help us to understand the nervous system in both health and disease. Here, to get deeper insight in biophysical processes involved in CSD, we carefully develop a biophysical neuron model for CSD that describes transport processes on a tissue level. In addition, to describe CSD by an effective model that also allows for analytical approximations, we use an extension of the Schlögl model with a second variable, which is also known as the FitzHugh-Nagumo model [4, 5]. Thereby, we can investigate the role of external influences, such as the curvature of the cortex or an externally applied electrical field, on CSD.

1.3 Overview of mathematical neuron models

The earliest mathematical model for electrically excitable living cells was proposed by Hodgkin and Huxley in a series of papers in 1952 [6–10]. They describe the generation and propagation of action potentials in the squid giant axon. Their model is based on the approach that the neuronal membrane can be described as a capacitor, the nonlinear conductance dynamics are achieved by voltage-gated ion channels. Originally, the ionic species considered in the Hodgkin-Huxley (HH) model are sodium and potassium. However, all kinds of ion channels can be incorporated into such a model scheme.

In the following, especially many HH-based cardiac models were developed [11–13]. The application to cortical dynamics was first mostly indirect by using the approximative FHN model [4, 5], which is a mathematical reduction of the HH model to two dynamical variables. As in the second part of this thesis, macroscopic properties of CSD are analyzed with this approach, the FHN model is discussed in detail later, Sect. 1.5. Another HH-related model has to be mentioned, the Morris-Lecar model [14]. It is a two-variable excitation model with two non-inactivating voltage-sensitive conductances. The original form of the model employed an instantaneously responding voltage-sensitive calcium conductance for excitation and a delayed voltage-dependent potassium conductance for recovery. As the FHN model, it became very popular in neuronal network modeling. Modeling cortical dynamics with the biophysical HH ansatz, it has to be considered that mammalian neurons are more complex than the squid giant axon in both, the variety of ion channels and morphology [15]. Based on the work of Traub [16, 17], biophysically more detailed models, that contain those ion channels, received an increasing attention since the late 1990s.

CSD is a massive perturbation of ionic homeostasis. Thus to model CSD, biophysical models based on HH formalism have to be extended including time-dependent ion concentrations inside and outside the cells. Ion dynamics in HH-like models were first studied in cardiac models [12]. On cortical models, this was for the first time applied in 2000 by Kager, Wadman and Somjen [18]. They proposed a very detailed model for a single hippocampal pyramidal neuron surrounded by a restricted interstitial space. The neuron consists of several compartments, it contains the neuronal soma and spatially complex apical and basal dendrite branches. In addition, for each neuronal compartment, the ion channels of sodium, potassium and chloride are adapted. The Nernst potential of an independent leak current, here interpreted as the chloride current, is fixed at -70mV. This makes sure that the model only has a single stable state, the physiological state with a depolarized membrane potential. This model reproduces CSD very well [18–21].

The effect of cortical ion dynamics was in the following studied by Barreto, Cressman at al. in a model for epileptoform bursting modulation. They used a much simpler HH-like description that neglects morphological details and only contains the classical HH channels [22, 23].

In 2014, Hübel, Schöll and Dahlem designed a model for CSD based on the same ansatz [24]. Their ion-based model consists of a single point neuron surrounded by a restricted extracellular space. The transmembrane currents of the considered ions, sodium, potassium and chloride, are HH-type. The Nernst potential of each ionic species is dynamic. This is physically consequent, as especially during CSD, the intra- and extracellular ion concentrations are massively perturbed. They found, that this minor change results in a different phase space structure, namely the model provides bistable dynamics. Besides the physiological state, there exists a second stable state, which is much less polarized due to a massive depletion of ion gradients. This state characterizes the depolarization during CSD.

In parallel, also mathematical model approaches for CSD in spatially extended systems were developed since the 1960s. The first model that describes propagation of CSD was proposed by Grafstein in 1963 [25]. She used a one-variable reaction-diffusion model, today known as Schlögl model, which equals the activator equation of the FHN model. The local potassium release by the neurons is mimiced by a cubic rate function, what provides bistability. The spatial coupling of the local elements is given by diffusing potassium. The system consisting of bistable elements has propagating front solutions, that connect the two stable states.

A model of CSD propagating in cortical neuronal structures that is based more directly on biophysical quantities was developed by Tuckwell and Miura in 1978 [26]. Movement of potassium and calcium across the neuronal membrane is introduced by leak, gated and pump currents and, in addition, ion diffusion in the ECS is considered. The transmembrane currents are composed such that the model has a single stable fixed point. Their model has *solitary traveling wave solutions*, i.e., pulses that start and end in the single stable state and propagate with constant shape and velocity.

A model based on the same principles was composed by Huang, Miura and Yao in 2011 [27, 28]. They coupled excitable elements consisting of two single point compartments, a neuron surrounded by a an extracellular space [27] based on the work of Kager, Wadman and Somjen [18–21], by extracellular diffusing ions. The main difference to the model proposed by Tuckwell and Miura [26] is that they include a fuller repertoire of transmembrane ionic currents, namely sodium, potassium and chloride currents. The stable stationary propagating solution (waves that propagate with constant velocity and constant shape) of the model consisting of monostable elements spatially coupled by diffusion also are *solitary traveling wave solutions.*

1.4 Cellular processes during Cortical Spreading Depression

The function of a single neuron and the interaction of ensembles of neurons depend very sensitively on the interplay of cellular processes such as the ability of ion movement across the neuronal and glial membrane, clearance of excess ions by the vasculature and lateral diffusion in the extracellular space and through neuronal and glial gap junctions. The ability of a neuron to produce voltage spikes depends very sensitively on the ion concentration in the microenvironment of the cell. In this thesis, we carefully develop a biophysical mathematical model, that allows us to systematically include or leave out the different mechanisms that are believed to be relevant for ionic homeostasis. We can thereby evaluate the importance of the specific processes and in particular develop hypotheses about when and why ionic homeostasis fails.

Our model is based on a work of Hübel, Schöll and Dahlem [24]. Their local model representing a neuron surrounded by an extracellular space is a modification of the model proposed by Barreto, Cressman et al. [22, 23]. Three ionic species are considered, sodium, potassium and chloride. The transmembrane currents considered are gated, leak and pump currents. The model has bistable dynamics. Besides the physiological depolarized state, it has a second stable state. To large a perturbation, as it occurs under extreme conditions like CSD, results in a less polarized state with largely depleted ion gradients. Thus, after a super-threshold excitation, the system remains in the less polarized state and does not recover to the physiological state any more.

During anoxic depolarization, which is a progressive and uncontrollable depolarization of neurons during stroke or brain ischemia, this behaviour has been observed. The depolarization during CSD, however, usually recovers after a time of about 100 s. Recovery was long believed to be due to the pumps only, as with anoxic brain injury, the supply of energy to drive the pumps is lost. The model from [24] proposes that homeostasis cannot rely on the pumps alone, but an additional mechanism is needed.

In the first part of this thesis, we discuss, which mechanisms this might be. First, the clearance of excess ions from the extracellular space by the glia cell is analyzed in the local system. Then, in a spatially extended system, we investigate whether lateral diffusion of excess ions contributes to ionic homeostasis. Therefore, we propose the to our knowledge first three-compartmental ion-based model for CSD consisting of neurons, an extracellular space and astrocytes. Gated and leak currents crossing the astrocytic membrane are considered. We find that ion uptake by glia cells can change system dynamics from bistable to excitable. In addition, we propose a simplified description of the glia cells, namely to assume them to be a bath. This implies, that clearance of excess ions within the glial syncytium is approximated to happen instantaneously, what can be interpreted as the fast uptake of ions by the vasculature. We find that in this open system, the physiological equilibrium is the single stable state and relaxation time is shortened.

In addition, to analyze whether lateral currents contribute to ionic homeostasis, we carefully develop a spatially continuously extended ion-based model for CSD. To model the spatial coupling between the neuronal elements, we pick up the idea of modeling the brain-cell microenvironment as porous medium [26, 28], i.e., the spatial coupling is assumed to be due to diffusing ions. Previous ion-based reaction-diffusion models for CSD have been proposed, i.e., monostable excitable elements consisting of two single point compartments were spatially coupled by extracellular diffusing ions [26–28]. The stable stationary propagating solution of this systems are pulses.

The single elements of our model consist of three compartments, a neuron and an astrocyte surrounded by an extracellular space. Depending on the properties of the astrocytic compartment, the local elements are bistable or excitable. This enables us to identify the role of lateral diffusive currents in buffering excess ions from the extracellular space.

The effect of gap junctions on CSD is widely unknown. Here, we analyze if they are relevant for ionic homeostasis. Therefore, we consider all, extracellular diffusing ions, ions diffusing through gap junctions in the glial syncytium and, in addition, ions diffusing through neuronal gap junctions. Furthermore, we carefully address the problem of electroneutrality in our grey matter model. First, electroneutrality of the transmembrane currents is discussed, a model description that ensures electroneutral transmembrane currents is identified. Second, analyzing diffusing charged particles, the electrical forces among them cannot be neglected. To our knowledge, the only work that deals with this topic in spatially extended models for CSD is from Mori from 2014 [29]. He follows a formalism for electroneutral diffusion proposed by Rubinstein in 1990 [30]. We resume this and discuss other possibilities to achieve electroneutral lateral currents.

In the neuronal medium, the type of inhomogeneous solutions reflect whether ionic homeostasis holds. If ionic homeostasis completely fails, an excitation spreads over the medium as a front. A functional buffer mechanism manages to recover a propagating depolarization after a period of depolarization to ionic homeostasis. This behaviour is reflected by pulses. However, in healthy brain, permanent ionic homeostasis (aside from fluctuations due to normal neuronal activity) is desired. Thus an inhibitory mechanism that prevents propagation of excitations is needed.

1.5 External influences on Cortical Spreading Depression

In addition to the biophysical processes explicitly described by the ion-based HH-type model, we are interested in the influence of external forces such as the geometry of the brain or an externally applied electrical field on CSD.

As there is clinical evidence that spatially localized wave segments play a dominant role in CSD [3], we aim at investigating them. In general, spatially localized wave segments, as they propagate, may shrink, expand or remain unchanged in size and shape, in which case they are called *particle-like waves* [31]. Spatially localized wave segments also represent critical structures which can be stabilized by global feedback [32–34]. They play an important role for the nucleation of propagating waves and wave segments in 2D spatial domains. Generally, waves can be controlled by feedback control. This is a robust and versatile concept which uses the internal dynamics of the system to generate a control signal which directs the system towards desired dynamics. A lot of examples are provided by global or nonlocal and in some cases time-delayed feedback control of wave propagation in reaction-diffusion systems [35–41]. On the other hand, the curvature of the medium itself also provides a means of internal control of the stability, as we will show in this thesis.

Most previous studies have focused on wave propagation in planar spatial domains, yet there is also a considerable body of work on reaction-diffusion waves in curved surfaces, mostly on spirals and ring waves [42–50], but not to the best of our knowlege on nucleation. The cortex, however, represents a strongly curved surface. It is our purpose to study nucleation and propagation of wave segments on curved 2D surfaces. We demonstrate that positive or negative Gaussian curvature of the spatial domain has a dramatically different effect upon the wave dynamics.

Furthermore, as small curvature of a wave front in 2D reaction-diffusion media can under some approximations result in a reduced reaction-diffusion-advection description in one dimension [51–53], we analyze critical properties of traveling waves in a spatially 1D excitable medium.

Generic features of reaction-diffusion-advection models have been subject to detailed mathematical analysis, e.g., conditions for the existence, uniqueness and asymptotic stability of time periodic traveling wave solutions have been found [54], and the influence of nonlocal coupling on dynamics of reaction-diffusion-advection systems has been analyzed [55–58]. Besides, critical properties of traveling waves affected by advection have been discussed [49, 51, 52]. It has been shown, that advection can have destructive and constructive effects on traveling waves, namely slowing them down and annihilate them at a critical speed, and accelerating them [51].

Here, we show that in the non-excitable parameter regime, which does not support traveling waves, advection can even induce stable propagation. We provide an analytical approximation for the effect of advection on the critical propagation velocity, i.e., the minimal possible velocity for stable wave propagation, and compare our results to numerical simulations.

As a model for traveling waves in one spatial dimension and for localized wave segments on a curved 2D surface, we consider excitable media of activator-inhibitor type. FHN dynamics are chosen, as they provide a mathematically tractable excitable medium of activator-inhibitor type. The FHN model is based on a modification of the *van der Pol oscillator* [59], i.e., an oscillator with non-linear damping that describes voltage dynamics in an electrical circuit. The FHN model was first suggested by FitzHugh in 1961 [4], who called it *Bonhoeffer-van der Pol oscillator* [60, 61], and independently by Nagumo et al. in 1962 [5]. By adding a driving current, they created a model for the action potential.

The FHN model became extremely popular in modeling several physiological systems, e.g., models of the heart [62, 63], of the muscle [62, 63] and especially spatially extended network models for cortical activity [64–66] can be found. In addition, FHN equations are a favorite model for the study of excitability. It also was suggested to describe the fundamentally different ionic excitability of neuronal tissue causal for CSD [24, 67].

1.6 Structure of the thesis

This thesis is mainly divided into two parts. First, cellular processes involved in CSD are studied in an ion-based model, Chapt. 2 and Chapt. 3. Second, a generic neuronal model is proposed, Chapt. 4, and external forces on CSD in this simplified description are investigated, Chapt. 5 and Chapt. 6.

In particular, in Chapt. 2, we introduce the local three-compartmental ion-based neuron model. First, the bistable HH-type ion-based model consisting of neurons surrounded by a closed extracellular space proposed in [24] is reviewed. Then, as in literature exists a huge variety of HH parameter values, we show that the phase space structure of the bistable model is quite robust under changes of this parameter values. In the two-compartmental closed system, electroneutrality holds due to mass conservation. We discuss a modification we will make to ensure, that electroneutrality also holds in open systems. Next, glia cells crucial for buffering excess ions from the extracellular space are introduced. Thereby, we carefully discuss, under which conditions they manage to maintain ionic homeostasis in a closed local element.

In Chapt. 3, a spatial 1D neuronal model describing cellular processes on a tissue level is designed. Therefore, the three-compartmental elements are spatially coupled by the assumption of diffusing ions. Diffusive fluxes are described electroneutral. We show that it depends on the strength of the particular transmembrane and diffusive currents whether after an excitation recovery to the physiological equilibrium can be achieved.

The second part of the thesis is structured as follows. In Chapt. 4, FHN equations are introduced, local dynamics are reviewed. Using the FHN system as a model for CSD, we analyze, whether, unless it does not allow for a direct interpretation in terms of ion channels, it captures the threshold and excitation properties of the biophysical ion-based model.

In Chapt. 5, the effect of advection on the propagation of traveling waves in one spatial dimension is studied. In particular, an analytical approximation for the effect of advection on the critical minimal speed, below which no stable wave propagation is possible, is found. Therefore, first the advection-velocity relation of the two traveling wave solutions of the FHN model, the stable fast wave and the unstable slow wave, is derived. Theoretical predictions are compared to numerical results.

Then, the generic reaction-diffusion system is extended to curved 2D surfaces, Chapt. 6. Primary focus of this investigation is the influence of the curvature upon the nucleation and propagation of spatially localized waves. We realize the geometry of the excitable medium by a torus as it provides both, positive and negative Gaussian curvature. We discuss wave solutions on a torus. We consider ring-shaped autowaves, wave segments and unstable structures such as particle-like waves (critical nuclei) stabilized by feedback control. Specifically, we study curvature-induced changes of nucleation and curvature-induced stabilization of wave segments. The critical propagation effects calculated in Chapt. 5 are numerically analyzed in two spatial dimensions with the help of ring-shaped autowaves, that break up if their geodetic curvature exceeds a critical value. Furthermore, critical propagation effects provide an explanation of the observed curvature-induced stabilisation. In addition, we show that curvature can induce a massive change of lifetime of unstable structures.

In Chapt. 7, we conclude the thesis with a brief summary and an outlook on future research projects that may follow our here presented results.

Chapter 2

Local dynamics of a biophysically detailed neuron model

In this Chapter, a biophysically detailed local model for CSD is designed. The system has time-dependent ion concentrations and consists of three compartments, a neuron (NCS) and an astrocyte (ACS) surrounded by a closed extracellular space (ECS). The model is based on the ion-based HH-type model proposed in [24], that consists of two compartments, a single point neuron surrounded by a closed extracellular space.

First, in Sect. 2.1, the two-compartmental model is reviewed. As shown in [24], the model is bistable; besides the physiological resting state it has a second stable state, a depolarized state with largely depleted ion gradients. This state characterizes the pathological depolarization during CSD.

In literature, we find a huge variety of biologically plausible parameter values of the HH model. However, slight variations in the parameter values might cause completely different dynamics if a bifurcation is passed. Thus, in Sect. 2.2, we analyze whether the bistability is robust under variations of the parameter values.

The transmembrane currents of the closed system are electroneutral. This is ensured by the mathematical description of the membrane potential. However, if ion exchange with the surrounding is considered, electroneutrality can be violated. In Sect. 2.3, we discuss, how the model equations, in detail the mathematical description of the membrane potential at both, the neuron and the astrocyte, have to be set up to ensure electroneutrality in open systems.

The bistability of the two-compartmental model gives reason to the assumption that ion pumps alone are not sufficient for ionic homostasis, but an additional mechanism is needed. This might be the uptake of excess ions from the extracellular space by astrocytes. To model this, in Sect. 2.4.1, a third compartment is added to the system, the astrocytes. Leak and pump currents crossing the astrocytic membrane are considered. In Sect. 2.4.2, we analyze, under which conditions this glial buffer manages to recover the system from the depolarized state to the polarized equilibrium. In addition, in Sect. 2.4.3, we propose an open system, namely to model the glia cells as a bath. This limit of infinitely large astrocytes is motivated by the fast clearance of excess charges in the astrocytes by the vasculature and by diffusion within the glial syncytium. Last, in Sect. 2.4.4, we show some examples of the temporal evolution of the membrane potential and the ion concentrations in the particular compartments during relaxation.

2.1 Bistable two-compartmental ion-based model

In [24], an extension of the HH model including explicit expressions for intra- and extracellular ion dynamics is proposed to describe local dynamics of CSD. The original HH model [10] reads

$$
\begin{aligned}
\frac{\partial V_m^n}{\partial t} &= -\frac{1}{C_m}(I_{Na} + I_K + I_{leak} - I_{app}), && (2.1)\\
\frac{\partial n}{\partial t} &= \frac{n_\infty - n}{\tau_n}, && (2.2)\\
\frac{\partial h}{\partial t} &= \frac{h_\infty - h}{\tau_h}, && (2.3)\\
\frac{\partial m}{\partial t} &= \frac{m_\infty - m}{\tau_m}. && (2.4)\\
& && (2.5)
\end{aligned}
$$

The first equation states, according to Kirchhoff's current law, that the excess charge is stored on the membrane capacitor with capacitance C_m and potential V_m^n. I_{Na} and I_K are the gated sodium and potassium current, I_{leak} a leak current that is carried by unspecific ions and I_{app} is an externally applied current. The other rate equations give the dynamics of the gating variables, the potassium activator n, the sodium inactivator h and the sodium activator m. The asymptotic values x_∞ and the relaxation times τ_x are given by

$$
\begin{aligned}
x_\infty &= \frac{\alpha_x}{\alpha_x + \beta_x}, && (2.6)\\
\tau_x &= \frac{1}{\alpha_x + \beta_x}, && (2.7)
\end{aligned}
$$

with x being n, m or h.

Throughout this thesis, α_x and β_x are chosen according to [24],

$$\begin{aligned}
\alpha_m &= \frac{0.3(V_m^n+30)}{1-\exp\left(-(V_m^n+30)/10\right)}, && (2.8)\\
\beta_m &= 12\,\exp\left(-(V_m^n+30)/10\right), && (2.9)\\
\alpha_n &= \frac{0.03(V_m^n+34)}{1-\exp\left(-(V_m^n+34)/10\right)}, && (2.10)\\
\beta_n &= 0.375\,\exp\left(-(V_m^n+44)/80\right), && (2.11)\\
\alpha_h &= 0.21\,\exp\left(-(V_m^n+44)/20\right), && (2.12)\\
\beta_h &= \frac{3}{1+\exp\left(-(V_m^n+14)/10\right)}. && (2.13)
\end{aligned}$$

In the HH model, the transmembrane ionic currents are a combination of gated and leak currents, whereat the gated currents are specifically calculated for each ionic species (i.e., for sodium and potassium),

$$\begin{aligned}
I_{Na}^g &= g_{Na}^g m^3 h\cdot(V_m^n - E_{Na}), && (2.14)\\
I_K^g &= g_K^g n^4\cdot(V_m^n - E_K), && (2.15)\\
& && (2.16)
\end{aligned}$$

with the gated conductances $g_{Na,K}^g$ and the Nernst potentials of sodium E_{Na} and potassium E_K. This equilibrium potentials occur when the forces due to the concentration gradient and the forces due to the electrical potential that drive a particular ionic species through a membrane are balanced. In the HH model, the Nernst potentials are given as constant parameter values.

The leak currents of all ions in the HH model are summarized in one unspecific leak current,

$$I_{leak} = g^l\cdot(V+68), \tag{2.17}$$

with the leak conductance g^l. Eq. (2.17) ensures that the single stable fixed point of the system is the polarized membrane potential, $V_m^n = -68$mV.

In [24], it is proposed to replace the leak current I_{leak} by a leak-only chloride current I_{Cl} and also consider specific leak currents for sodium and potassium. The transmembrane ionic currents then read

$$\begin{aligned}
I_{Na} &= I_{Na}^l + I_{Na}^g = (g_{Na}^l + g_{Na}^g m^3 h)\cdot(V_m^n - E_{Na}), && (2.18)\\
I_K &= I_K^l + I_K^g = (g_K^l + g_K^g n^4)\cdot(V_m^n - E_K), && (2.19)\\
I_{Cl} &= I_{Cl}^l = g_{Cl}^l\cdot(V - E_{Cl}), && (2.20)
\end{aligned}$$

with the gated and leak conductances $g_j^{l;g}$, where $j = 1..3$ specifies the respective ionic species (Na, K and Cl). All model parameters are listed in Tab. 2.1. The units for conductance densities imply, that ionic and pump current densities are in μA/cm^2.

The HH model can be reduced by two common simplifications. One is to replace dynamics of the fastest gating variable m by its steady state value m_∞,

$$m = m_\infty(V_m^n). \tag{2.21}$$

In addition, there is an approximate functional relation between h and n, that is usually realized as a linear fit. This, however, in the ion-based version of the model, can lead to negative values of h. Thus, in [24], a sigmoidal fit is used instead,

$$h = 1 - \frac{1}{1 + \exp(-6.5(n - 0.35))}. \tag{2.22}$$

In the HH model, ion concentrations are model parameter. In ion-based models, intra- and extracellular ion concentrations are dynamical variables. Temporal changes of ion concentrations are caused by transmembrane currents. Here, gated, leak and pump currents are considered,

$$\begin{aligned}
\frac{\partial Na_n}{\partial t} &= -\frac{\gamma}{\omega_n}(I_{Na} + 3I_P), & (2.23)\\
\frac{\partial K_n}{\partial t} &= -\frac{\gamma}{\omega_n}(I_K - 2I_P), & (2.24)\\
\frac{\partial Cl_n}{\partial t} &= +\frac{\gamma}{\omega_n}I_{Cl}, & (2.25)
\end{aligned}$$

with Na_n, K_n and Cl_n being the concentration of sodium, potassium and chloride in the NCS, and with the NCS volume ω_n. The factor γ, the ratio of the membrane surface A_m and Faraday's constant F,

$$\gamma = \frac{A_m}{\mathrm{F}}, \tag{2.26}$$

converts currents to ion fluxes. I_{Na}, I_K and I_{Cl} are the currents calculated by Eqs. (2.18)-(2.20), a combination of gated and leak currents. The ATP-driven pump current I_P, that replaces intracellular sodium with extracellular potassium at a 3/2-ratio, is calculated by a formalism proposed in [23],

$$I_P(Na_n, K_n) = \frac{I_{max}}{(1 + \exp((25 - Na_n)/3))\,(1 + \exp(5.5 - K_e))}, \tag{2.27}$$

where I_{max} is the maximal pump current.

Name	Value & unit	Description
C_m	1 μF/cm^2	membrane capacitance
g^l_{Na}	0.0175 mS/cm^2	sodium leak conductance
g^g_{Na}	50 mS/cm^2	max. gated sodium conductance
g^l_K	0.05 mS/cm^2	potassium leak conductance
g^g_K	40 mS/cm^2	max. gated potassium conductance
g^l_{Cl}	0.05 mS/cm^2	chloride leak conductance
$Na^{(0)}_n$	25.35 mmol/l	initial NCS sodium conc.
$Na^{(0)}_e$	115.52 mmol/l	initial ECS sodium conc.
$Na^{(0)}_a$	25.35 mmol/l	initial ACS sodium conc.
$K^{(0)}_n$	128.76 mmol/l	initial NCS potassium conc.
$K^{(0)}_e$	3.96 mmol/l	initial ECS potassium conc.
$K^{(0)}_a$	128.76 mmol/l	initial ACS potassium conc.
$Cl^{(0)}_n$	10.80 mmol/l	initial NCS chloride conc.
$Cl^{(0)}_e$	137.80 mmol/l	initial ECS chloride conc.
$Cl^{(0)}_a$	10.80 mmol/l	initial ACS chloride conc.
ω_n	2160 μm^3	NCS volume
ω_e	720 μm^3	ECS volume
ω_a	2160 μm^3	ACS volume
I_{max}	6.8 μA/cm^2	max. pump current
A_m	922 μm^2	membrane surface
F	96485 C/mol	Faraday's constant
γ	9.556e^{-3} $\frac{\mu\text{m}^2\text{mol}}{\text{C}}$	conversion factor
R	8.135 $\frac{\text{J}}{\text{mol K}}$	gas constant
T	310 K	temperature
D_{Na}	$1.32 \cdot 10^{-5}$ cm^2/s	sodium diffusion coefficient
D_K	$2.0 \cdot 10^{-5}$ cm^2/s	potassium diffusion coefficient
D_{Cl}	$2.0 \cdot 10^{-5}$ cm^2/s	chloride diffusion coefficient
λ_e	1.6	tortuosity of the ECS
λ_a	3.2	tortuosity of the ACS
C_a	0.5	current strength at glial membrane

TABLE 2.1: Parameter values of two- and three-compartmental local and spatially extended ion-based model.

The rate equation for the membrane potential Eq. (2.1) including a chloride I_{Cl} and a pump current I_P reads

$$\frac{\partial V_m^n}{\partial t} = -\frac{1}{C_m}(I_{Na} + I_K + I_{Cl} + I_P - I_{app}). \tag{2.28}$$

Due to mass conservation, the extracellular ion concentration can be calculated by

$$c_j^e = c_j^{e(0)} + \frac{\omega_n}{\omega_e}\left(c_j^{n(0)} - c_j^n\right), \tag{2.29}$$

with $c_j^{n,e}$ being the concentration of the j-th ionic species in the NCS and in the ECS respectively, and with the ECS volume ω_e. The superscript zero indicates initial values.

The Nernst potentials are dynamic now. They depend on the concentrations of the respective ionic species inside and outside the cell,

$$E_j = -\frac{\mathrm{RT}}{z_j\mathrm{F}}\ln\frac{c_j^n}{c_j^e}. \tag{2.30}$$

In [24], it is discussed that the ion-based system consisting of 5 rate equations

$$\begin{aligned}
\frac{\partial V_m^n}{\partial t} &= -\frac{1}{C_m}(I_{Na} + I_K + I_{Cl} + I_P - I_{app}), && (2.31)\\
\frac{\partial n}{\partial t} &= \frac{n_\infty - n}{\tau_n}, && (2.32)\\
\frac{\partial Na_n}{\partial t} &= -\frac{\gamma}{\omega_n}(I_{Na} + 3I_P), && (2.33)\\
\frac{\partial K_n}{\partial t} &= -\frac{\gamma}{\omega_n}(I_K - 2I_P), && (2.34)\\
\frac{\partial Cl_n}{\partial t} &= +\frac{\gamma}{\omega_n}I_{Cl} && (2.35)
\end{aligned}$$

is nonhyperbolic, i.e., the structurally unstable phase space structure can be changed by arbitrarily small perurbations. In order to make the system structurally stable, it is proposed to reduce the system. One variable (except for n) is eliminated and expressed in terms of the others. As the membrane potential is a consequence of changes in ion concentrations, here we choose to eleminate Eq. (2.31). For this purpose, first Eqs. (2.33)-(2.35) are inserted into Eq. (2.31),

$$\frac{\partial V_m^n}{\partial t} = \frac{\omega_n}{C_m\gamma}\left(\frac{\partial Na_n}{\partial t} + \frac{\partial K_n}{\partial t} - \frac{\partial Cl_n}{\partial t}\right). \tag{2.36}$$

Integrating this over time yields the standard capacitor equation

$$V_m^n = \frac{1}{C_m\gamma}\rho_n. \tag{2.37}$$

$\rho_{n,e}$ is the total amount of charges in the NCS,

$$\rho_n = z_0^n F \omega_n c_{imp}^n + \sum_{j=1}^{3} z_j F \omega_n c_j^n, \tag{2.38}$$

with the valence of the respective ions z_j and the concentration and valence of the impermeable ions in the NCS c_{imp}^n and z_0^n respectively. The physiological meaning of this reduction is that the possibility of unspecific applied currents is ruled out. For instance, a perturbation on the potassium rate Eq. 2.34 should be interpreted as a potassium current.

With I_j^n being the transmembrane gated, leak and pump currents of each considered species,

$$\begin{aligned} I_{Na}^n &= (g_{Na}^l + g_{Na}^g m^3 h) \cdot (V_m^n - E_{Na}) + 3I_P, && (2.39)\\ I_K^n &= (g_K^l + g_K^g n^4) \cdot (V_m^n - E_K) - 2I_P, && (2.40)\\ I_{Cl}^n &= g_{Cl}^l \cdot (V - E_{Cl}), && (2.41)\end{aligned}$$

the full set of rate equations reads

$$\begin{aligned} \frac{\partial n}{\partial t} &= \frac{n_\infty - n}{\tau_n}, && (2.42)\\ \frac{\partial c_j^n}{\partial t} &= -z_j \frac{\gamma}{\omega_n} I_j^n. && (2.43)\end{aligned}$$

These rate equations are complemented by the following constraints,

$$\begin{aligned} m &= m_\infty(V), && (2.44)\\ h &= 1 - \frac{1}{1 + \exp(-6.5(n - 0.35))}, && (2.45)\\ c_j^e &= c_j^{e(0)} + \frac{\omega_n}{\omega_e}\left(c_j^{n(0)} - c_j^n\right), && (2.46)\\ V_m^n &= \frac{1}{C_m \gamma}\rho_n. && (2.47)\end{aligned}$$

The model presented here is bistable in a wide parameter range, see Fig. 2.1. In addition to the polarized state ($V_m^n = -68$mV), the system has a second stable state with depolarized membrane potential ($V_m^n \approx -25$mV) and largely depleted ion gradients. After a super-threshold excitation (e.g., a strong current pulse or switching off ion pumps) the system remains in the depolarized state and does not recover any more, Fig. 2.2. During anoxic depolarization, we find this behaviour. The depolarization during CSD, however, usually recovers after a time of about 100 s.

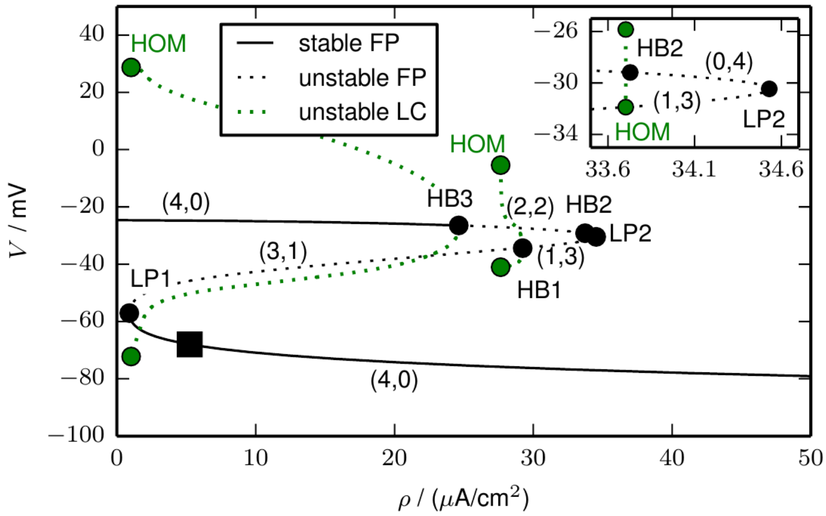

FIGURE 2.1: (V_m^n, I_{max})-bifurcation diagram of the two-compartmental ion-based model Eqs. (2.42)-(2.47). The fixed point (FP) is presented as a black line, the maximal and minimal membrane potential of the limit cycle (LC) is drawn as a green line. Stable sections are solid, unstable sections are dashed. Bifurcations are marked by circles, the physiological resting state by a black square. Following the characteristic z-shaped FP line from below, there are two limit point bifurcations (LP1, LP2) and three supercritical Hopf bifurcations (HB1, HB2, HB3). The LCs created in HB1, HB2 and HB3 disappear in homoclinic bifurcations (HOMs). The number of stable (n_-) and unstable (n_+) directions of the fixed point is indicated by the (n_-, n_+)-tuples. There is bistability of a physiological state and a depolarized state between LP1 and HB3. Figure from [24].

In Sect. 2.4.1, we show that the buffering of excess ions in the ECS by glia cells and from there further in the blood vessels, Sect. 2.4.3, can maintain ionic homeostasis.

2.2 Robustness of the phase space structure

The model proposed in Sect. 2.1 is based on the HH model. In literature, we find a huge variety of biologically plausible parameter values of the common HH model, see e.g. [16, 17, 68]. However, in excitable systems, slight changes in the parameter values might cause completely different dynamics if a bifurcation is passed. Here, the robustness of the phase space structure of the ion-based model Sect. 2 to variations of parameter values is discussed. Therefor, we vary several HH parameter values over a wide range and compare the position of the stable states in a bifurcation diagram.

The parameter values of the common HH model are not directly comparable to the parameter values of the ion-based HH-type model. In detail, the ion-based HH type model has gated and leak currents for each ionic species Eqs. (2.18)-(2.20), whereas the common HH model has specific gated currents and one unspecific leak current, see

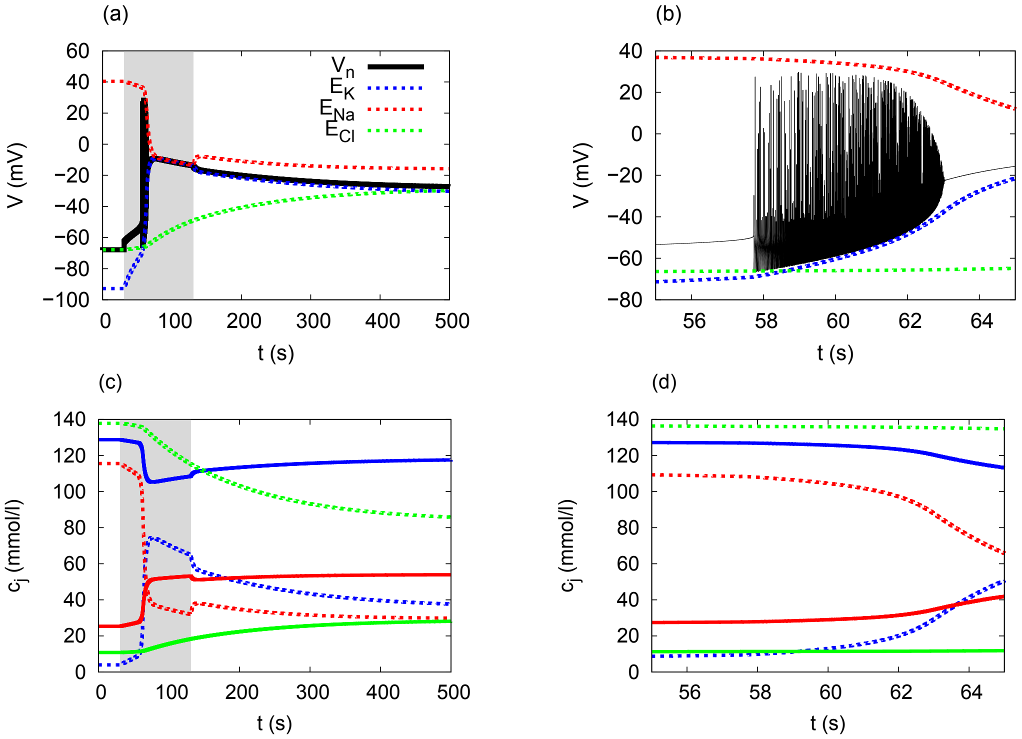

FIGURE 2.2: Response of the single-neuron model to a super-threshold excitation. (a) The system initialized in the polarized membrane potential is perturbed by augmentation of extracellular potassium concentration (grey shaded area). Thereby, the membrane potential V_m^n depolarizes; the Nernst potentials E_j of each ionic species approach to V_m^n. (b) Inset at the rising front shows characteristic initial bursting. (c) Corresponding ion concentration c_j of K (blue), Na (red) and Cl (green), each in the NCS (solid) and in the ECS (dashed). (d) Inset at the rising front shows changes of ion concentrations.

Sect. 2. In addition, in the ion-based model, a description for potassium and sodium ATPase is introduced. Furthermore, the Nernst potentials in the ion-based model are dynamic, Eq. (2.30), whereas in the common HH model, they are static parameter values. Thus, it is not surprising that completely different parameter values are used in ion-based models, within which however also variations can be found [18–21, 23, 24, 27, 28]. In all of this works, the choice of the parameter values is justified by the requested output of the model merely. In the model approach proposed in [24], mainly parameter values from [23] are used.

To analyze the robustness of the ion-based model, we consider a wide range of parameter values. In detail, we investigate, in which parameter regime the model provides bistable dynamics. As stability of the depolarized state is due to an equilibrium between the gated and the pump currents of sodium and potassium, we analyze, how changes in the gated currents affect the phase space structure. The strength of the gated currents is defined by the gated conductances g_j^g, the voltage-dependent probability, that the gated channels are open or closed is given by the gating variables m, h and n.

In Sect. 2.2.1 we show, how bistability is affected by variations of the gated conductances g_j^g, and in Sect. 2.2.2 we analyze, how changes in dynamics of the gating variables m, h and n affect bistability.

2.2.1 Varying strength of gated currents

The gated currents considered are the fast inward sodium current and the slower outward potassium current. After a small perturbation, ion pumps are required to recover the system to the physiological steady state. The sodium-potassium ATPase counteracts the gated currents, it pumps sodium out of the cell and potassium into the cell to maintain ionic homeostasis. In the physiological steady state, the gated currents are almost zero, leak currents and pump currents are balanced. If, however, the system is massively perturbed, e.g., during CSD, the voltage-dependent gated currents can become very strong. Then, ion pumps are not sufficient to recover the system to the physiological steady state, but the system ends up in a depolarized state with largely depleted ion gradients. In this depolarized state, the leak currents are very small, the pump currents and the gated currents are balanced.

If the strength of both gated currents, the sodium and the potassium current, is increased by the same factor, a larger pump current is required to compensate for the gated currents. This can be seen in Fig. 2.3(a). The bifurcation diagram drawn with the continuation software *AUTO* [69] shows the extracellular potassium concentration K_{ex} at fixed point values as a function of maximal pump rate I_{max}. Branches for varying strength of gated conductances g_j^g are shown, whereat the relation of the gated conductance of sodium g_{Na}^g and potassium g_K^g is constant ($g_{Na}^g/g_K^g = const.$). Phase space structure changes quantitatively, i.e., for stronger gated conductances g_j^g, a stronger pump rate I_{max} is required to annihilate bistability. In addition, to maintain the depolarized equilibrium, in systems with stronger gated conductances, a larger concentration of extracellular potassium K_{ex} is required to increase the pump currents in the depolarized state to be strong enough to compensate for the increased gated currents. Changing the strength of both gated currents with the same factor changes the bifurcation diagram quantitatively, but not qualitatively. The system provides bistability in a wide parameter range.

However, if the strength of the gated potassium current g_K^g is changed massively whereas the gated sodium current remains equal, the bifurcation diagram changes qualitatively, Fig. 2.3(b). However, at the in literature usually used pump rate of about $5\,\frac{\mu\mathrm{A}}{\mathrm{cm}^2}$, the system provides bistability for a wide range of g_K^g.

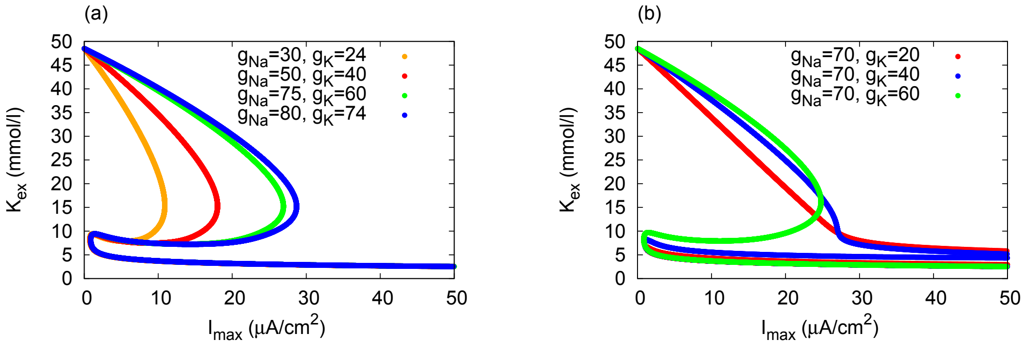

FIGURE 2.3: Bifurcation diagram of the two-compartmental ion-based model Eqs. (2.42)-(2.47). The extracellular potassium concentration K_{ex} at fixed point values is shown as a function of maximal pump current I_{max}. Fixed point branches are shown for varying strength of gated conductances. (a) Varying strength of gated conductances g^g_j, the relation of the gated conductances is constant ($g^g_{Na}/g^g_K = const.$); (b) varying strength of the gated conductance of potassium g^g_K, the gated conductance of sodium g^g_{Na} remains equal.

2.2.2 Varying dynamics of gated currents

Dynamics of the gated currents are defined by their voltage-dependent steady state values x_∞ and timescales τ_x,

$$x_\infty = \frac{\alpha_x}{\alpha_x + \beta_x}, \tag{2.48}$$

$$\tau_x = \frac{1}{\alpha_x + \beta_x}, \tag{2.49}$$

with x being n, m or h.

The fast gating variable m activates the gated sodium inward current, what causes a depolarization. The depolarization is inhibited by h, the inactivation of the gated sodium channel and by an increase of n, the activation of the gated potassium current. Decisive for system dynamics is the relationship between the sodium and the potassium currents, see Sect. 2.2.1. Thus, here we analyze, how phase space structure changes under variations of the slow gating variable n, whereat the sodium gating variables m and h remain constant.

The variations of n are realized by changing the steepness and position of the steady-state conductance n^4_∞. The HH exponential funtions of n are

$$\alpha_n(V) = \frac{\alpha^n_1(V + \alpha^n_2)}{1 - \exp((V + \alpha^n_2)/\alpha^n_3)}, \tag{2.50}$$

$$\beta_n(V) = \beta^n_1 \exp(-(V + \beta^n_2)/\beta^n_3). \tag{2.51}$$

β^n_3 determines the steepness of n^4_∞, see Fig. 2.4(a).

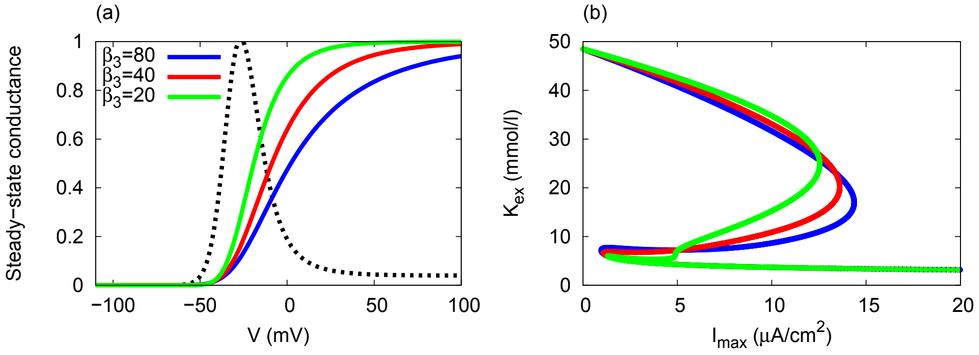

FIGURE 2.4: (a) Steady-state conductance of sodium m^3h normalized to a maximum value of 1 (black, dashed) and of potassium n_∞^4 (coloured, solid) as a function of the membrane potential V_m^n with varying steepness β_3^n of the potassium conductance n_∞^4, see Eq. (2.51). The other values of α_n Eq. (2.50) and β_n Eq. (2.51) are chosen according to Eqs. (2.10),(2.11). (b) Corresponding bifurcation diagram calculated with the two-compartmental ion-based model Eqs. (2.42)-(2.47). The extracellular potassium concentration K_{ex} at fixed point values is shown as a function of maximal pump current I_{max}.

Varying the steepness of n_∞^4 and quantifying the position of the stable states in a bifurcation diagram Fig. 2.4(b), we find that if the gated potassium currents open at a less depolarized membrane potential, the depolarized state is annihilated at a smaller pump rate I_{max}.

Next, to shift the position of n_∞^4 with respect to V_m^n, we first approximate the steady-state conductance n_∞ as proposed in [70] with

$$n_\infty(V) \quad = \quad \frac{1}{1+\exp\left((V_{1/2}^n - V)/k^n\right)}. \tag{2.52}$$

The timescale is approximated by

$$\tau_n(V) \quad = \quad C_{base}^n + C_{amp}^n \exp\left(-(V_{max}^n - V)^2/\sigma_n^2\right). \tag{2.53}$$

We fit this to the original description Eqs. (2.48),(2.49) with α_n defined by Eq. (2.10) and β_n defined by Eq. (2.11) using the *NMinimize* function of the software *Mathematica*. The thereby determined parameter values of Eqs. (2.52),(2.53) are listed in Tab. 2.2.

The original and fitted curves of $n_\infty(V)$ and $\tau_n(V)$ are shown in Figs. 2.5(a),(b). Replacing the description of $n_\infty(V)$ and $\tau_n(V)$ by the approximative descriptions Eq. (2.52) and Eq. (2.53), the bifurcation diagram changes quantitatively, see Fig. 2.5(c). The bistability in the parameter regime around $I_{max} \approx 5\ \mu$A/cm^2 persists.

Name	Value	Unit
$V_{1/2}$	-28.4238	mV
k_n	17.3834	1/mV
C^n_{base}	0.189003	ms
C^n_{amp}	1.61589	ms
V^n_{max}	-64.3065	mV
σ^2_n	74.6914	$1/(\text{mV})^2$

TABLE 2.2: Parameter values of fitted steady state value $n_\infty(V)$ Eq. (2.52) and timescale $\tau_n(V)$ Eq. (2.53).

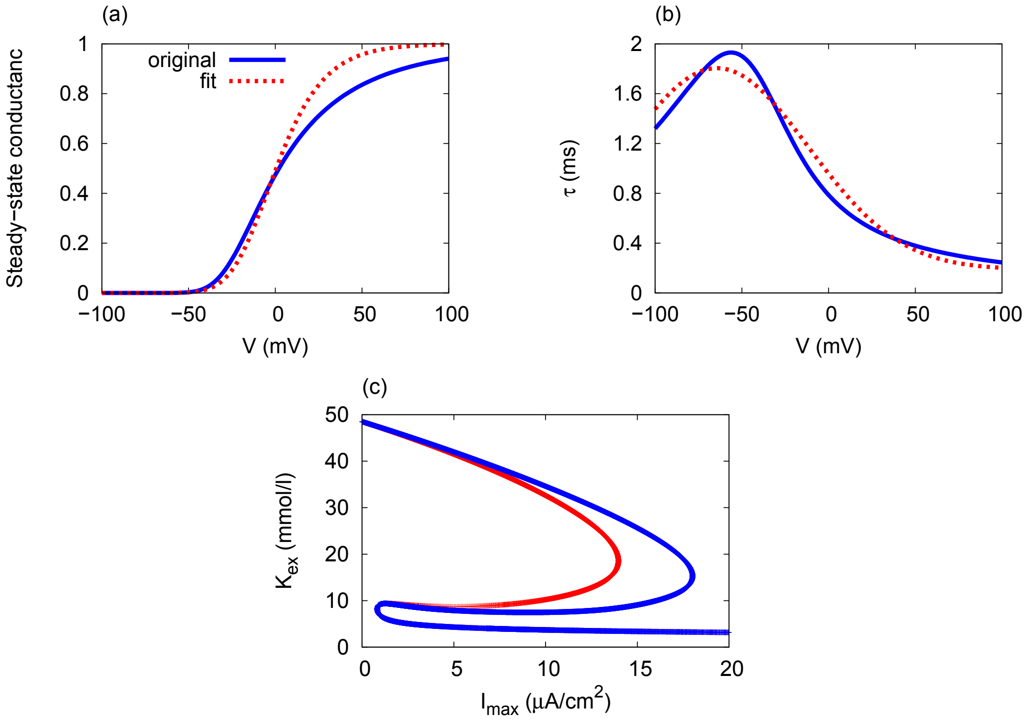

FIGURE 2.5: The original descriptions of the steady state conductance n^4_∞ and timescale τ_n of potassium Eqs. (2.48),(2.49) are compared to the fitted descriptions Eqs. (2.52),(2.53). (a) Steady-state conductance of potassium n^4_∞ as a function of the membrane potential V^n_m. (b) Timescale τ_n as a function of the membrane potential V^n_m. (c) Bifurcation diagram of the ion-based model Eqs. (2.42)-(2.47). The extracellular potassium concentration K_{ex} at fixed point values is shown as a function of maximal pump current I_{max}.

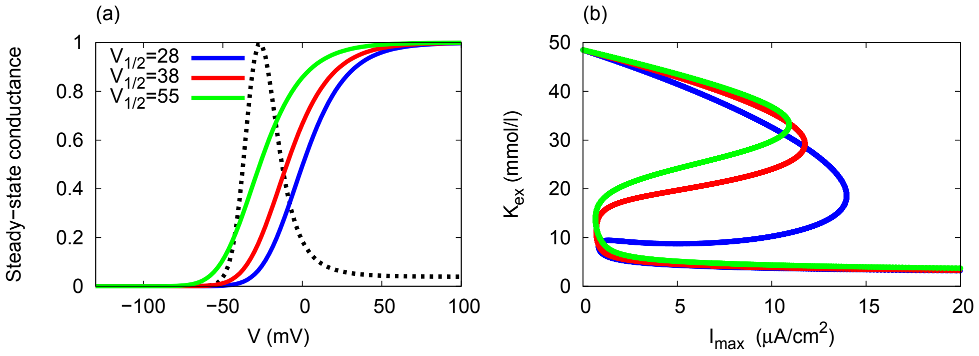

FIGURE 2.6: Shifting the Steady-state conductance of potassium n_∞^4 with respect to the membrane potential V_m^n by varying $V_{1/2}$, see Eq. (2.52). (a) Steady-state conductance of sodium m^3h normalized to a maximum value of 1 (black, dashed) and of potassium n_∞^4 (coloured, solid) as a function of the membrane potential V_m^n. (b) Bifurcation diagram of the ion-based model Eqs. (2.42)-(2.47). The extracellular potassium concentration K_{ex} at fix point values is shown as a function of maximal pump current I_{max}.

The position of the steady-state conductance of potassium n_∞^4 described by the approximation Eq. (2.52) can easily be shifted with respect to the membrane potential V_m^n by varying the parameter $V_{1/2}$, see Fig. 2.6(a). Be aware, that a shift of the steady-state conductance n_∞ also can be realized by adding a constant value ΔV to each V in α_n Eq. (2.50) and β_n Eq. (2.51). However, for numerical reasons, I used the approximative description Eq. (2.52). We find that if the potassium currents are activated at a smaller depolarization, a smaller pump rate I_{max} is sufficient to annihilate bistability, Fig. 2.6(b).

In both analyzed cases, changing the steepness of the potassium steady-state conductance with respect to the membrane voltage and varying the position of the potassium steady-state conductance with respect to the membrane voltage, we find qualitatively the same results. First, if the gated potassium currents open at a smaller depolarization, a smaller pump rate I_{max} is sufficient to annihilate bistability. Second, in the whole analyzed range of potassium steady-state conductances, the model provides bistability in a wide range of pump rates.

2.3 Membrane potential and electroneutrality

In most quantitative treatments of the membrane potential, electroneutrality is assumed. Although there is an electrical potential across the membrane due to charge separation, there is no measurable difference in the global concentration of positive and negative ions in both sides of the membrane. That occurs, because a small undetectable change in the charge concentration creates a great change on electrical potential.

In most neuron models, changes in the membrane potential V_m^n are assumed to be due to transmembrane currents only and thus are proportional to changes in the amount of charges in the NCS,

$$V_m^n = \frac{1}{C_m\gamma}\rho_n. \tag{2.54}$$

With this description, small changes in the amount of charges $\Delta\rho_n$ create great changes in the membrane potential ΔV_m^n, since $C_m\gamma$ is very small. Δ denotes the difference between the initial and final value of a variable. Electroneutrality in the NCS holds, as from

$$\Delta\rho_n = C_m\gamma\Delta V_m^n \tag{2.55}$$

follows, that

$$\Delta\rho_n \approx 0. \tag{2.56}$$

In a closed system, i.e., a neuron surrounded by an extracellular space without ion exchange with the surrounding, electroneutrality in the NCS implies electroneutrality in the ECS. As mass conservation constraint Eq. (2.46) holds, we can find an expression for the membrane potential equivalent to Eq. (2.54). From mass conservation follows charge conservation,

$$\rho_n = -\rho_e, \tag{2.57}$$

if the initial conditions are chosen such that $\rho_n^{(0)} = -\rho_e^{(0)}$. Inserting Eq. (2.57) in Eq. (2.54) yields

$$V_m^n = -\frac{1}{C_m\gamma}\rho_e. \tag{2.58}$$

However, in open systems, e.g., if glial buffering is introduced or in spatially extended systems with ion diffusion in the ECS, it has to be considered that changes in the membrane potential are due to changes in the amount of charges in both, the NCS and the ECS. This fact is captured by the definition of the membrane potential [71],

$$V_m^n = \Phi^n - \Phi^e, \tag{2.59}$$

with $\Phi^{n,e}$ being the electrical potential in the NCS and in the ECS respectively.

We assume Φ^n and Φ^e to be proportional to the amount of charges in the NCS and in the ECS respectively,

$$\Phi^n = K\rho_n, \tag{2.60}$$

$$\Phi^e = K\rho_e. \tag{2.61}$$

If the system is closed and the initial conditions are chosen such that $\rho_n = -\rho_e$, Eq. (2.59)

$$V_m^n = K\left(\rho_n - \rho_e\right) \tag{2.62}$$

is equivalent to Eq. (2.54) and to Eq. (2.58) for $K = \frac{1}{2C_m\gamma}$,

$$V_m^n = \frac{1}{2C_m\gamma}\left(\rho_n - \rho_e\right). \tag{2.63}$$

If charge conservation is violated, Eqs. (2.54),(2.58) and (2.63) determine dissimilar behaviour. In particular, electroneutrality is affected. Calculating the membrane potential by the amount of charges in the neuron Eq. (2.54) determines electroneutrality in the NCS, see Eq. (2.56), but not in the ECS. Using the amount of charges in the ECS to calculate the membrane potential Eq. (2.58) in contrast implies electroneutrality in the ECS, but not in the NCS, as from Eq. (2.58) follows

$$\rho_e = C_m\gamma V_m^n \approx 0. \tag{2.64}$$

Using the definition of the membrane potential Eq. (2.63) however states that

$$\rho_n - \rho_e = 2C_m\gamma V_m^n \approx 0. \tag{2.65}$$

In this case, the amount of charges in the NCS equals the amount of charges in the ECS, what not necessarily implies electroneutrality.

How to achieve electroneutrality in both compartments in open systems is discussed with the help of examples in Sect. 2.4.4, and in spatially extended reaction-diffusion systems in Sect. 3.1.1.

For the sake of completeness, I will add some considerations about neuronal systems including astrocytes here. If the model has three compartments, neurons and astrocytes surrounded by an extracellular space, the potential at both, the neuronal and the astrocytic membrane, has to be calculated. This could in a first approximation be done by an expression following Eq. (2.54),

$$V_m^{n,a} = \frac{1}{C_m\gamma}\rho_{n,a}, \tag{2.66}$$

with V_m^a being the astrocytic membrane potential and $\rho_a = z_0^a F \omega_a c_{imp}^a + \sum_{j=1}^3 z_j F \omega_a c_j^a$ being the amount of charges in the astrocyte with the valence z_0^a and the concentration of impermeable ions c_{imp}^a. Thereby, it is neglected that due to currents through the astrocytic membrane changes in the amount of charges in the ECS might occur, that affect the neuronal membrane potential, and vice versa. This issue is taken into account by a description according to Eq. (2.63),

$$V_m^{n,a} = \frac{1}{2C_m\gamma}(\rho_{n,a} - \rho_e). \tag{2.67}$$

Be aware, that this description is a consequence of the assumption of single point compartments, i.e., the spatial extension of the compartments is neglected. In fact, excess ions in the particular compartments are stored close to the respective membrane, which impedes them to gravitate towards each other. The charge concentration thereby decays exponentially with respect to the distance from the membrane. The amount of excess charges in the ECS is distributed into ones that are stored nearby the neuronal membrane and ones that are stored nearby the astrocytic membrane and thus mainly contribute to the respective potential. Hence the potential at the neuronal membrane and the potential at the astrocytic membrane can be written as

$$\begin{aligned} V_m^n &= \frac{1}{2C_m\gamma}(\rho_n - G\rho_e), & (2.68)\\ V_m^a &= \frac{1}{2C_m\gamma}(\rho_a - (1-G)\rho_e), & (2.69) \end{aligned}$$

with G being the portion of ECS charges stored at the neuronal membrane.

In a closed system, due to mass conservation, the changes in charges in the ECS are a superposition of changes in charges in the NCS and changes in charges in the ACS,

$$\rho_e = -\rho_n - \rho_a. \tag{2.70}$$

The amount of ρ_e can be separated in a portion generated by neuronal-extracellular ion exchange G_n and a portion generated by astrocytic-extracellular ion exchange G_a,

$$\rho_e = G_n\rho_e + G_a\rho_e, \tag{2.71}$$

with $G_n = \frac{\rho_n}{\rho_n+\rho_a}$ and $G_a = \frac{\rho_a}{\rho_n+\rho_a} = 1 - G_n$. Assuming that the distribution G aims at an electrical equilibrium between the neuronal and the astrocytic membrane yields that the portion G_n of ρ_e contributes to V_m^n and the portion $(1 - G_n)$ of ρ_e contributes to V_m^a, thus

$$G = G_n = \frac{\rho_n}{\rho_n + \rho_a}. \tag{2.72}$$

The description of the membrane potentials Eqs. (2.68),(2.69) in a closed system equals Eq. (2.66), what can be seen by inserting G Eq. (2.72) and ρ_e Eq. (2.70) in Eqs. (2.68)-(2.69),

$$\begin{aligned} V_m^n &= \frac{1}{2C_m\gamma}(\rho_n - G\rho_e) = \frac{1}{C_m\gamma}\rho_n, && (2.73)\\ V_m^a &= \frac{1}{2C_m\gamma}(\rho_a - (1-G)\rho_e) = \frac{1}{C_m\gamma}\rho_a. && (2.74)\end{aligned}$$

In an open system, however, assuming that the distribution aims at an electrical equilibrium, G has to be formulated in a more general way,

$$G = \Theta((\rho_a - \rho_n)\cdot\rho_e))\cdot R_1 + R_2, \qquad (2.75)$$

with

$$\begin{aligned} R_1 &= \mid \rho_n - \rho_a \mid \frac{1}{\mid \rho_e \mid}\Theta(\mid \rho_e \mid - \mid \rho_n - \rho_a \mid) + \Theta(\mid \rho_n - \rho_a \mid - \mid \rho_e \mid), && (2.76)\\ R_2 &= 0.5(1 - R_1), && (2.77)\end{aligned}$$

with Θ being the heaviside step function. Be aware that the equality of Eq. (2.66) and Eqs. (2.68),(2.69) in open systems does not hold, as mass conservation Eq. (2.70) is violated.

In Sect. 2.4.4, we show examples using description Eq. (2.66), Eq. (2.67) and Eqs. (2.68)-(2.69) to calculate the membrane potential at the neuron and the astrocyte and discuss, how electroneutrality is affected by the respective description.

2.4 Glial buffer

As shown in [24], the two-compartmental single-neuron model Eqs. (2.42)-(2.47) is bistable. However, brain tissue depolarized due to CSD usually repolarizes after a time of about 100 s. Thereby, clearance of extracellular excess ions, besides restoration in the neuron by ATPase, likely depends on local uptake by- and intracellular transport within astrocytes.

In this Section, the role of astrocytes on ionic homeostasis is analyzed. Therefore, we first model the glia cells as an additional compartment, transmembrane ion exchange with the ECS is assumed to be due to leak and pump currents, Sect. 2.4.1. We carefully analyze, under which conditions this description manages to recover the system from the depolarized to the polarized equilibrium, Sect. 2.4.2. Then, in Sect. 2.4.3, we approximate the glial compartment as a bath, what is reasonable under the assumption of fast clearance of glial excess ions by the vasculature and by lateral diffusion within the glial syncytium.

2.4.1 Three-compartmental ion-based model including glia cells

The two-compartmental model Eqs. (2.42)-(2.47) is bistable, with a polarized physiological and a depolarized pathophysiological state. However, in the brain of a migraine patient, we expect the depolarized state to be transient, whereas the polarized equilibrium is stable. We assume that due to ion uptake by the ACS, the physiological polarized equilibrium is recovered after a period of depolarization.

Before we propose a formalism that captures this, we shortly discuss, which quantities are decisive for bistability in the two-compartmental model. The condition for a stable state is that the ion concentrations are constant,

$$\frac{\partial c_j^{n,e}}{\partial t} = 0. \tag{2.78}$$

This is satisfied if the sum over the transmembrane currents for each ionic species vanishes,

$$I_j^n = 0. \tag{2.79}$$

At the neuronal membrane, the transmembrane currents considered are leak I_j^l, gated I_j^g and pump currents I_P. At the polarized membrane potential $V_m^n = -68\text{mV}$, the gated currents almost vanish ($I_j^g \approx 0$), thus the leak currents I_j^l and the pump current I_P are balanced. In the depolarized state, however, the Nernst potentials E_j^n assimilate to the membrane potential V_m^n, thus the leak currents are very small ($I_j^l \approx 0$). In addition, the pump current I_P is augmented, as the ion concentrations Na_n and K_e are increased. Thus, gated currents I_j^g are needed to compensate for the increased pump current I_P.

At the astrocytic membrane, only leak I_j^a and pump currents I_P^a are considered. In our model, the leak currents I_{Na}^a, I_K^a and I_{Cl}^a and the pump current I_P^a at the astrocytic membrane V_m^a equal the leak currents and the pump current at the neuronal membrane except for a constant scaling factor C_a, which is a measure for the amount of channels at the astrocytic membrane in relation to the amount of channels at the neuronal membrane. The transmembrane currents at the astrocyte are calculated by

$$I_{Na}^a = C_a g_{Na}^l \cdot (V_m^a - E_{Na}^a) + 3I_P^a, \tag{2.80}$$

$$I_K^a = C_a g_K^l \cdot (V_m^a - E_K^a) - 2I_P^a, \tag{2.81}$$

$$I_{Cl}^a = C_a g_{Cl}^l \cdot (V_m^a - E_{Cl}^a), \tag{2.82}$$

with the pump current

$$I_P^a = C_a \frac{\rho}{(1+\exp((25-Na_a)/3))\,(1+\exp(5.5-K_e))}. \tag{2.83}$$

The dynamic Nernst potentials at the astrocytic membrane read

$$E_j^a = -\frac{RT}{z_j F}\ln\frac{c_j^a}{c_j^e}, \tag{2.84}$$

with c_j^a being the concentration of the j-th species in the glia cell. We thereby choose the same initial ion concentrations in the glia cell and in the neuron,

$$c_j^{a(0)} = c_j^{n(0)}, \tag{2.85}$$

see Tab. 2.1. This description of the glial transmembrane currents ensures that the polarized resting state does not change, as the leak I_l^a and pump currents I_P^a are balanced in the polarized equilibrium.

Ion exchange with the surrounding is not considered, thus mass conservation holds,

$$c_j^e = c_j^{e(0)} + \frac{\omega_n}{\omega_e}\left(c_j^{n(0)} - c_j^n\right) + \frac{\omega_a}{\omega_e}\left(c_j^{a(0)} - c_j^a\right). \tag{2.86}$$

Hence, to calculate the ion concentrations in all three compartments, the ion concentration in two compartments has to be calculated with rate equations, and then the ion concentration in the third compartment can be obtained by the mass conservation constraint Eq. (2.86). Thus, three additional rate equations are needed. Either, the ion concentrations in the ACS c_j^a can be calculated by

$$\frac{\partial c_j^a}{\partial t} = -z_j\frac{\gamma}{\omega_a}I_j^a, \tag{2.87}$$

with c_j^a being the concentration of the j-th species in the ACS and I_j^a being the considered leak and pump currents of species j, that cross the astrocytic membrane, Eqs. (2.80)-(2.82). Or, equivalent, the ion concentrations in the ECS c_j^e can be calculated by

$$\frac{\partial c_j^e}{\partial t} = z_j\frac{\gamma}{\omega_e}\left(I_j^n + I_j^a\right). \tag{2.88}$$

The full set of rate equations reads

$$\frac{\partial n}{\partial t} = \frac{n_\infty - n}{\tau_n}, \tag{2.89}$$

$$\frac{\partial c_j^n}{\partial t} = -z_j \frac{\gamma}{\omega_n} I_j^n, \tag{2.90}$$

$$\frac{\partial c_j^a}{\partial t} = -z_j \frac{\gamma}{\omega_a} I_j^a. \tag{2.91}$$

These rate equations are complemented by the following constraints,

$$m = m_\infty(V), \tag{2.92}$$

$$h = 1 - \frac{1}{1+\exp(-6.5(n-0.35))}, \tag{2.93}$$

$$c_j^e = c_j^{e(0)} + \frac{\omega_n}{\omega_e}\left(c_j^{n(0)} - c_j^n\right) + \frac{\omega_a}{\omega_e}\left(c_j^{a(0)} - c_j^a\right), \tag{2.94}$$

$$V_m^n = \frac{1}{2C_m\gamma}\left(\rho_n - \rho_e\right), \tag{2.95}$$

$$V_m^a = \frac{1}{2C_m\gamma}\left(\rho_a - \rho_e\right). \tag{2.96}$$

2.4.2 Dynamics of the three-compartmental model

In Sect. 2.4.1, we proposed a formalism for the glia cells such that the polarized equilibrium remains stable. Here, we analyze if the glial currents manage to recover the system from the depolarized to the polarized state.

To get insight in existence and stability properties of the depolarized state, we determine the projection of the 7-dimensional phase space of the system on the $V_m^n - \frac{\partial V_m^n}{\partial t}$-space. Without currents crossing the glial membrane, temporal changes of the membrane potential V_m^n are caused by the transmembrane currents I_j^n only,

$$\frac{\partial V_m^n}{\partial t} = -\frac{1}{C_m}\sum_j I_j^n. \tag{2.97}$$

To determine the dependency $\frac{\partial V_m^n}{\partial t}(V_m^n)$, we calculate the voltage clamp curve. In experiments, it is obtained by threading an electrode through a nerve axon and closing the circuit with an external control circuit. Then, a step voltage is applied and held constant. The ionic current is measured as a function of time at each fixed voltage level. Thereby, two time scales are involved: a fast rise that corresponds to turning on the sodium inflow (m), followed by a slower slope that is related to turning off the sodium inflow (h) and turning on the potassium outflow (n). In our model, time scales are widely separated; as $\tau_m = 0$, $m = m_\infty(V_m^n)$ changes instantaneously if V_m^n is varied, whereas h and n change on a much slower time scale of several ms.

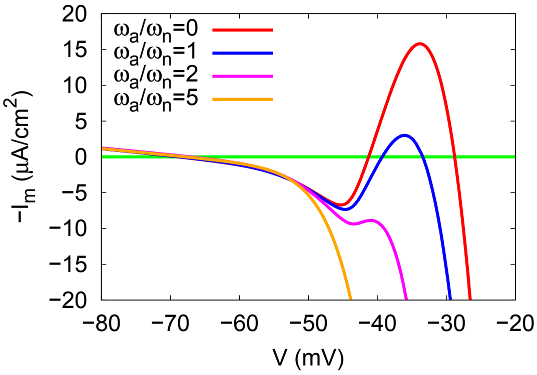

FIGURE 2.7: Projection of the phase space of the three-compartmental ion-based model Eqs. (2.89)-(2.96) on the V_m^n-space. At time T, a step voltage is applied. The negative sum over the transmembrane currents $-\sum_j I_j^n(t=T)$, which is proportional to $\frac{\partial V_m^n}{\partial t}$, is shown as a function of V_m^n. The two-compartmental system without an ACS ($\omega_a = 0$) is bistable. The depolarized state vanishes if the volume fraction of the ACS ω_a is increased.

Thus, directly after a voltage step is applied, the ionic current $\sum_j I_j^n$ is due to gated sodium currents mainly. At the glial membrane, no fast gated currents are considered.

We set the voltage level V_m^n static on values between $V_m^n = -80\text{mV}$ and $V_m^n = -20\text{mV}$, until the system evened out into this state. Thereby, to ensure, that the constraint Eq. (2.47), which describes the dependency of the neuronal membrane potential from the ion concentrations, holds, the rate equation of sodium is replaced by the constraint

$$Na_n = Na_n^{(0)} - K_n + K_n^{(0)} + Cl_n - Cl_n^{(0)} + \frac{C_m\gamma}{\omega_n}\left(V_m^n - V^{(0)}\right), \tag{2.98}$$

$$Na_e = Na_e^{(0)} + \frac{\omega_n}{\omega_e}\left(Na_n^{(0)} - Na_n\right) + \frac{\omega_a}{\omega_e}\left(Na_a^{(0)} - Na_a\right). \tag{2.99}$$

Sodium is chosen, as it changes with V_m^n without time-delay.

At time T, we apply a voltage step of $\Delta V_m^n = 1\text{mV}$. Then, the response directly thereafter $\sum_j I_j^n(t=T)$ is measured. Varying the size or direction of the voltage step ΔV_m^n by a constant factor K changes the response $\sum_j I_j^n(t=T)$ by the same factor K if ΔV_m^n is not to large. Thus, $\frac{\sum_j I_j^n(t=T)}{\Delta V_m^n}$ is independent of the size or direction of the voltage step.

Be aware, that this method is not an accurate bifurcation analysis. First, it only shows the fast current response of the system to changes in the membrane potential. Second, it does not give any information about stability properties of the fixed points or possible bifurcations under changes of parameter values. However, it is a good scheme to get information about the existence and position of fixed points.

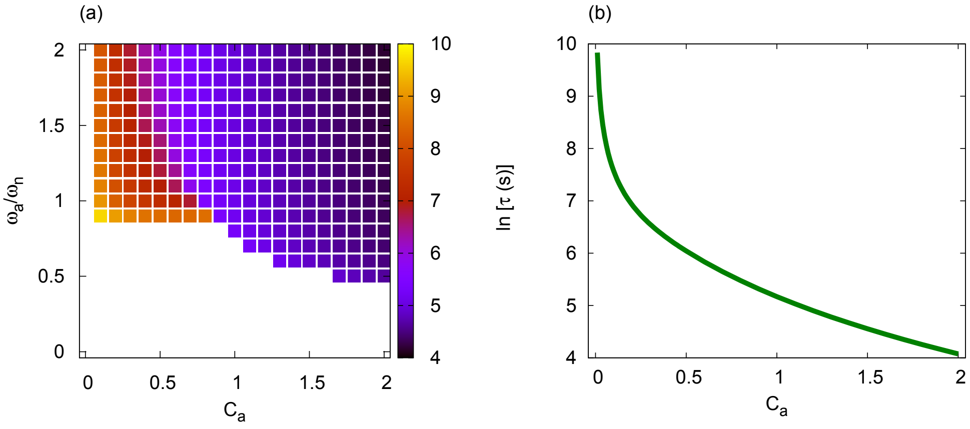

FIGURE 2.8: Relaxation time τ in the three-compartmental model as function of C_a and the relation ω_a/ω_n (with constant ω_n); the system is initialized in the depolarized state of the bistable two-compartmental model Eqs. (2.42)-(2.47); at time $t = 0$, the astrocytic currents Eqs. (2.80)-(2.82) are switched on, what causes a relaxation to the polarized state. The relaxation time τ is the first time with $K_e < 20$ mmol/l. In the white region, the astrocytic currents are too weak to recover the system to the polarized state. The membrane potentials $V_m^{n;a}$ are calculated with Eqs. (2.95),(2.96). (a) Dynamic ion concentrations in ACS, c_j^a calculated with Eq. (2.87), (b) ACS as a bath, $c_j^a = c_j^{a(0)}$.

We find that in the bistable two-compartmental model, the transmembrane currents $\sum_j I_j^n$ behave like a cubic function of the voltage V_m^n, see Fig. 2.7, red curve. The system has three fixed points, where the transmembrane currents sum up to zero. We already know that they comprise two stable ones and, in between, an unstable one.

If we add the glial compartment, phase space structure changes, see Fig. 2.7. If the volume fraction ω_a is small ($\omega_a \leqq \omega_n$), the system still has three fixed points. Due to the composition of the model equations we know that the polarized state remains stable. However, this scheme does not give us information about stability properties of the depolarized state.

Next, we analyze, for which values of C_a and ω_a a system once excited to the depolarized state of the bistable two-compartmental model recovers to the polarized state. For $\omega_a \leqq 0.8 \cdot \omega_n$, we find persistent depolarizations, see Fig. 2.8(a). Therefrom we conclude that the depolarized state remains stable for $\omega_a \leqq 0.8 \cdot \omega_n$. For large values of C_a, the glial buffer nevertheless manages to recover the system to the polarized state, as we did not initialize the system in the basin of attraction of the three-compartmental model. We suppose that the basin of attraction of the depolarized state decreases with increasing volume ω_a.

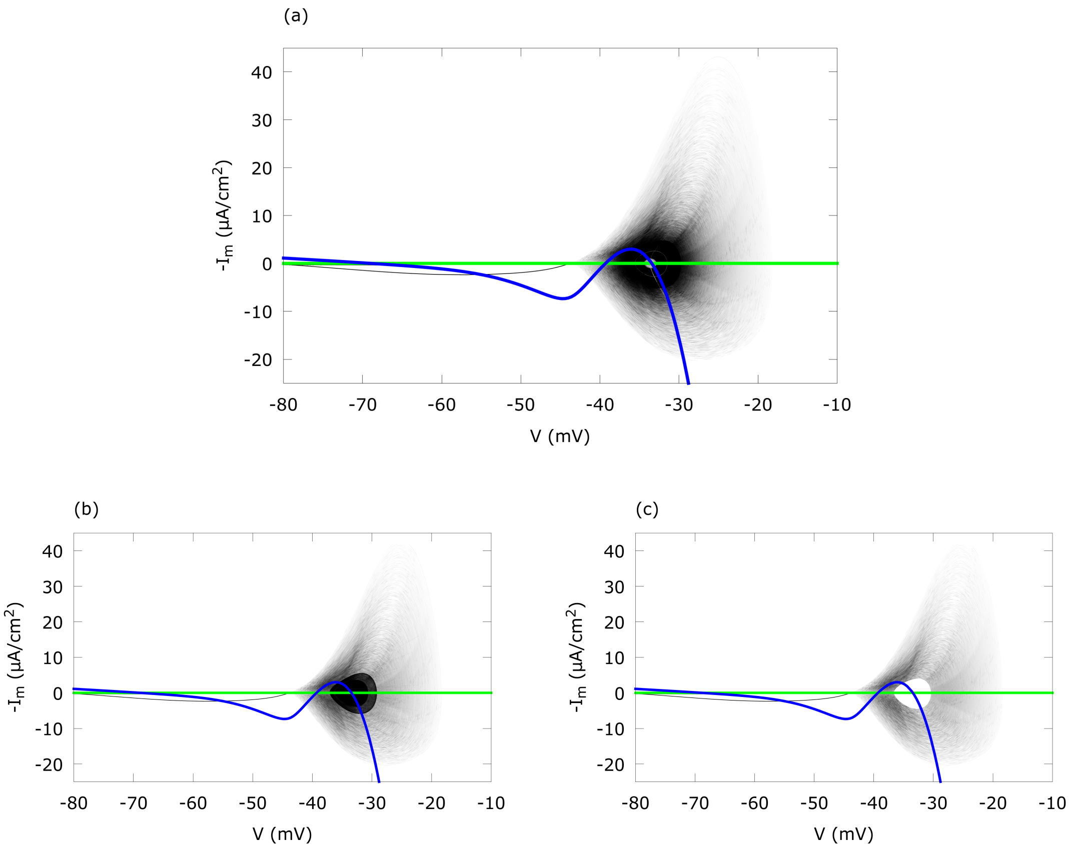

FIGURE 2.9: Projection of the phase space of the three-compartmental ion-based model Eqs. (2.89)-(2.96) with $\frac{\omega_a}{\omega_n} = 1$ on the V_m^n-space. (black) Trajectory during relaxation. The trajectory spirals around the depolarized state, before the system recovers to the polarized state, compare Fig. 2.10. (blue) Voltage clamp curve, compare Fig. 2.7. (a) $C_a = 0.5$, (b) $C_a = 0.1$, (c) $C_a = 1$.

For a larger volume ω_a, the depolarizations are not persistent, Fig. 2.8(a), although for $\omega_a \approx \omega_n$, the system has three fixed points, Fig. 2.7. Mapping the trajectory during relaxation in the V_m^n-space, we find that for small values of C_a it passes very close by the depolarized state and spirals out slowly, Fig. 2.9. In the time course, this corresponds to slight bursting during the relaxation process, see Fig. 2.10. For larger values of C_a, the trajectory does not get so close to the depolarized state, what results in a much shorter relaxation time τ, compare Fig. 2.8(a). From this results, we cannot make a distinct statement concerning stability properties of the depolarized state. However, we suppose that it has at least one unstable direction, as otherwise it is likely to end up in the depolarized state for small values of C_a. But it also is possible that the depolarized state is stable and has a very small basin of attraction.

For even larger values of ω_a, the depolarized state vanishes, the system is monostable, Fig. 2.7. In the monostable system, all excitations recover to the physiological polarized

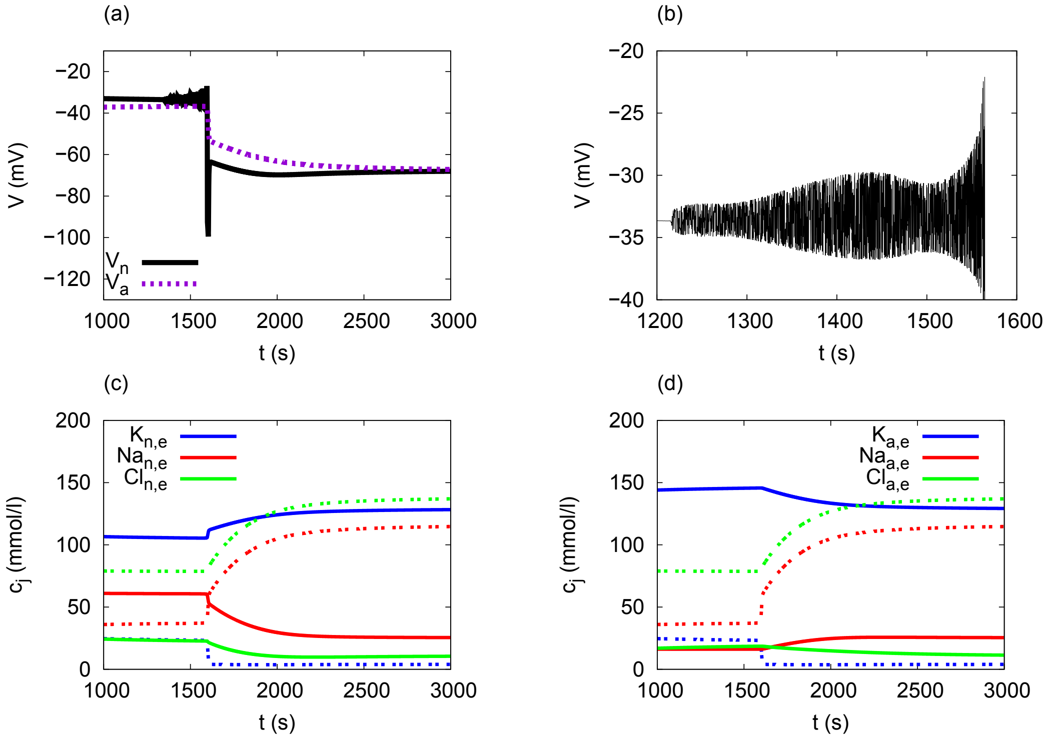

FIGURE 2.10: Temporal evolution during relaxation. The system is initialized in the depolarized state of the bistable two-compartmental model Eqs. (2.42)-(2.46) (Sect. 2.1), and at $t = 0$, the astrocytic currents are switched on. The three-compartmental system is described by Eqs. (2.89)-(2.96) with $\omega_a = \omega_n$ and $C_a = 0.5$. The membrane potentials at the neuron and the astrocyte are calculated with Eq. (2.111) $V_m^{n,a} \sim (\rho_{n,a} - \rho_e)$. (a) Neuronal and glial membrane potential; (b) inset at the back (neuronal membrane potential); (c) ion concentration of K (blue), Na (red) and Cl (green), each in the NCS (solid) and in the ECS (dashed); (d) ion concentration of K (blue), Na (red) and Cl (green), each in the ACS (solid) and in the ECS (dashed).

equilibrium. Thereby, the relaxation time τ depends on the size of the glial compartment ω_a, and, in addition, strongly on C_a, see Fig. 2.8.

In the following, we choose the volume of the astrocyte to be equal the volume of the neuron ($\omega_a = \omega_n$), as this approximately is the case in brain tissue.

2.4.3 Modeling glia cells as a bath

Excess ions in the glia cells are distributed within the glial syncytium by movement through gap junctions. Furthermore, the glia cells are connected to the blood vessels, what enables fast clearance of excess ions. Thus, it is reasonable to make the approximation that excess ions in the ACS are cleared instantaneously.

This can be modeled by the assumption that the ACS is a bath, what equals the limit of an infinitely large glial compartment ($\omega_a \to \infty$). Then, ion concentrations in the glia cells c_j^a are not dynamic any more, but model parameters. They are fixed on the initial concentrations, compare Eq. (2.85),

$$c_j^a = c_j^{a(0)}. \tag{2.100}$$

Thus, the rate equation for the ion concentrations in the astrocyte Eq. (2.91) can be replaced by the constraint Eq. (2.100). In the open system, mass conservation constraint Eq. (2.94) does not hold any more, the extracellular ion concentrations have to be modeled using rate equation Eq. (2.88). The full set of rate equations reads

$$\frac{\partial n}{\partial t} = \frac{n_\infty - n}{\tau_n}, \tag{2.101}$$

$$\frac{\partial c_j^n}{\partial t} = -z_j \frac{\gamma}{\omega_n} I_j^n, \tag{2.102}$$

$$\frac{\partial c_j^e}{\partial t} = z_j \frac{\gamma}{\omega_a} \left(I_j^n + I_j^a \right). \tag{2.103}$$

These rate equations are complemented by the following constraints,

$$m = m_\infty(V), \tag{2.104}$$

$$h = 1 - \frac{1}{1 + \exp(-6.5(n - 0.35))}, \tag{2.105}$$

$$V_m^n = \frac{1}{2C_m\gamma} \left(\rho_n - \rho_e \right), \tag{2.106}$$

$$V_m^a = \frac{1}{2C_m\gamma} \left(\rho_a - \rho_e \right), \tag{2.107}$$

with ρ_a being static.

Provided that the amount of each ionic species in the ICS and in the ECS is constant, $c_j^e/\omega_e + c_j^n/\omega_n = const.$, the system is monostable. The single stable fixed point is the polarized state, because the currents crossing the astrocytic membrane only vanish if the ion concentration in the ECS is in the polarized equilibrium state. However, in the open system, the amount of dynamic ions in the ECS and in the NCS, $c_j^e/\omega_e + c_j^n/\omega_n$, is not conserved. Phase space structure depends on the amount of each ionic species in the system, thus due to changes in the amount of ions the number, position and stability of the fixed points can change.

Analyzing, how fast the glial bath buffers the system from the depolarized state of the two-compartmental model Eqs. (2.42)-(2.47) to the polarized state, we find that, compared to the system where the ion concentration in a small glial compartment (e.g., $\omega_a = \omega_n$) is dynamic Eqs. (2.89)-(2.96), the relaxation is faster, Fig. 2.8(b). This is due to the fact that in the glial bath, in contrast to a small glial compartment, excess ions do not accumulate. Thus, ion buffering from the ECS to the ACS is facilitated and perturbations recover faster.

2.4.4 Examples of time course during relaxation

Here, some examples of the temporal evolution during the relaxation of the system from a depolarized state with largely depleted ion gradients to the polarized physiological state are presented. Examples are shown for two model descriptions, first for the three-compartmental system (see Sect. 2.4.1) consisting of a NCS, an ECS and an ACS, which is a closed system, and second for the two-compartmental system (see Sect. 2.4.3) consisting of a NCS and an open ECS, excess ions are buffered by a glial bath.

In Sect. 2.3, we proposed three different mathematical formulations for the neuronal and astrocytic membrane potential. Here, we pay special attention to the influence of the mathematical description of the membrane potentials on the temporal evolution of the system. In detail, we initialize the particular system in the depolarized state of the bistable two-compartmental model Eqs. (2.42)-(2.46) and analyze for different mathematical descriptions of the membrane potentials, Eq. (2.66), Eq. (2.67) and Eqs. (2.68),(2.69), if the system recovers to the polarized state and, in addition, if the description provides electroneutrality in all considered compartments.

The closed three-compartmental model with convenient parameter values recovers to the polarized physiological state after a period of depolarization for all analyzed descriptions of the membrane potentials V_m^n and V_m^a, Fig. 2.11(a). Describing the membrane potential with Eq. (2.67) ($V_m^{n,a} \sim (\rho_{n,a} - \rho_e)$) results in the longest relaxation time. The open two-compartmental model recovers for two of the three analyzed descriptions of the membrane potentials. The period of depolarization is much shorter than in the closed three-compartmental model.

Next, we discuss with the help of the shown examples the influence of the mathematical description of the membrane potentials on electroneutrality.

$\boldsymbol{V_m^{n,a} \sim \rho_{n,a}}$ Calculating the membrane potential of the neuron and of the astrocyte with

$$V_m^{n,a} = \frac{1}{C_m\gamma}\rho_{n,a} \tag{2.108}$$

determines electroneutrality in the NCS and in the ACS,

$$\rho_{n,a} = C_m\gamma V_m^{n,a} \approx 0, \tag{2.109}$$

compare red curves in Fig. 2.11(a),(b).

In a closed system, this implies electroneutrality in the ECS, as due to mass conservation charge conservation is determined,

$$\rho_e = -\rho_n - \rho_a, \tag{2.110}$$

compare Fig. 2.11(a).

In an open system, however, mass conservation does not hold. Thus, in the ECS, electroneutrality is not determined, compare Fig. 2.11(b), red curves. In the analyzed example, mass exchange with the bath results in a failure of recovery of the neuronal membrane potential.

$\boldsymbol{V_m^{n,a} \sim (\rho_{n,a} - \rho_e)}$ Calculating the membrane potential of the neuron and of the astrocyte with

$$V_m^{n,a} = \frac{1}{2C_m\gamma}(\rho_{n,a} - \rho_e) \tag{2.111}$$

determines an approximate equality of charges in the NCS, in the ECS and in the ACS,

$$\rho_{n,a} - \rho_e = 2C_m\gamma V_m^{n,a} \approx 0, \tag{2.112}$$

$$\rho_{n,a} \approx \rho_e. \tag{2.113}$$

In a closed system, this is only possible under electroneutral conditions in all compartments, compare Fig. 2.11(a), green curve respectively.

However, in an open system, electroneutrality might be violated, e.g., if not-electroneutral transmembrane currents or, in a spatially extended system, not-electroneutral lateral currents occur and, as a consequence, the charges in all compartments change simultaneously. But in the example analyzed here, we fixed the charges in the bath electroneutrally, thus electroneutrality holds in the NCS and in the ECS, see green curves in Fig. 2.11(b).

$\boldsymbol{V_m^{n,a} \sim (\rho_{n,a} - G_{n,a} \cdot \rho_e)}$ Next, we describe the membrane potential of the neuron and of the astrocyte with

$$V_m^n = \frac{1}{2C_m\gamma}(\rho_n - G\rho_e), \tag{2.114}$$

$$V_m^a = \frac{1}{2C_m\gamma}(\rho_a - (1-G)\rho_e), \tag{2.115}$$

$G \in [0, 1]$ is calculated with Eqs. (2.75)-(2.77).

In a closed system, this equals the description Eq. (2.108), as explained in Sect. 2.3. Thus, in Fig. 2.11(a), the course of the blue curves equals the course of the red curves.

In an open system,

$$\begin{aligned}\rho_n - G\rho_e &= 2C_m\gamma V_m^n \approx 0, && (2.116)\\ \rho_a - (1-G)\rho_e &= 2C_m\gamma V_m^a \approx 0, && (2.117)\\ \rho_n &\approx G\rho_e, && (2.118)\\ \rho_a &\approx (1-G)\rho_e. && (2.119)\end{aligned}$$

With $G \not\approx 0$ and $G \not\approx 1$, this implies in the scale of $2C_m\gamma$

$$\rho_n \approx \rho_e \approx \rho_a \tag{2.120}$$

and thus, as in the last discussed description Eq. (2.111), electroneutrality only holds necessarily if in one compartment charges are conserved.
If, however, $G = 1$,

$$\begin{aligned}\rho_n &= \rho_e, && (2.121)\\ \rho_a &= 0 && (2.122)\end{aligned}$$

holds. This might cause not-electroneutral results in the NCS and in the ECS simultaneously.
If $G = 0$,

$$\begin{aligned}\rho_n &= 0, && (2.123)\\ \rho_a &= \rho_e && (2.124)\end{aligned}$$

holds. This also might violate electroneutrality, in this case in the ACS and in the ECS. But if in one compartment, in the ECS or in the ACS, charges are conserved, this condition determines electroneutrality.
In the example shown in Fig. 2.11(b), however, $G \not\approx 1$ all the time during relaxation, see Fig. 2.12, and, in addition, ρ_a is fixed, what implies electroneutrality for $G = 0$.

Concluding we found that the description of the membrane potentials Eq. (2.108) ($V_m^{n,a} \sim \rho_{n,a}$) only provides electroneutrality in closed systems, but fails in open systems. The description Eqs. (2.114),(2.115) ($V_m^{n,a} \sim (\rho_{n,a} - G_{n,a} \cdot \rho_e)$) is the physically most reasonable one. In closed systems it equals the description $V_m^{n,a} \sim \rho_{n,a}$. However, in open systems, for $G = 1$ it fails. The description Eq. (2.111) ($V_m^{n,a} \sim (\rho_{n,a} - \rho_e)$), which averages the compartments into single points, for open systems provides electroneutrality in all compartments if the extra condition that in one compartment charge concentration is fixed holds.

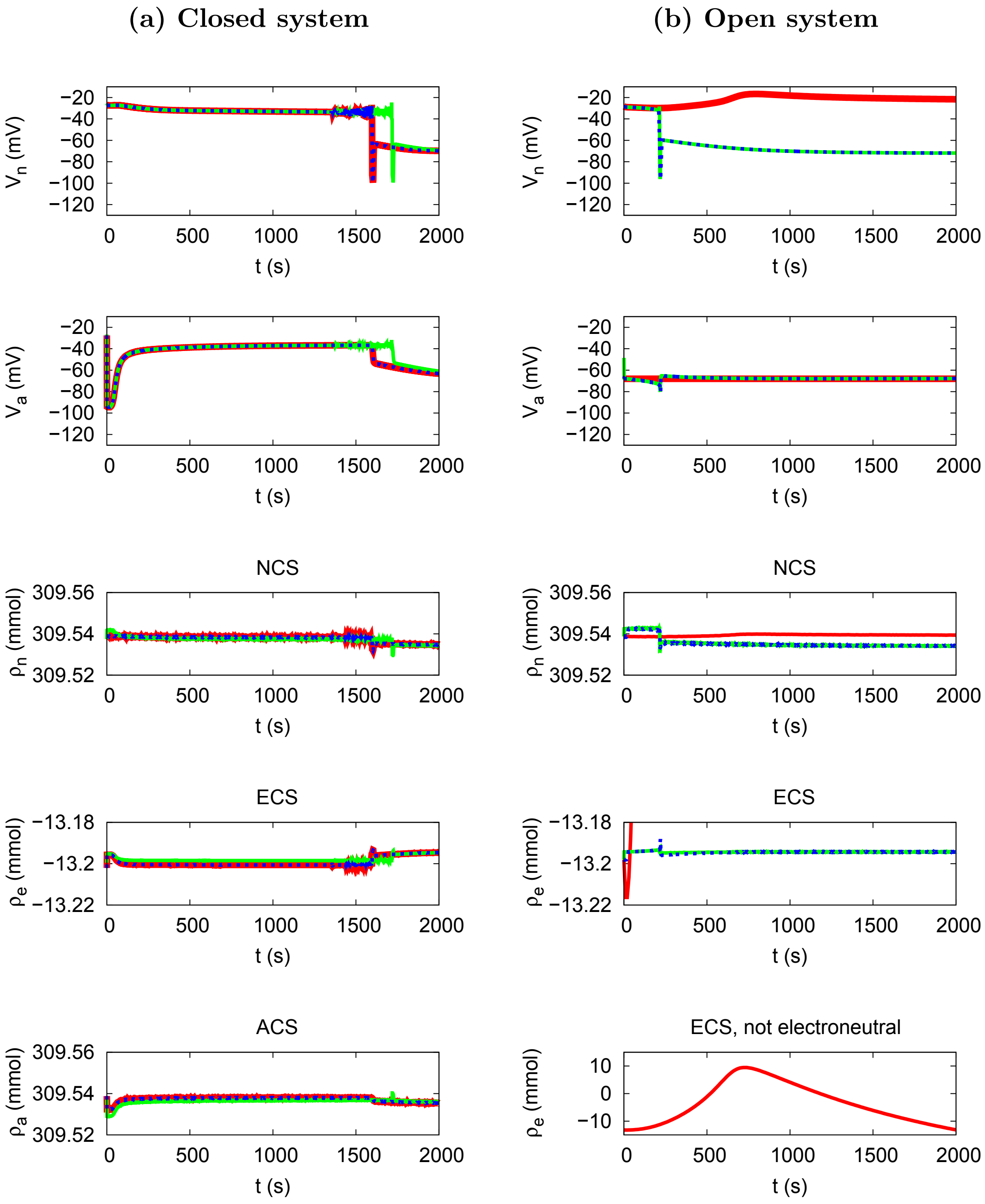

FIGURE 2.11: Temporal evolution during relaxation. The system is initialized in the depolarized state of the bistable two-compartmental model Eqs. (2.42)-(2.46) (Sect. 2.1), and at $t = 0$, the astrocytic currents Eqs. (2.80)-(2.82) are switched on. The membrane potentials at the neuron and the astrocyte are calculated with Eq. (2.108) $V_m^{n,a} \sim \rho_{n,a}$ (solid red curve), Eq. (2.111) $V_m^{n,a} \sim (\rho_{n,a} - \rho_e)$ (solid green curve) and Eqs. (2.114),(2.115) $V_m^n \sim (\rho_{n,a} - G_{n,a}\rho_e)$ (dashed blue curve). You see the neuronal membrane potential V_m^n, the astrocytic membrane potential V_m^a and the sum over the permeable charges in the NCS, in the ECS and in the ACS. In the closed system, the dynamic ion concentrations in the ACS c_j^a are calculated with Eq. (2.87) with $\omega_a = \omega_n$. In the open system, the ACS is modeled as a bath, Eq. (2.100). $C_a = 0.5$.

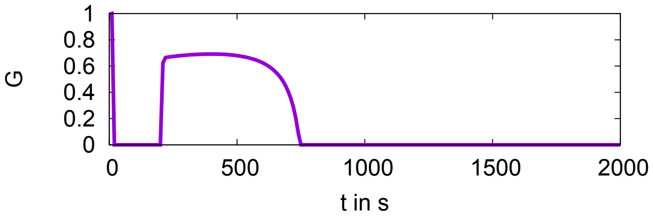

Figure 2.12: Temporal evolution of G Eqs. (2.75)-(2.77) during the relaxation process shown in the blue dashed curve in Fig. 2.11(b).

2.5 Conclusion

In this chapter, we carefully introduced a local neuronal model for CSD. We start from a two-compartmental HH-type model consisting of neurons surrounded by a closed extracellular space [24]. The transmembrane currents considered are leak, gated and pump currents. The model with time-dependent ion-concentrations is bistable, besides the physiological state with polarized membrane potential a second stable state with depolarized membrane potential and largely depleted ion gradients exists. This pathological state is associated with the depolarization during CSD. We reviewed this model and showed that the bistability is quite robust under changes of strength and dynamics of the gated currents.

The bistable system once excited in the depolarized state does not recover to the polarized state any more [24]. During CSD, however, the depolarization is transient. Buffering of excess ions in the extracellular space by astrocytes plays a crucial role in relaxation. Thus, we introduced a third compartment, the glia cells. We found that in the three-compartmental system in a wide parameter range the depolarized state is transient or nonexistent. Then, every excitation recovers to the polarized state.

Furthermore, a simplified description of the buffer is proposed, namely to approximate the glia cells as a bath. In this open system, the total amount of each ionic species is dynamic. However, phase space structure depends on the amount of ions in the system. If the amount of ions equals the initial values used throughout this thesis, the system is monostable. Then, the astrocytic bath is a strong buffer, because there is no ion accumulation in the astrocyte.

In addition, the problem of electroneutrality is addressed. We showed that, especially in open systems, the mathematical description of the neuronal and glial membrane potential plays a crucial role in charge distribution and discussed advantages and disadvantages of different descriptions.

Chapter 3

A biophysically detailed reaction-diffusion model

In this chapter, we compose a spatially continuously extended neuronal model that describes transport processes on a tissue level. For this purpose, the single-neuron elements consisting of a NCS, an ECS and an ACS are spatially coupled in a 1D geometry.

In brain tissue, ions can move within the neuronal net, within the astrocytic syncytium and within the extracellular space. According to Grafstein's hypothesis from 1963 [25] that propagation of CSD mainly is due to extracellular diffusing potassium, we model ion movement in the extracellular space with porous media theory. The spatial coupling among the single elements thus is given by extracellular diffusing ions. Thereby, diffusion is treated as isotropic. To carefully compose the reaction-diffusion model, we first couple the two-compartmental bistable elements (proposed in Sect. 2.1) consisting of a NCS and an ECS by extracellular diffusing ions, Sect. 3.1. Thereby, we pay special attention to electroneutrality, Sect. 3.1.1. In detail, we discuss, how to model electroneutral transmembrane currents in the open elements, Sect. 3.1.1.1, and, in addition, we analyze, how to describe electroneutral lateral currents, Sect. 3.1.1.2.

Then, the three-compartmental elements (proposed in Sect. 2.4) are spatially coupled, Sect. 3.2. Thereby, we analyze whether lateral diffusion manages to maintain ionic homeostasis. First, we investigate the role of extracellular diffusion on clearance of excess ions, Sect. 3.2.1. Besides diffusing in the ECS, ions can move through glial gap junctions. The gap-junctional coupling can be approximated by isotropic diffusion [72, 73]. Thus, second we analyze the role of astrocytic gap junctions on clearance of excess ions, Sect. 3.2.2. Then, as proposed in Sect. 2.4.3, the astrocytic compartment is assumed to be a bath, Sect. 3.2.3. In addition, electroneutrality in this system is shortly discussed, Sect. 3.2.4.

In brain, signal transmission within the neuronal net is mostly due to chemical synapses. However, action potentials occur on a much shorter timescale than CSD. Furthermore, during the depolarization of CSD, no action potentials are generated. Thus, we argue that in a model for CSD, spatial coupling among the neurons by chemical synapses can be neglected. However, neuronal coupling is not solely given by chemical synapses, but also few electrical synapses (gap junctions) can be found. We show, how propagation of CSD is affected by neuronal gap junctions, Sect. 3.3.

3.1 Diffusive spatial coupling of bistable two-compartmental elements

Here, a spatially continuously extended model consisting of bistable two-compartmental elements Eqs. (2.42)-(2.46) is designed. Thereby, spatial coupling is modeled by extracellular diffusing ions.

The single elements spatially coupled by diffusion are open systems, local mass conservation does not hold. Thus, in addition to the rate equations describing the ion concentrations in the NCS, the concentration of each ionic species in the ECS has to be calculated with a partial differential equation. The full set of rate equations of the two-compartmental reaction-diffusion model reads

$$\frac{\partial n}{\partial t} = \frac{n_\infty - n}{\tau_n}, \tag{3.1}$$

$$\frac{\partial c_j^n}{\partial t} = -z_j \frac{\gamma}{\omega_n} I_j^n, \tag{3.2}$$

$$\frac{\partial c_j^e}{\partial t} = z_j \frac{\gamma}{\omega_e} I_j^n + D_j^e \frac{\partial^2 c_j^e}{\partial x^2}. \tag{3.3}$$

The diffusion coefficient of each ion in brain tissue D_j is assumed to equal the diffusion coefficient of the respective ion in aqueous solution. As the path in the ECS is increased due to the tortuosity λ_e, the effective diffusion coefficient reads

$$D_j^e = \frac{D_j}{\lambda_e^2}. \tag{3.4}$$

The literature values for the diffusion coefficients of sodium, potassium and chloride in aqueous solution are $D_{Na} = 1.3 \cdot 10^{-5}$ cm^2/s, $D_K = 1.96 \cdot 10^{-5}$ cm^2/s and $D_{Cl} = 2.03 \cdot 10^{-5}$ cm^2/s. Here, the diffusion coefficients of potassium and chloride are approximated with $D_{K,Cl} = 2.0 \cdot 10^{-5}$ cm^2/s, whereas the diffusion coefficient of sodium is approximated with $D_{Na} = 0.66 \cdot D_{K,Cl}$. The tortuosity of the ECS is chosen to be $\lambda_e = 1.6$. The parameter values are listed in Tab. 2.1.

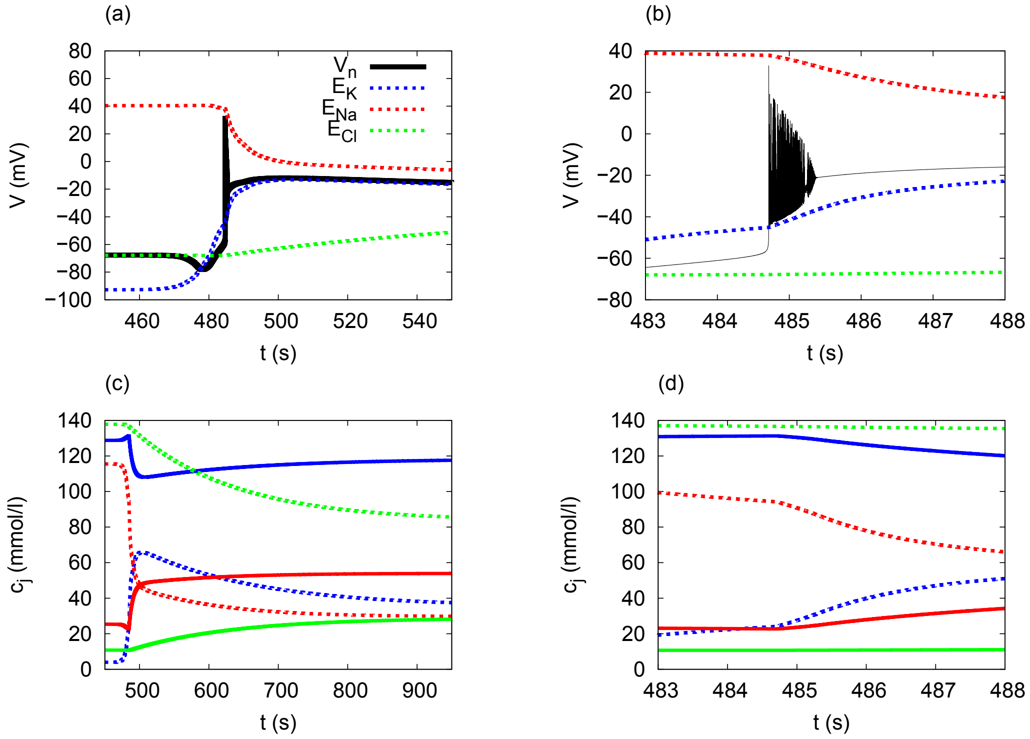

FIGURE 3.1: Example of a propagating front solution as a function of time t calculated with the spatially extended system Eqs. (3.1)-(3.3); (a) membrane potential V_m^n and Nernst potentials E_j; (b) inset at the rising front shows characteristic initial bursting; (c) ion concentration of K (blue), Na (red) and Cl (green), each in the NCS (solid) and in the ECS (dashed); (d) inset shows variation of ion concentrations at the front; $D_{Na} = D_K = D_{Cl} = 2.0 \cdot 10^{-5}$ cm^2/s.

The system consisting of bistable elements has two stable homogeneous solutions, the polarized and the depolarized state, compare Fig. 2.1. In reaction-diffusion models, besides homogeneous solutions, inhomogeneous solutions exist. We are interested in stable stationary propagating solutions, i.e., waves that propagate with constant velocity and constant shape. Here, the stationary propagating solution is a front solution, i.e., a solution that connects the two stable homogeneous states, see Fig. 3.1. At the rising front, bursting characteristic for CSD can be seen, Fig. 3.1(b). In the depolarized state, ion gradients are largely depleted, Fig.3.1(c). The transition of the ion concentrations $c_j^{n,e}$ from the physiological to the pathological equilibrium lasts several seconds, Fig.3.1(d).

Initializing the system in the homogeneous polarized state, a localized excitation, that is super-threshold in a combination of strength, duration and width, depolarizes the membrane potential in the affected area. The depolarization then spreads with constant propagation velocity c in both the positive and the negative x-direction. Thereby, area once affected does not recover to the polarized state any more, but remains in the depolarized state. Thus, lateral diffusion of ions in the ECS here is not sufficient for ionic homeostasis.

3.1.1 Electroneutrality

We propose to model ion movement in brain tissue by diffusive fluxes in the ECS. Positive and negative charged particles are considered, Na^+, K^+ and Cl^-. The strong electrical forces between the charged particles thereby cannot be neglected. As charge separation is not reasonable, local electroneutrality in the ECS is requested, i.e., at every location the sum over the charges is zero.

Charge distribution depends on both, transmembrane and lateral currents. First, we show, how electroneutrality of the transmembrane currents in this system composed of open elements is affected by the mathematical description of the membrane potential V_m^n, Sect. 3.1.1.1. Then, we discuss, how electroneutral diffusion in the ECS can be realized, Sect. 3.1.1.2.

Be aware that if the lateral diffusive currents are electroneutral, local charge conservation holds and thus the local elements act like closed elements in matters of electroneutrality. This implies that, independent of the description of the membrane potential, the sum over the transmembrane currents at each element is electroneutral, compare Sect. 2.3.

3.1.1.1 Electroneutral transmembrane currents

In Sect. 2.4.4, we showed, how the charge distribution in open two-compartmental local elements is determined by the particular mathematical description of the neuronal membrane potential V_m^n. Here, we discuss with the help of examples, how the charge distribution due to transmembrane currents in open two-compartmental elements spatially coupled by diffusion depends on the particular mathematical description of the neuronal membrane potential V_m^n. Therefore, we model the lateral diffusive currents not-electroneutral. This theoretical construct is physically not reasonable, but helps to understand the influence of the model description on the transmembrane currents, what is of importance in open systems.

In Sect. 2.3, we proposed three different formulations for the neuronal membrane potential V_m^n. In a closed system with charge conservation and convenient initial conditions ($\rho_n = -\rho_e$), they are equivalent. However, in an open system, where charge conservation is violated, they differ. Next, we shortly reconsider the three possibilities to describe the membrane potential and discuss, how electroneutrality is affected in the reaction-diffusion model.

$\boldsymbol{V_m^n \sim \rho_n}$ Calculating the neuronal membrane potential with

$$V_m^n = \frac{1}{C_m \gamma} \rho_n \tag{3.5}$$

determines electroneutrality in the NCS,

$$\rho_n = C_m \gamma V_m^n \approx 0, \tag{3.6}$$

but not in the ECS, compare Fig. 3.2(a).

$\boldsymbol{V_m^n \sim -\rho_e}$ Calculating the neuronal membrane potential with

$$V_m^n = -\frac{1}{C_m \gamma} \rho_e \tag{3.7}$$

determines electroneutrality in the ECS,

$$\rho_e = -C_m \gamma V_m^n \approx 0. \tag{3.8}$$

but not in the NCS, compare Fig. 3.2(b).

$\boldsymbol{V_m^n \sim (\rho_n - \rho_e)}$ Calculating the neuronal membrane potentials with

$$V_m^n = \frac{1}{2 C_m \gamma} (\rho_n - \rho_e) \tag{3.9}$$

determines an approximate equality of charges in the NCS and in the ECS,

$$\begin{aligned} \rho_n - \rho_e &= 2 C_m \gamma V_m^n \approx 0, & (3.10) \\ \rho_n &\approx \rho_e, & (3.11) \end{aligned}$$

compare Fig. 3.2(c).

Not-electroneutral lateral diffusive currents here are realized by different diffusion coefficients D_j for the ionic species. The diffusion coefficients of potassium and chloride are approximated with $D_{K,Cl} = 2.0 \cdot 10^{-5}$ cm^2/s, whereas the diffusion coefficient of sodium is approximated with $D_{Na} = 0.66 \cdot D_{K,Cl}$. Varying the strength of D_{Na} affects front propagation. This can be seen in the bifurcation diagram Fig. 3.3. The propagation velocity c of front solutions calculated with Eqs. (3.1)-(3.3) as a function of the diffusion coefficient of sodium D_{Na} (with constant D_K and D_{Cl}) is shown for each description of the membrane potential V_m^n proposed here.

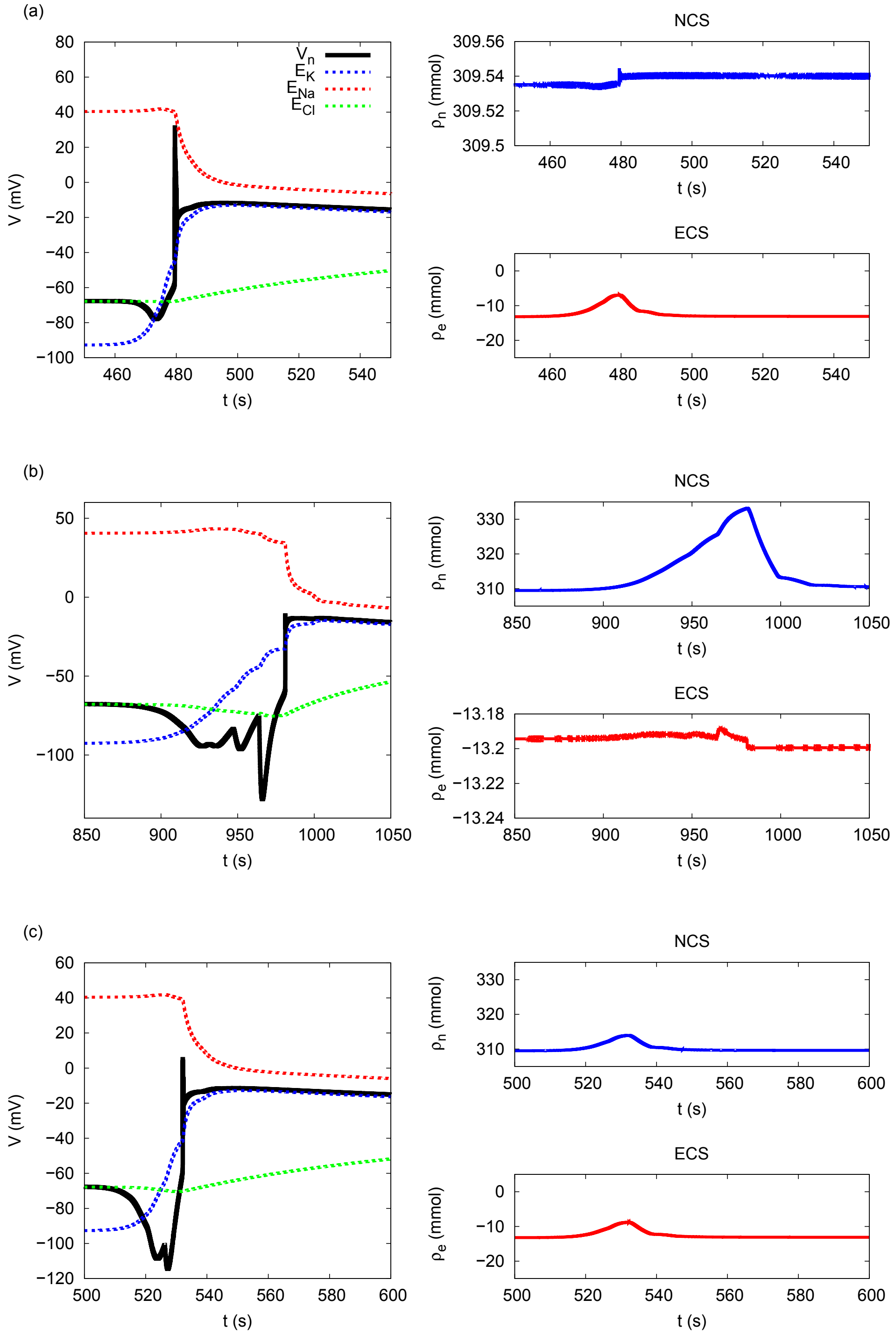

FIGURE 3.2: (a) Temporal evolution of neuronal membrane potential V_m^n (black, solid) and Nernst potential E_j of each ionic species (coloured dashed) of a propagating front solution calculated with Eqs. (3.1)-(3.3). In addition, you see the sum over permeable charges in the NCS and in the ECS. The lateral diffusive currents are not-electroneutral ($D_K = D_{Cl} = 2.0 \cdot 10^{-5}$ cm^2/s, $D_{Na} = 0.66 \cdot D_K$). (a) The membrane potential is assumed to be proportional to the amount of charges in the NCS ($V_m^n \sim \rho_n$), Eq. (3.5). This description determines electroneutrality in the NCS, but not in the ECS. (b) The membrane potential is assumed to be proportional to the amount of charges in the ECS ($V_m^n \sim \rho_e$), Eq. (3.7). This description determines electroneutrality in the ECS, but not in the NCS. (c) The membrane potential is assumed to be proportional to the difference between the amount of charges in the NCS and the amount of charges in the ECS ($V_m^n \sim (\rho_n - \rho_e)$), Eq. (3.9). This description determines charge equality in the NCS and in the ECS.

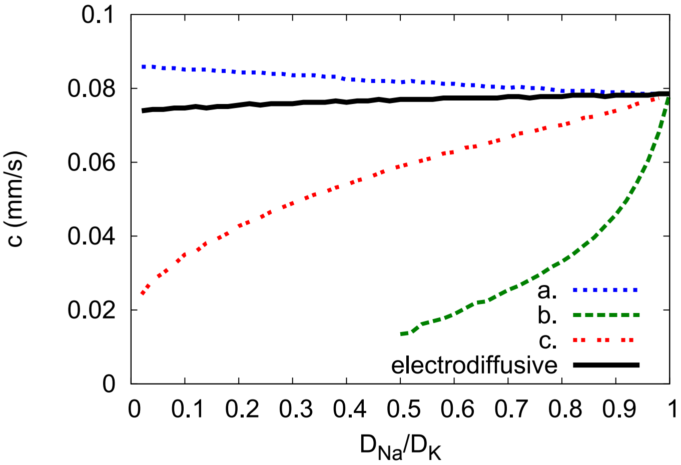

FIGURE 3.3: Propagation velocity c of propagating front solutions calculated with Eqs. (3.1)-(3.3) as a function of the diffusion coefficient D_{Na}; the membrane potential V_m^n is described by Eq. (3.5) ($V_m^n \sim \rho_n$) (a), Eq. 3.7 ($V_m^n \sim -\rho_e$) (b) and Eq. (3.9) ($V_m^n \sim (\rho_n - \rho_e)$) (c). The black solid line shows the propagation velocity using the locally electroneutral electrodiffusive description, Sect. 3.1.1.2. In this case, results are independent from the description of the membrane potential V_m^n. $D_K = D_{Cl} = 2.0 \cdot 10^{-5}$ cm^2/s.

The formulation Eq. (3.5) ($V_m^n \sim \rho_n$) results in the fastest front solutions. This is due to the fact that electroneutrality in the ECS is not determined, what is in accordance with the chosen not-electroneutral lateral diffusion. As Eq. (3.5) determines electroneutrality in the NCS, the transmembrane currents are electroneutral.

The formulation Eq. (3.7) ($V_m^n \sim \rho_e$) disturbes propagation massively. You can see this first in the crude course of the membrane potential, Fig. 3.2(b) and second in the comparatively slow propagation velocity, Fig. 3.3, which strongly depends on the relation between the diffusion coefficients of sodium and potassium, D_{Na}/D_K. The disturbance is caused by two contradicting constraints: on the one hand, electroneutrality in the ECS is determined by Eq. (3.7), on the other hand, the lateral diffusive currents in the ECS are chosen not-electroneutral. Thus, at every timestep, electroneutrality in the ECS has to be ensured by transmembrane currents, what impedes propagation massively.

Using the formulation Eq. (3.9) ($V_m^n \sim (\rho_n - \rho_e)$) to calculate the membrane potential determines charge equality in both, the NCS and the ECS. As the not-electroneutral diffusion inhibits electroneutrality in the ECS, also the NCS is not electroneutral.

Electroneutral diffusive currents are required to get electroneutrality in both compartments, the NCS and the ECS. How this can be achieved, is discussed in the following, Sect. 3.1.1.2.

3.1.1.2 Electroneutral lateral currents

Electrodiffusion treats a nonlinear transport process whose essence is diffusion of charged particles. Basic equations for motion of ions in a self-consistent electrical field were already formulated by Nernst and Planck. Over 100 years later, in 1990, Rubinstein proposed a formalism to describe electroneutral electrodiffusion [30]. In a first assumption, this formalism is a good approximation for ion movement in brain tissue, as it avoids charge separation due to diffusion.

In the two-compartmental model spatially coupled by diffusing ions in the ECS Eqs. (3.1)-(3.3), changes of the extracellular ion concentration are due to transmembrane currents and lateral diffusive currents,

$$\frac{\partial c_j^e}{\partial t} = z_j \frac{\gamma z_j}{\omega_e} \left(I_j^n + I_j^{Diff} \right), \tag{3.12}$$

with I_j^n being the transmembrane gated, leak and pump currents of species j and I_j^{Diff} being the diffusive current of species j in the ECS. In [30], it is proposed to replace I_j^{Diff} by the Nernst-Planck equation, which states that the forces causal for movement of ions in an electrical field can be approximated by a superposition of forces due to the chemical gradient and forces due to the electrical gradient,

$$I_j^{Diff} = z_j \frac{\omega_e}{\gamma} D_j^e \left(\frac{\partial}{\partial x} \left(\frac{\partial c_j^e}{\partial x} + z_j \frac{F}{RT} c_j^e \frac{\partial \Phi^e}{\partial x} \right) \right). \tag{3.13}$$

Electroneutral electrodiffusion means that the sum over the diffusive currents equals zero, thus

$$\sum_j I_j^{Diff} \overset{!}{=} 0, \tag{3.14}$$

and hence

$$0 = \frac{\partial}{\partial x} \left(A + B \frac{\partial \Phi^e}{\partial x} \right), \tag{3.15}$$

with

$$A = \sum_j \left(z_j D_j^e \frac{\partial c_j^e}{\partial x} \right), \tag{3.16}$$

$$B = \sum_j \left(z_j^2 D_j^e \frac{F}{RT} c_j^e \right). \tag{3.17}$$

With no-flux boundaries, therefrom follows

$$0 = A + B\frac{\partial \Phi^e}{\partial x} \tag{3.18}$$

and thus

$$\frac{\partial \Phi^e}{\partial x} = -\frac{A}{B}. \tag{3.19}$$

Be aware that the electroneutral electrodiffusive description only is valid if the sum over the transmembrane currents equals zero,

$$\sum_j I_j^n = 0. \tag{3.20}$$

As due to electroneutral diffusion local charge conservation holds, all descriptions of the membrane potential V_m^n proposed in Sect. 3.1.1.1 are equivalent (see Sect. 2.3) and determine that Eq. (3.20) is valid. Thus, in the system described by Eqs. (3.1)-(3.3), from electroneutral diffusion in the ECS follows electroneutrality in both compartments, the NCS and the ECS. In models with

$$\sum_j I_j^n \neq 0, \tag{3.21}$$

electroneutral diffusion is physically not reasonable, as charge gradients in the ECS caused by transmembrane currents would be cleared due to electrical forces.

Modeling the spatial coupling with the electroneutral electrodiffusive description, electroneutrality in both compartments, the NCS and the ECS, holds. This can be seen in Fig. 3.4(a), where the profile of the membrane potential V_m^n of a front and, in addition, the corresponding time course of the sum over permeable charges in both compartments, the NCS and the ECS, are shown. The propagation velocity c of the front solution thereby only depends slightly on the relation between the diffusion coefficients of sodium and potassium D_{Na}/D_K, see Fig. 3.3 (solid black line).

Electroneutrality in the ECS means that the sum over the charges in the ECS at each location equals zero. This implies that the gradient of the charges ρ_e with respect to space x is zero, $\frac{\partial \rho_e}{\partial x} = \omega_e \sum_j \left(z_j \frac{\partial c_j^e}{\partial x} \right) = 0$. Thus, with zero transmembrane currents $\sum_j I_j^n = 0$ and electroneutral initial conditions, electroneutral diffusion can be achieved by the approximation that the diffusion coefficients of all ions are equal, $D_{Na} = D_K = D_{Cl}$. Then, $A = 0$ and thus the electrical gradient in the Nernst-Planck equation vanishes.

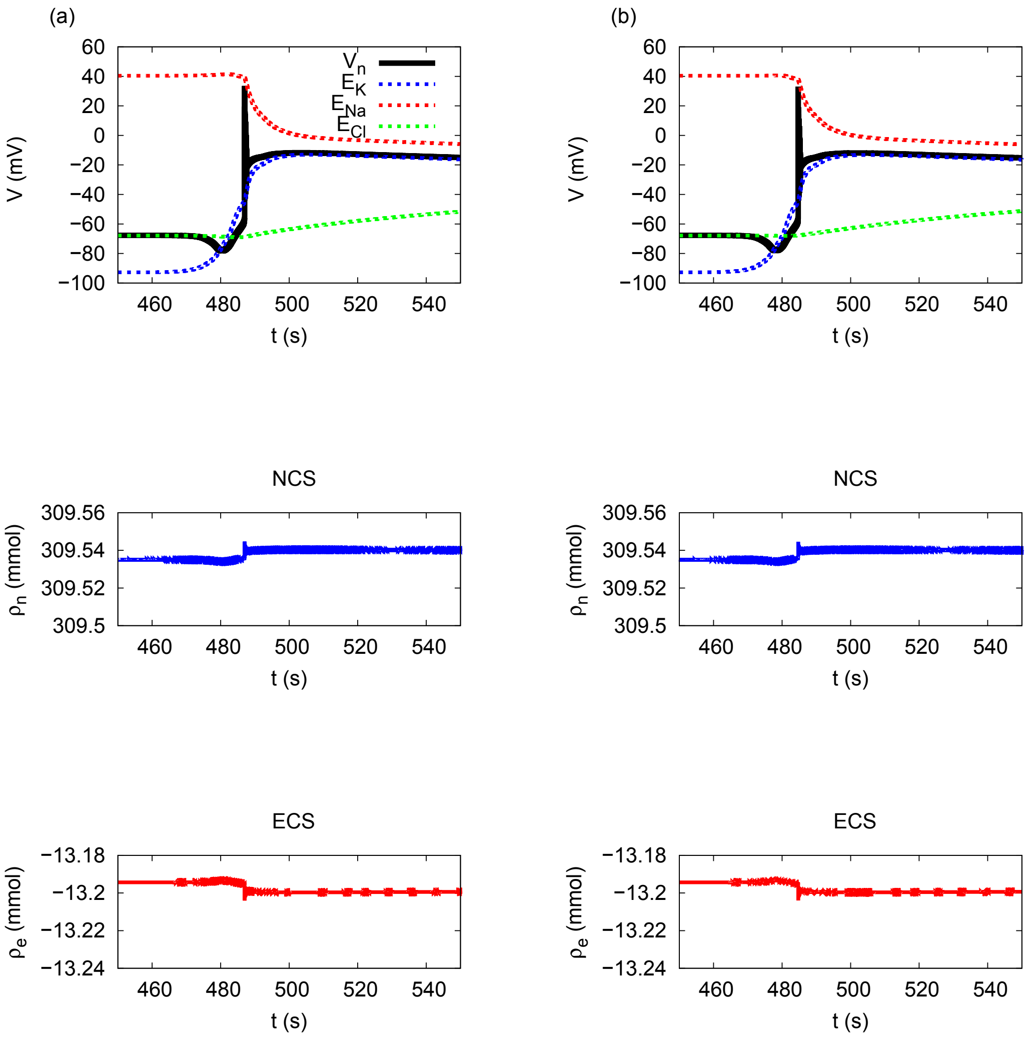

FIGURE 3.4: (a) Temporal evolution of neuronal membrane potential V_m^n (black, solid) and Nernst potential E_j of each ionic species (coloured, dashed) of a propagating front solution calculated with Eqs. (3.1)-(3.3). In addition, the corresponding sum over permeable charges in the NCS and in the ECS is shown. (a) The diffusion in the ECS is described by the electroneutral electrodiffusion formalism proposed by Rubinstein. $D_K = D_{Cl} = 2.0 \cdot 10^{-5}$ cm^2/s, $D_{Na} = 0.66 \cdot D_K$. (b) All diffusion coefficients in the ECS are assumed to be equal, $D_{Na} = D_K = D_{Cl} = 2.0 \cdot 10^{-5}$ cm^2/s. Both descriptions provide electroneutrality in both compartments, the NCS and the ECS.

The deviation of the profile of a front solution, where the diffusive currents are calculated with the approximation $D_{Na} = D_K = D_{Cl}$ Fig. 3.4(b) from the profile of a front solution, where the diffusive currents are calculated with the electroneutral electrodiffusive description Fig. 3.4(a) in the shown example are negligible. If $D_{Na} = D_K = D_{Cl}$, the diffusive currents in the ECS are electroneutral and thus charge conservation holds. Therefrom follows that the descriptions of the membrane potential V_m^n Eq. (3.5), Eq. (3.7) and Eq. (3.9) are identical, thus all curves drawn in Fig. 3.3 coincide at $D_{Na}/D_K = 1$.

3.2 Diffusive spatial coupling of three-compartmental elements

In Sect. 3.1, we found that the reaction-diffusion model consisting of bistable elements has propagating front solutions. A super-threshold perturbation excites the system to a depolarized state, that propagates over space. Area once affected remains in the depolarized state and does not recover to the polarized equilibrium any more. During CSD, however, depolarizations usually recover after a time of at most 1000 s. To resolve this, in Sect. 2.4, we proposed uptake of excess ions from the extracellular space by glia cells as regulation mechanism.

Here, we want to identify the effect of lateral diffusive currents on ionic homeostasis. Therefore, a spatial 1D reaction-diffusion model consisting of three-compartmental elements is designed. We analyze, which lateral currents are decisive for existence and type of inhomogeneous solutions, i.e., we vary the strength of the particular lateral currents and analyze whether the system has propagating front solutions, propagating pulse solutions or no stable stationary propagating solution.

To carefully compose the spatially extended model, we first couple the three-compartmental elements by extracellular diffusing ions, Sect. 3.2.1. Then, in Sect. 3.2.2, we also allow for diffusion within the astrocytic syncytium. We analyze, how the strength of the gap-junctional coupling affects propagation of CSD. As proposed in Sect. 2.4.3, the ACS can, due to vascular coupling, be approximated as a bath. We analyze, how this approximation affects propagation of CSD, Sect. 3.2.3. In addition, we shortly discuss electroneutrality in this system, Sect. 3.2.4.

3.2.1 Ion movement in the extracellular space

We are interested in the question whether lateral diffusion of ions in the ECS facilitates relaxation. Here, the three-compartmental elements proposed in Sect. 2.4.1 consisting of a NCS, an ECS and an ACS are spatially coupled by extracellular diffusing ions.

As due to diffusion local mass conservation does not hold any more, the concentrations c_j of the considered ionic species have to be calculated by rate equations in all three compartments.

Including the equation for the gating variable n, the full set of rate equations then reads

$$\frac{\partial n}{\partial t} = \frac{n_\infty - n}{\tau_n}, \tag{3.22}$$

$$\frac{\partial c_j^n}{\partial t} = -z_j \frac{\gamma}{\omega_n} I_j^n, \tag{3.23}$$

$$\frac{\partial c_j^a}{\partial t} = -z_j \frac{\gamma}{\omega_a} I_j^a, \tag{3.24}$$

$$\frac{\partial c_j^e}{\partial t} = z_j \frac{\gamma}{\omega_e} \left(I_j^n + I_j^a \right) + D_j^e \frac{\partial^2 c_j^e}{\partial x^2}. \tag{3.25}$$

As electroneutral diffusion in the ECS is required, we set the diffusion coefficients of all ions equal, compare Sect. 3.1.1.2.

To figure out whether diffusion contributes to ionic homeostasis, we analyze if we find propagating pulse solutions in a parameter regime, where the astrocytic buffer does not manage to recover a single-neuron element from the depolarized state to the polarized state. This parameter regime is the white area in Fig. 3.5(a). We find that diffusion in the ECS does not contribute to ionic homeostasis, compare Fig. 3.5(a) and Fig. 3.5(b). The stationary propagating solution of a system consisting of single-neuron elements, whose glial buffer is too weak to recover the system from a depolarized membrane potential, spatially coupled by extracellular diffusing ions are front solutions.

In the parameter regime where the system is bistable, but the buffer manages to recover the system from the depolarized state ($\omega_a \leqq 0.8 \cdot \omega_n$ and large C_a, compare Sect. 2.4.2), we find coexisting front and pulse solutions. This phenomen also was found in the complex Ginzburg-Landau equation and in the bistable FHN model [74].

At few parameter combinations, where ionic homeostasis of the single-neuron element holds, we find propagating front solutions in the spatially extended system. This deviation is caused by the fact that the depolarized state of the propagating front solution differs from the depolarized stat, in which the single-neuron element is initialized. However, in almost the whole parameter regime where the depolarized state of a single-neuron element is buffered, we find propagating pulse solutions in the spatially extended system. We measure the pulse duration τ as the time, during which at a particular location x the extracellular potassium concentration K_e is larger than 20 mmol/l. We find that the pulse duration approximately equals the relaxation time from the depolarized to the polarized state in a single-neuron element, compare Fig. 3.5(a) and Fig. 3.5(b).

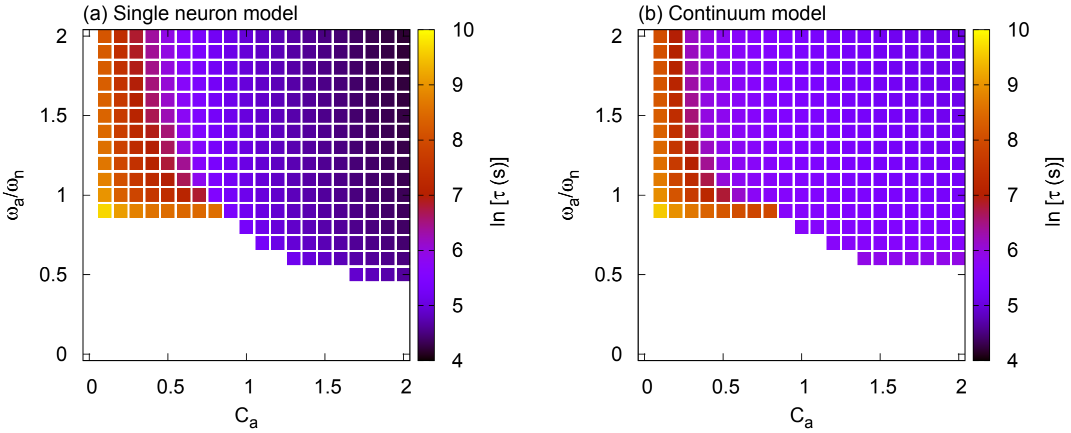

FIGURE 3.5: (a) Relaxation time of three-compartmental single-neuron elements, compare Fig. 2.8. (b) Duration of depolarization τ of propagating pulses computed with three-compartmental elements spatially coupled by diffusing ions in the ECS, Eqs. (3.22)-(3.25), as a function of C_a and ω_a/ω_n (with constant ω_n). In the white region, only propagating front solutions are found. $\tau = t_2 - t_1$, with t_1 being the first time at a specific location x with $K_e > 20$ mmol/l, and t_2 being the first time $t_2 > t_1$ at the same location x with $K_e < 20$ mmol/l. $D_j = 2.0 \cdot 10^{-5}$ cm^2/s.

3.2.2 Glial gap junctions

In the astrocytic syncytium, ions can move through gap junctions. The volume fraction of the glial syncytium is about three times larger than the volume fraction of the extracellular space. Thus, in a model for CSD, ion movement in the ACS cannot be neglected. As proposed in [72, 73], we model ion movement through glial gap junctions by diffusing ions within the astrocytic compartment. The full set of rate equations then reads

$$\frac{\partial n}{\partial t} = \frac{n_\infty - n}{\tau_n}, \tag{3.26}$$

$$\frac{\partial c_j^n}{\partial t} = -z_j \frac{\gamma}{\omega_n} I_j^n, \tag{3.27}$$

$$\frac{\partial c_j^a}{\partial t} = -z_j \frac{\gamma}{\omega_a} I_j^a + D_j^a \frac{\partial^2 c_j^a}{\partial x^2}, \tag{3.28}$$

$$\frac{\partial c_j^e}{\partial t} = z_j \frac{\gamma}{\omega_e} \left(I_j^n + I_j^a \right) + D_j^e \frac{\partial^2 c_j^e}{\partial x^2}. \tag{3.29}$$

In [72], it is proposed to calculate the effective diffusion coefficients in the glial compartment D_j^a with

$$D_j^a = \frac{D_j}{\lambda_a^2}, \tag{3.30}$$

with $\lambda_a = 3.2$. The tortuosity in the ACS is two times larger than the tortuosity in the ECS, see Tab. 2.1. Be aware that the tortuosity in the ACS is not a measure for the convolution of the path, but summarizes the hindrance imposed by the cellular structures. D_j is the diffusion coefficient of the respective ion in aqueous solution, which here as in the ECS is approximated by the values listed in Tab. 2.1. To achieve electroneutral diffusion in the ACS, we set the diffusion coefficients of all ions in the ACS equal,

$$D^a_{Na} = D^a_K = D^a_{Cl}. \tag{3.31}$$

Clearance of excess charges in the ACS is not due to diffusion only, but supported by the connection of the ACS with the vasculature. We approximate this by augmenting the effective diffusion coefficients D^a_j. We analyze, how relaxation depends on the strength of the effective diffusion coefficient D^a_j and, in addition, on the amount of ion channels at the astrocytic membrane C_a, i.e., we measure the pulse duration τ at different parameter values, see Fig. 3.6(a). We find that the pulse width decreases with increasing D^a_j and C_a. In addition, we measure the propagation velocity c of the respective pulse solutions, see Fig. 3.6(b). For very strong buffer (large D^a_j and large C_a), the pulses are very slow. Surprisingly, we find the maximal propagation velocity for $C_a \neq 0$ and relatively large diffusion strength D^a_j. This might be caused by the fast spread of ions in the ACS, which then, apart from the current position of the pulse, cross the astrocytic membrane and get in the ECS and in the NCS, and there facilitate the propagation of the incoming pulse.

The three-compartmental model spatially coupled by diffusion in the ECS and in the ACS has propagating pulse solutions in the whole analyzed parameter regime. An example of the profile of a propagating pulse solution is shown in Fig. 3.7. You see the membrane potential at the neuron and the astrocyte and, in addition, the ion concentrations in all compartments as a function of time. The membrane potential of both, the neuron and the astrocyte, is depolarized. This depolarization, which is caused by a large depletion of ion gradients at the neuronal and at the astrocytic membrane, Figs. 3.7(c),(d), propagates over space. Due to astrocytic ion uptake, excess ions in the ECS are buffered, and thus the membrane potentials V^n_m and V^a_m recover after a period of depolarization. At the rising front, the profiles exhibit short strong bursting, Fig. 3.7(b), what is characteristic for CSD. At the back, you see a long period of weak bursting.

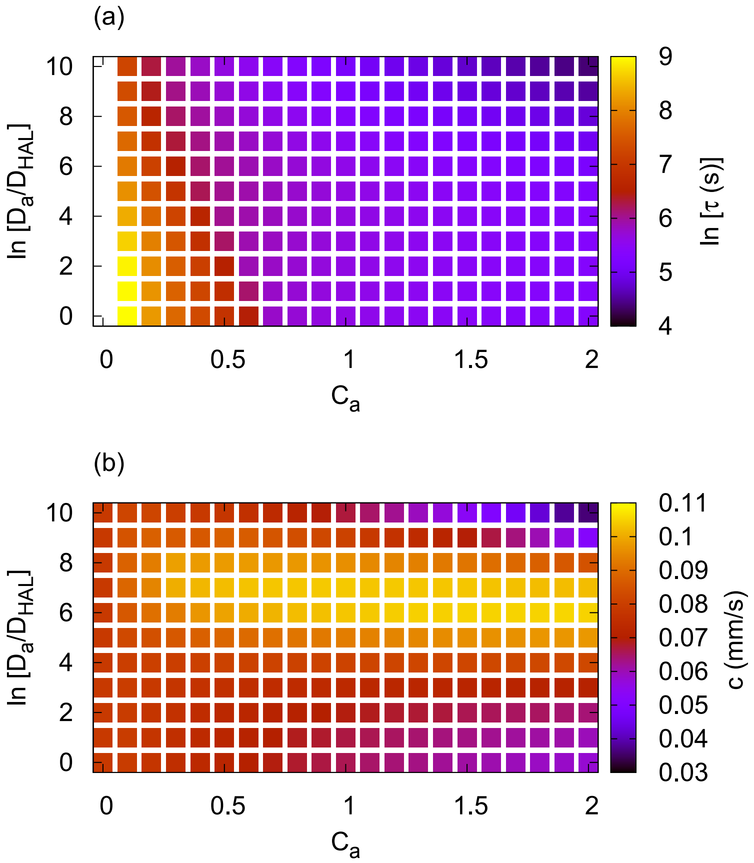

FIGURE 3.6: Duration of depolarization τ (a) and propagation velocity (b) of propagating pulses computed with three-compartmental elements spatially coupled by diffusing ions in the ECS and in the ACS, Eqs. (3.26)-(3.29), as a function of C_a and $\ln(D_j^a/D_{HAL})$ with D_{HAL} being the diffusion coefficient proposed by Halnes, Eq. 3.30. $D_j = 2.0 \cdot 10^{-5}$ cm^2/s for all ionic species; $\tau = t_2 - t_1$, with t_1 being the first time at a specific location x with $K_e > 20$ mmol/l, and t_2 being the first time $t_2 > t_1$ at the same location x with $K_e < 20$ mmol/l.

3.2.3 Glial bath in the reaction-diffusion model

In the limit of an infinitely large glial compartment ($\omega_a \to \infty$), the ACS reduces to a bath, compare Sect. 2.4.3. This is equivalent to the limit of infinitely strong diffusion in the ACS ($D_j^a \to \infty$) if the medium is infinitely extended. The physical meaning of modeling the ACS as a bath is that clearance of excess ions in the ACS is approximated to happen instantaneously.

Approximating the glia compartment as a bath, the ion concentrations c_j^a are not dynamic any more, but model parameters. They are fixed on the initial concentrations, compare Eq. (2.100),

$$c_j^a \quad = \quad c_j^{a(0)}. \qquad (3.32)$$

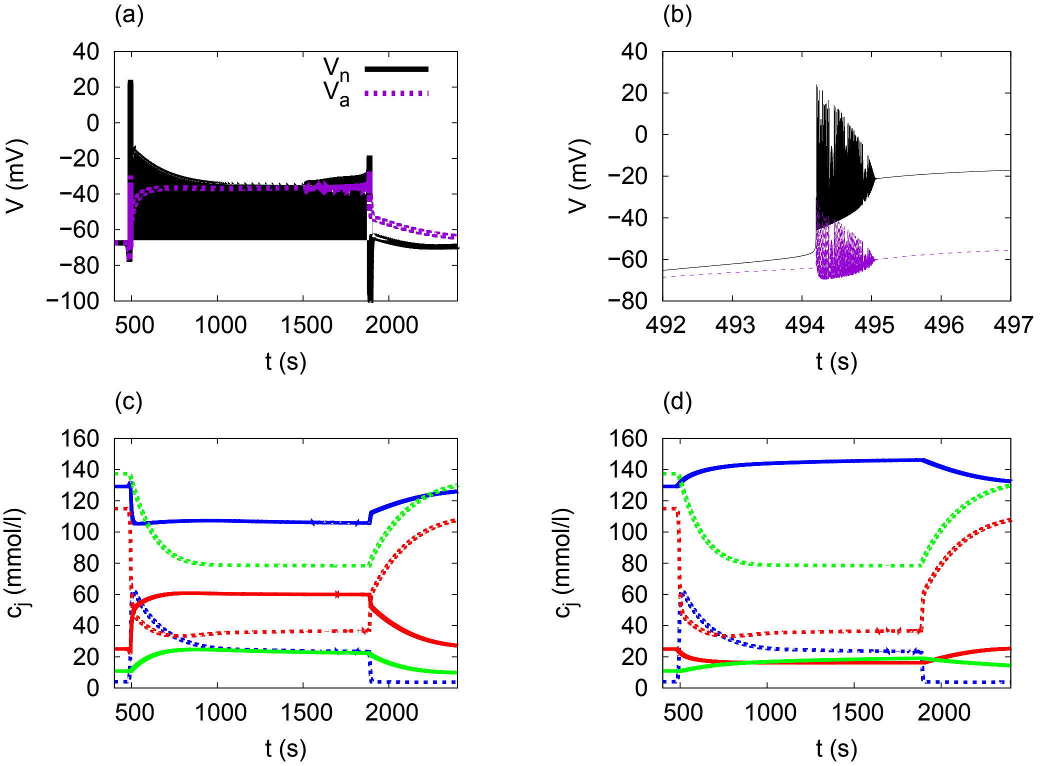

FIGURE 3.7: Temporal evolution of a propagating pulse solution computed with three-compartmental elements spatially coupled by diffusing ions in the ECS and in the ACS, Eqs. (3.26)-(3.29). (a) Neuronal and glial membrane potential; (b) inset at the rising front; (c) ion concentration of K (blue), Na (red) and Cl (green), each in the NCS (solid) and in the ECS (dashed); (d) ion concentration of K (blue), Na (red) and Cl (green), each in the ACS (solid) and in the ECS (dashed). $D_j = 2.0 \cdot 10^{-5}$ cm^2/s, $D_j^e = \frac{D_j}{\lambda_e^2}$, $D_j^a = \frac{D_j}{\lambda_a^2}$, $C_a = 0.5$.

The rate equation for the ion concentrations in the astrocyte Eq. (3.28) is replaced by the constraint Eq. (3.32). Thereby, the number of rate equations reduces from 10 to 7.

Modeling the glial compartment as a bath, the buffer mechanism is increased compared to the model consisting of three-compartmental elements with $D_j^a = \frac{D_j}{\lambda_a^2}$, as excess ions from the ECS are absorbed by the bath, where ions do not accumulate. This can be seen in the much shorter period of depolarization, compare Fig. 3.8(a) to Fig. 3.6(a). However, strong diffusion in the ACS also shortens the period of depolarization, see Fig. 3.6(a).

In a wide parameter regime, we find propagating pulse solutions. An example of a propagating pulse solution is shown in Fig. 3.9. You see, that the astrocytic membrane potential during CSD is hardly depolarized, Fig. 3.9(a). At the rising front and at the back, the membrane potentials of both, the neuron and the astrocyte, exhibit bursting, Fig. 3.9(c),(d). If C_a is increased, the pulsewidth decreases massively, and also the propagation velocity c decreases, Fig. 3.8(b).

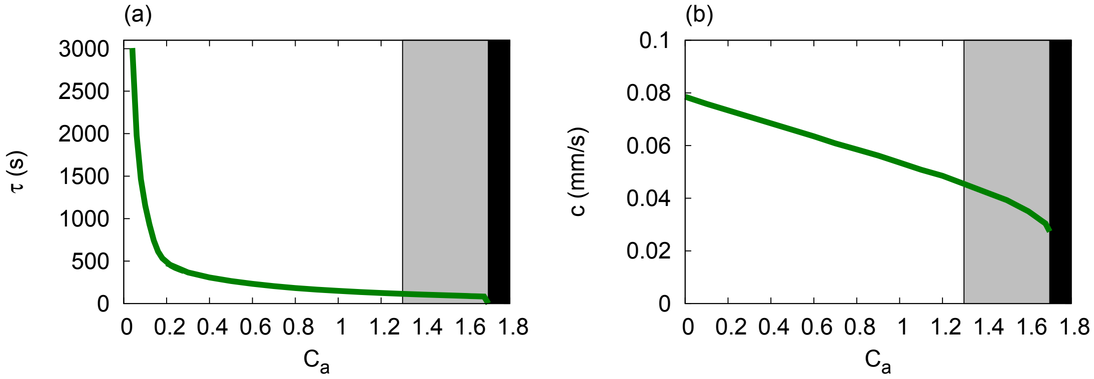

FIGURE 3.8: Duration of depolarization τ (a) and propagation velocity c (b) of propagating pulses computed with Eqs. (3.26),(3.27) and Eq. (3.29). The ACS is assumed to be a bath, $c_j^a = c_j^{a(0)}$, Eq. (3.32). (white area) Propagating pulses; (grey shaded area) excess ions from the ECS are buffered, but the depolarization persists, because in the NCS, the ion concentrations do not recover to physiological equilibrium values; (black area) no propagating solution. $\tau = t_2 - t_1$, with t_1 being the first time at a specific location x with $K_e > 20$ mmol/l, and t_2 being the first time $t_2 > t_1$ at the same location x with $K_e < 20$ mmol/l. $D_j = 2.0 \cdot 10^{-5}$ cm^2/s, $D_j^e = \frac{D_j}{\lambda_e^2}$.

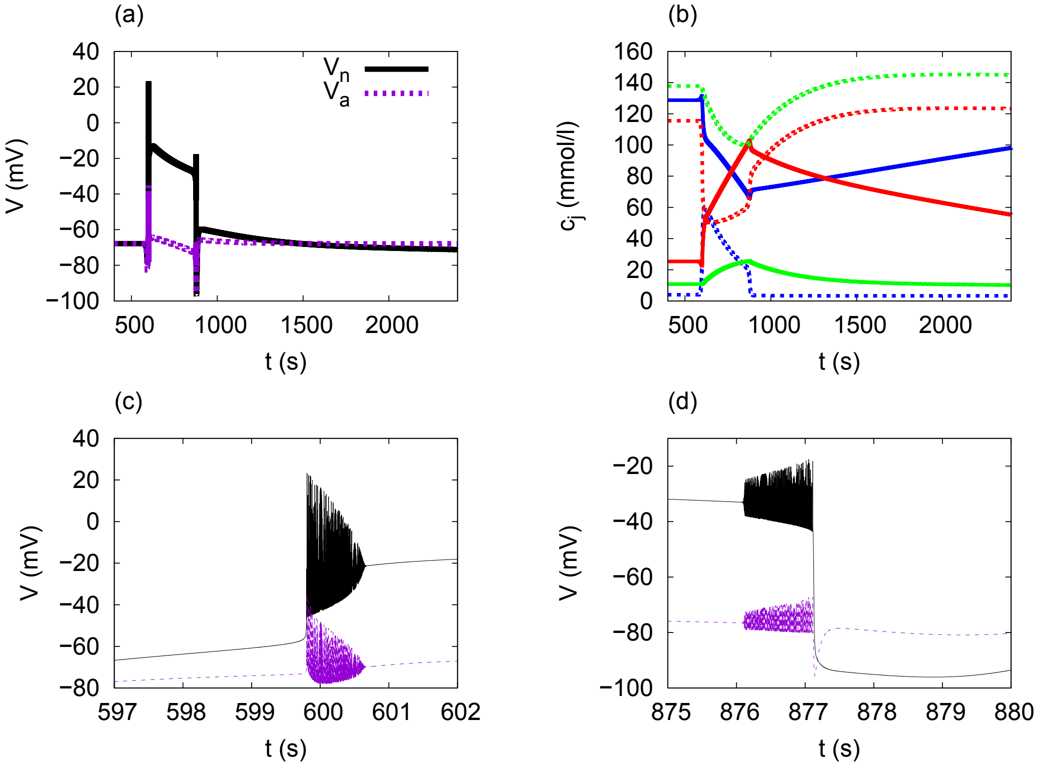

FIGURE 3.9: Temporal evolution of a propagating pulse solution calculated with Eqs. (3.26),(3.27) and (3.29). The ACS is assumed to be a bath, $c_j^a = c_j^{a(0)}$, Eq. (3.32). (a) Neuronal and glial membrane potential; (b) ion concentration of K (blue), Na (red) and Cl (green), each in the NCS (solid) and in the ECS (dashed); (c) neuronal and glial membrane potential at the rising front; (d) neuronal and glial membrane potential at the back; $D_j = 2.0 \cdot 10^{-5}$ cm^2/s, $D_j^e = \frac{D_j}{\lambda_e^2}$, $C_a = 0.5$.

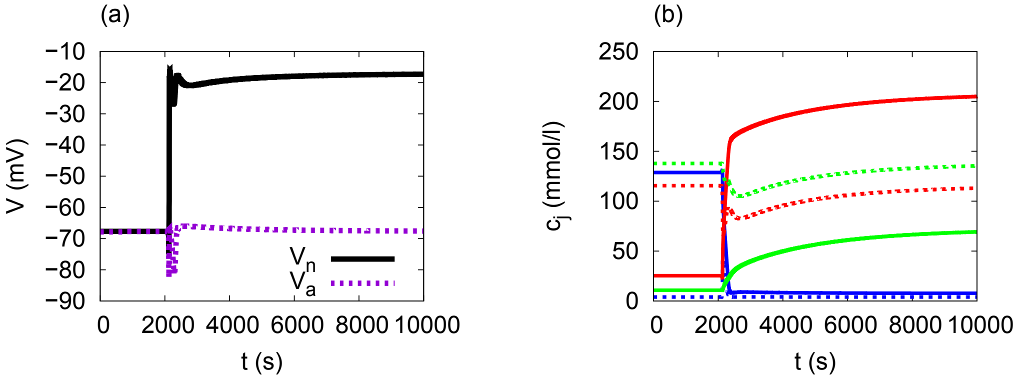

FIGURE 3.10: Temporal evolution of a propagating front solution calculated with Eqs. (3.26),(3.27) and Eq. (3.29). The ACS is assumed to be a bath, $c_j^a = c_j^{a(0)}$, Eq. (3.32). (a) Neuronal and glial membrane potential; (b) ion concentration of K (blue), Na (red) and Cl (green), each in the NCS (solid) and in the ECS (dashed). $D_j = 2.0 \cdot 10^{-5}$ cm^2/s, $D_j^e = \frac{D_j}{\lambda_e^2}$, $C_a = 1.5$.

If, however, C_a is to large, the very strong glial buffer does not succeed to recover the depolarized system to the polarized state (grey shaded area in Figs. 3.8(a),(b)). Because excess ions in the ECS are cleared very fast by the bath, they lack to restore the equilibrium in the NCS, see Fig. 3.10. For even larger values of C_a, no propagating solutions can be found (black area in Figs. 3.8(a),(b)).

3.2.4 Electroneutrality

In the three-compartmental reaction-diffusion model Sects. 3.2.1 and 3.2.2, the diffusive currents in both compartments, the ECS and the ACS, are electroneutral. Thus due to local charge conservation, the descriptions of the membrane potential Eq. (2.108), Eq. (2.111) and Eqs. (2.114)-(2.115) are equivalent.

However, if the ACS is assumed to be a bath Sect. 3.2.3, charge conservation can be violated and thus the choice of the membrane potential determines if electroneutrality holds. Thereby, the argumentation of Sect. 2.4.4 still holds. Throughout this section, we choose the description for the neuronal and glial membrane potential

$$V_m^{n,a} = \frac{1}{2C_m\gamma}(\rho_{n,a} - \rho_e). \tag{3.33}$$

3.3 Neuronal gap junctions

In recent years, neuronal gap junctions have been characterized to exist in several adult brain regions, including the neocortex, thalamus, inferior olive, cerebellum and retina. The role of neuronal gap junctions on CSD, however, is widely unknown.

In our model, the neuronal gap junctions are as the glial gap junctions, see Sect. 3.2.2, described by diffusing ions within the neuronal compartment. To figure out the effect of neuronal gap junctions on CSD, first, the bistable two-compartmental elements consisting of a NCS and an ECS, Sect. 2.1, are spatially coupled by diffusing ions in the ECS and in the NCS. The rate equations then read

$$\frac{\partial n}{\partial t} = \frac{n_\infty - n}{\tau_n}, \tag{3.34}$$

$$\frac{\partial c_j^n}{\partial t} = -z_j \frac{\gamma}{\omega_n} I_j^n + D_j^n \frac{\partial^2 c_j^n}{\partial x^2}, \tag{3.35}$$

$$\frac{\partial c_j^e}{\partial t} = z_j \frac{\gamma}{\omega_e} I_j^n + D_j^e \frac{\partial^2 c_j^e}{\partial x^2}, \tag{3.36}$$

with D_j^n being the effective diffusion coefficient of the respective ionic species in the NCS. As electroneutral diffusion also in the NCS is required, we set the diffusion coefficient of each ionic species equal, $D_{Na}^n = D_K^n = D_{Cl}^n$. The size of D_j^n is a measure for the permeability of the cellular structure. As the amount of neuronal gap junctions is very low, D_j^n is much smaller than D_j^e.

Our model suggests, that neuronal gap junctions have a strong inhibitory effect on CSD, Fig. 3.11. Already very small values of D_j^n massively decelerate propagating fronts. This is accompied by an enhancement of the initial bursting, see Figs. 3.11(b),(c),(d). If the diffusion strength in the NCS exceeds a critical value, no front propagation is possible.

Next, we analyze the three-compartmental model with diffusion in all compartments,

$$\frac{\partial n}{\partial t} = \frac{n_\infty - n}{\tau_n}, \tag{3.37}$$

$$\frac{\partial c_j^n}{\partial t} = -z_j \frac{\gamma}{\omega_n} I_j^n + D_j^n \frac{\partial^2 c_j^n}{\partial x^2}, \tag{3.38}$$

$$\frac{\partial c_j^a}{\partial t} = -z_j \frac{\gamma}{\omega_a} I_j^a + D_j^a \frac{\partial^2 c_j^a}{\partial x^2}, \tag{3.39}$$

$$\frac{\partial c_j^e}{\partial t} = z_j \frac{\gamma}{\omega_e} \left(I_j^n + I_j^a\right) + D_j^e \frac{\partial^2 c_j^e}{\partial x^2}. \tag{3.40}$$

The diffusion strength in the ACS thereby is chosen to be $D_j^a = \frac{D_j}{\lambda_a^2}$ with $\lambda_a = 2 \cdot \lambda_e$.

Depending on the diffusion strength in the NCS D_j^n, the inhomogeneous solutions of the system change. For small values of D_j^n, we find stable propagating pulses, white area in Fig. 3.12. An example of the temporal evolution of such a pulse solution is shown in Fig. 3.13(a),(b),(c). You see the potential at the neuronal and glial membrane, Fig. 3.13(a), and the concentrations of each ionic species in the NCS, the ECS, Fig. 3.13(b), and the ACS, Fig. 3.13(c). For larger values of D_j^n, the propagation velocity c of the back of a depolarization is faster than the propagation velocity c of the front of a

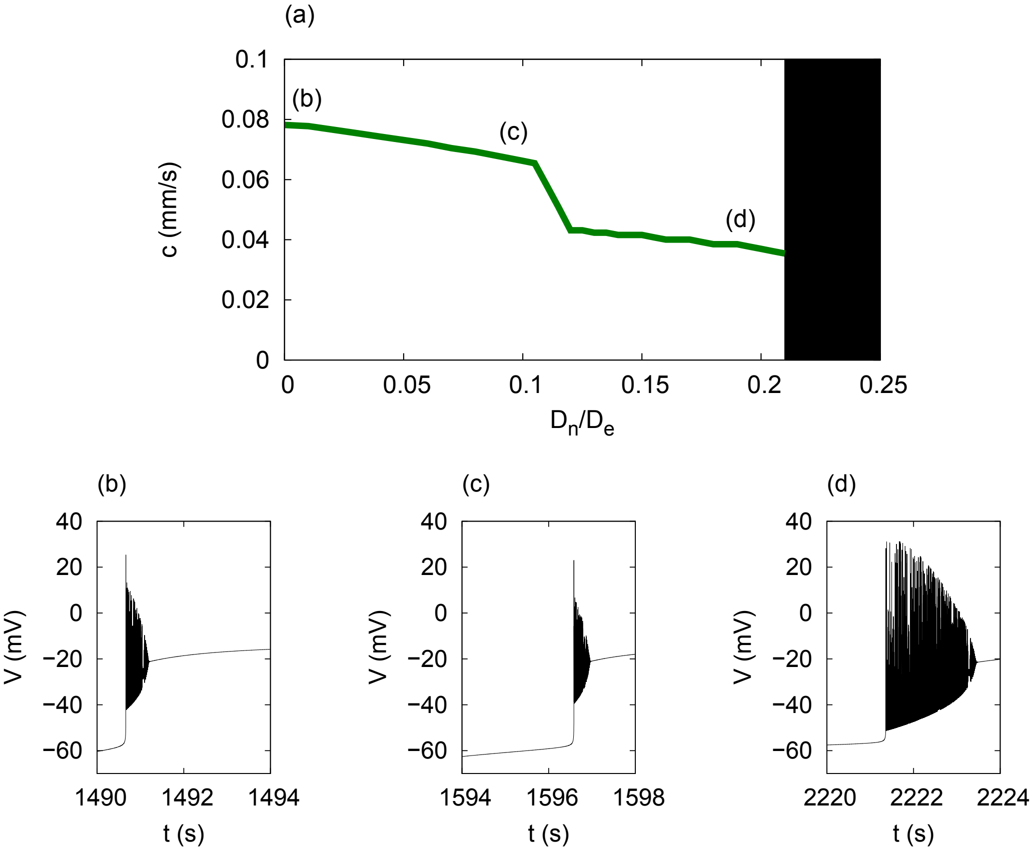

FIGURE 3.11: (a) Propagation velocity c of propagating front solutions computed with bistable two-compartmental elements spatially coupled by diffusion in the ECS and in the NCS, Eqs. (3.34)-(3.36), as a function of D_j^n/D_j^e, with constant D_j^e. In the black area, no propagation is possible. In addition, the temporal evolution of propagating front solutions at the rising front with $D_j^n = 0$ (b), $D_j^n = 0.1 \cdot D_j^e$ (c) and $D_j^n = 0.2 \cdot D_j^e$ (d) is shown. $D_j = 2.0 \cdot 10^{-5}$ cm^2/s, $D_j^e = \frac{D_j}{\lambda_e^2}$.

depolarization, light grey area in Fig. 3.12. In this parameter regime, propagating depolarizations decrease in width and disappear. For even larger values of D_j^n, the stationary propagating solution are hyperpolarizations, grey area in Fig. 3.12. An example of the profile of a propagating hyperpolarization is shown in Fig. 3.13(d),(e),(f). In the black area in Fig. 3.12, no propagating solution is found. Concluding, our model suggests that diffusion in the NCS has a strong inhibitory effect on CSD. For $D_j^n > 0.07 \cdot D_j^e$, no stable propagating pulse solution exists. For $D_j^n > 0.13 \cdot D_j^e$, we find no stable stationary propagating solution.

Modeling the glial cells as a bath,

$$c_j^a = c_j^{a(0)}, \tag{3.41}$$

the width τ and the propagation velocity c of the pulse solutions only slightly depend on the strength of the diffusion in the NCS, see Fig. 3.14. However, the inhibitory effect of

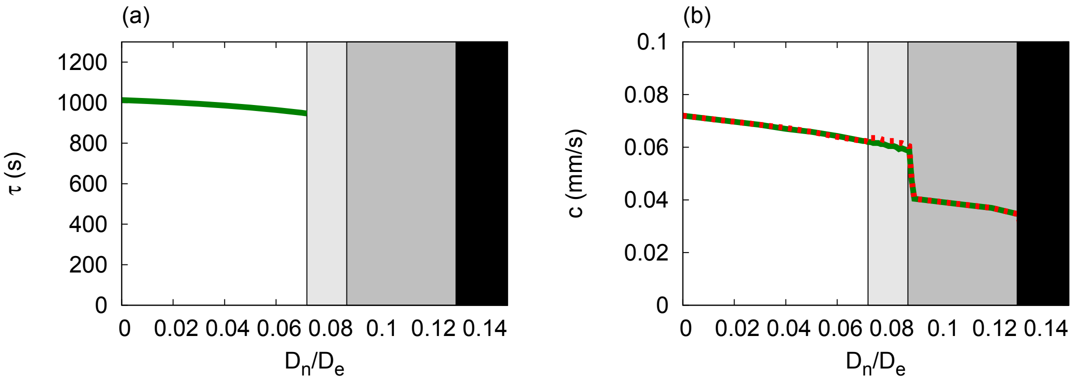

FIGURE 3.12: Duration τ (a) and propagation velocity c of pulse front (green, solid) and pulse back (red, dashed) (b) of propagating pulses computed with three-compartmental elements spatially coupled by diffusion in all compartments, Eqs. (3.37)-(3.40), as a function of D_j^n/D_j^e, with constant D_j^e. $\tau = t_2 - t_1$, with t_1 being the first time at a specific location x with $K_e > 20$ mmol/l, and t_2 being the first time $t_2 > t_1$ at the same location x with $K_e < 20$ mmol/l. $D_j = 2.0 \cdot 10^{-5}$ cm^2/s, $D_j^e = \frac{D_j}{\lambda_e^2}$, $D_j^a = \frac{D_j}{\lambda_a^2}$. (white area) Stable propagating pulse solutions; (light grey area) pulse back is faster than pulse front, pulses decrease in breath and disappear; (grey area) stable propagating hyperpolarizations.

neuronal gap junctions remains. If D_j^n exceeds a small critical value, no stable stationary propagating solution is found.

3.4 Conclusion

In this chapter, we designed a biophysically detailed reaction-diffusion model. In detail, we coupled local ion-based neuronal elements by ion diffusion in the extracellular space and by ion diffusion through neuronal and glial gap junctions in a 1D geometry.

Addressing the problem of electroneutral diffusion, we showed that the so-called electroneutral electrodiffusive description proposed in [30] here can be approximated by setting the diffusion coefficients of all ionic species within one compartment equal.

Then, we analyzed, which mechanisms are relevant for ionic homeostasis. In detail, we investigated, how existence and type of inhomogenious solutions depends on the particular lateral currents. First, we coupled bistable two-compartmental elements consisting of a neuron surrounded by an extracellular space by diffusion in the extrcellular space. We found that the system has propagating front solutions, i.e., solutions that connect the two stable states and propagate over space. Thus, lateral diffusion in the extracellular space is not sufficient for ionic homeostasis, an area once depolarized does not recover to the polarized equilibrium. This behaviour is found during anoxic depolarization. During CSD, however, the depolarized state is not stable.

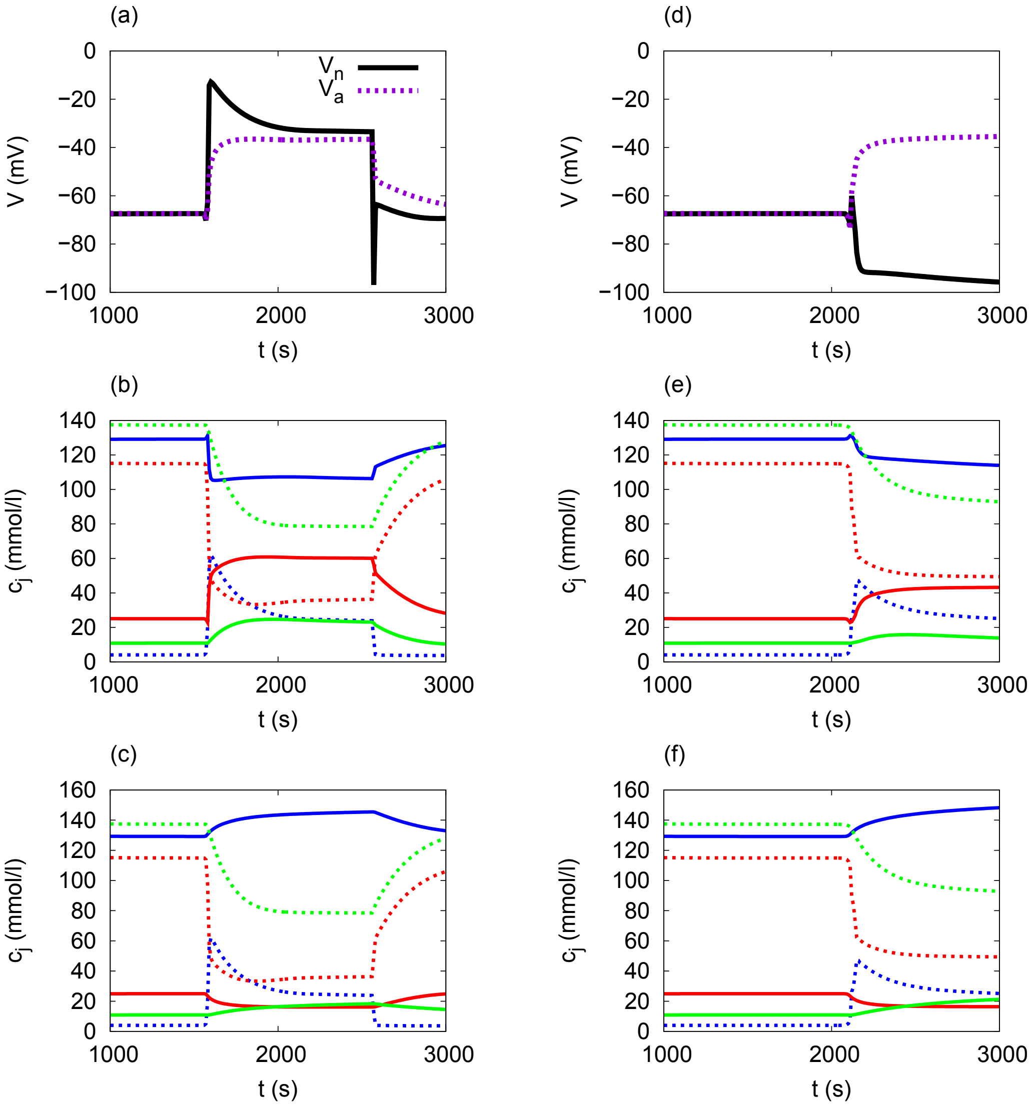

FIGURE 3.13: Temporal evolution of a propagating pulse solution with $D_j^n/D_j^e = 0.04$ (a),(b),(c) and of a propagating hyperpolarization with $D_j^n/D_j^e = 0.1$ (d),(e),(f) computed with three-compartmental elements spatially coupled by diffusion in all compartments, Eqs. (3.37)-(3.40). (a),(d) Neuronal and glial membrane potential; (b),(e) ion concentration of K (blue), Na (red) and Cl (green), each in the NCS (solid) and in the ECS (dashed); (c),(f) ion concentration of K (blue), Na (red) and Cl (green), each in the ACS (solid) and in the ECS (dashed). $D_j = 2.0 \cdot 10^{-5}$ cm^2/s, $D_j^e = \frac{D_j}{\lambda_e^2}$, $D_j^a = \frac{D_j}{\lambda_a^2}$.

Next, the role of lateral diffusion was analyzed in the three-compartmental system. First, only diffusion in the extracellular space was considered, neuronal and glial gap junctions were neglected. The inhomogeneous solutions we found confirm that lateral diffusion in the extracellular space does not contribute to relaxation. In detail, in the parameter regime, in which the local elements are bistable (small astrocytic compartment, Sect. 2.4.2) and the glial buffer fails, the spatially extended system has propagating front solutions. In the parameter regime, in which the bistable elements after and excitation recover due to a large amount of ion channels at the glial membrane, the

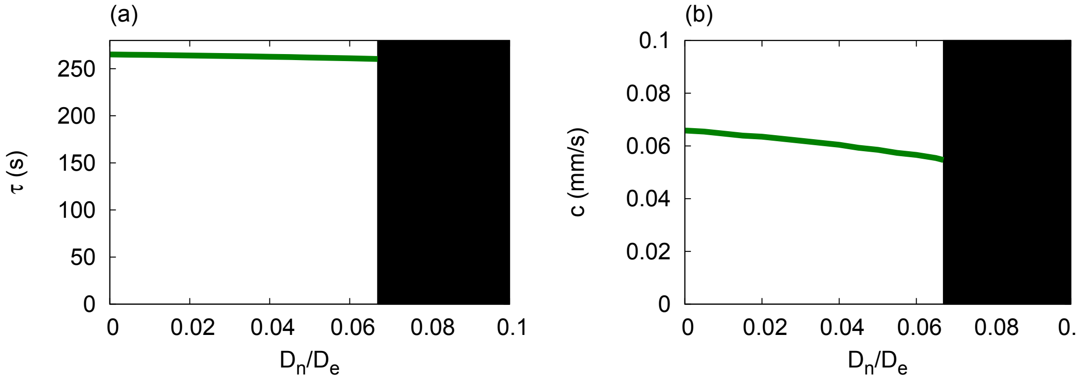

FIGURE 3.14: Duration of depolarization τ (a) and propagation velocity c (b) of propagating pulses computed with Eqs. (3.37),(3.38) and Eq. (3.40), the ACS is assumed to be a bath, $c_j^a = c_j^{a(0)}$, Eq. (3.32), as a function of D_j^n/D_j^e, with constant D_j^e. $\tau = t_2 - t_1$, with t_1 being the first time at a specific location x with $K_e > 20$ mmol/l, and t_2 being the first time $t_2 > t_1$ at the same location x with $K_e > 20$ mmol/l. $D_j = 2.0 \cdot 10^{-5}$ cm^2/s, $D_j^e = \frac{D_j}{\lambda_e^2}$. (black area) No propagating solution is found.

reaction-diffusion model has coexisting front and pulse solutions. If the local elements are monostable (large astrocytic compartment), only pulse solutions exist.

Adding glial gap junctions, i.e., allowing for diffusion within the glial compartment, we found that the width of propagating pulses decreases with increasing diffusion strength in the glial compartment. Thus, our model suggests that glial gap junctions facilitate relaxation. However, in the whole analyzed parameter regime pulse solutions exist, the glial gap junctions hence do not prevent CSD.

A medium consisting of monostable two-compartmental elements, i.e., single neurons surrounded by an open extracellular space connected to a glial bath spatially coupled by extracellular diffusing ions, has propagating pulse solutions. As the glial bath due to infinite capacity buffers very strong, the pulse width is small. The assumption of a glial bath can be interpreted as making the approximation that excess ions in the astrocyte are cleared by the vasculature instantaneously. The model suggests that this shortens the period of CSD, but does not avoid it.

Furthermore, the role of neuronal gap junctions on propagating solutions was discussed. As between neurons only few gap junctions exist, small diffusion coefficients D_j^n are assumed. Our model suggests that neuronal gap junctions have a strong inhibitory effect on propagating solutions. Propagating front solutions computed with the bistable two-compartmental model decelerate massively already at small values of D_j^n. Pulse solutions modeled with the three-compartmental model become transient. If the diffusion coefficient D_j^n is slightly increased, in all analyzed model compositions, no stationary propagating solution was found.

Chapter 4

A generic neuronal model

We want to analyze the influence of external forces such as the geometry of the brain or an externally applied electrical field on CSD. To describe CSD with a mathematically tractable model of activator-inhibitor type, we use FHN dynamics.

The FHN model originally is a two-variable simplification of the four-variable HH model, which describes the conduction of voltage pulses along the membrane of nerve cell axons [10]. In this context, the FHN model describes the response of an excitable nerve membrane to external current stimulation. Although the approximate equations lose some of the physical meaning of the more complete biophysical model, they allow for analytical manipulations and therefore provide more insight into the mathematical processes involved.

In this chapter, the FHN equations are introduced, Sect. (4.1). Then, in Sect. (4.2), we discuss whether the FHN model is a reasonable simplification of the ion-based neuron model for CSD proposed in Chapt. 2.

4.1 FitzHugh-Nagumo equations

Cortical tissue has been shown to be weakly excitable for pulse propagation [75–77]. As an excitable medium, it can be described by reaction-diffusion models. A simple one-variable reaction-diffusion model is the Schlögl model, whose kinetics are given by a cubic reaction part,

$$\frac{\partial u}{\partial t} = 3u - u^3 - v_0 + D\nabla^2 u, \tag{4.1}$$

$$\tag{4.2}$$

whith the variable $u(\vec{x},t)$ and the diffusion coefficient D. ∇^2 is the Laplace operator $\sum_{i=1}^{n} \frac{\partial^2}{\partial x_i^2}$ in a n-dimensional medium. The Schlögl model is bistable, it has two spatially homogeneous solutions separated by an unstable one. In addition, the system has a stationary propagating solution, that connects the two stable states. The parameter v_0 determines whether the stationary propagating solution is a front or a back solution. For $v_0 = 0$, the propagation velocity of the stationary propagating solution is zero.

For the mathematical description of pulses, stationary propagating solutions that start and end in the same stable state, at least two dynamical variables are needed. FitzHugh and Nagumo proposed to use a second slow inhibiting variable with linear dynamics [4, 5]. This simple mathematical description covers the requirement of changing homogeneous system dynamics from bistable to excitable,

$$\frac{\partial u}{\partial t} = 3u - u^3 - v + D\nabla^2 u, \tag{4.3}$$

$$\frac{\partial v}{\partial t} = \varepsilon(u + \beta - \gamma v). \tag{4.4}$$

The original interpretation of the FHN model Eqs. (4.3), (4.4) is based on a single neuron. The variable u models fast changes of the electrical potential across the membrane of a nerve cell axon (occurring as spikes in the time series), and v is the recovery variable related to the gating mechanism of the membrane channels [4]. The small parameter $\varepsilon \ll 1$ represents the time scale ratio of the two variables. The fast variable u is called the activator variable, whereas the slow variable v is referred to as inhibitor variable. The diffusion constant of the activator is D, which can simply be interpreted as a scaling of space, and inhibitor diffusion is assumed to be slow and hence negligible. In the following, the parameter γ is set at zero. The excitability parameter β determines whether the systems is excitable ($\beta > 1$) or exhibits self-sustained perodic oscillations ($\beta < 1$). In the following, we consider β in the excitable regime.

Fig. 4.1 shows a schematic phase portrait of a spatially homogeneous system in the excitable regime ($\beta > 1$) with the cubic activator nullcline (solid red line) and the vertical inhibitor nullcline (solid green line). The system has a single fixed point (u_s, v_s), which is stable for $\beta > 1$ and located on the left branch of the cubic nullcline. At $\beta = 1$, a limit cycle occurs in a supercritical Hopf bifurcation, the fixed point becomes unstable and is shifted to the middle branch of the nullcline for $\beta < 1$.

The excitable behaviour of the system is crucially determined by the cubic nonlinearity of the activator equation and the separation of time-scales between the two variables. When the system is perturbed by a sufficiently large (super-threshold) external stimulus, which can be regarded as setting the initial conditions, the system undergoes a large excursion in phase space (spiking). Starting from its initial condition, the system performs, due

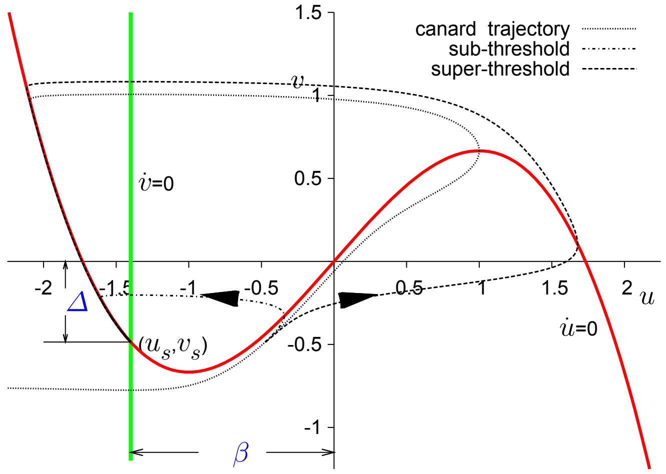

FIGURE 4.1: The nullclines $\dot{u} = 0$ (solid red) and $\dot{v} = 0$ (solid green) in the phase space of the homogeneous FHN system with $\beta = 1.4$. Their intersection at (u_s, v_s) is a stable fixed point. Three trajectories are drawn for $\varepsilon = 0.04$: one canard-like trajectory (dotted) passing through the maximum of the nullcline $\dot{u} = 0$, and two trajectories starting at $v = v_s$ nearby but on opposite sides of the canard trajectory. They diverge sharply, producing threshold-like behaviour: the dashed and the dash-dotted trajectories represent super-threshold and sub-threshold stimulation, respectively.

to the strong timescale separation $\varepsilon \ll 1$, a fast transition to the stable right branch of the activator nullcline. After that, it travels slowly upwards approximately along this nullcline, until the phase point jumps back to the left branch, and returns, along the left branch of the nullcline, slowly downwards to the fixed point (recovery phase). Without further external stimulation, the system remains in the stable fixed point (rest state).

The threshold-like behaviour of the FHN system is associated with the *canard-like trajectory* (dotted black line in Fig. 4.1), which is the trajectory passing through the local maximum of the cubic nullcline, and which is often referred to as the threshold of the FHN system. The region around the canard-like trajectory is extremely sensitive to initial conditions. For initial conditions only slightly below the canard-like trajectory, the systems will perform a large excursion in phase space, whereas for initial conditions only slightly above the canard-like trajectory, the excursion will be small. In principle, the transition from small to large amplitude excitation is continuous; in fact, however, phase space excursions of intermediate amplitude are very rare. Correspondingly, small sub-threshold stimulations (dash-dotted black line in Fig. 4.1) will result in fast relaxation, while super-threshold stimulations (dashed black line in Fig. 4.1) induce a full excursion in phase space, corresponding to a characteristic spike in the time evolution of the u-variable.

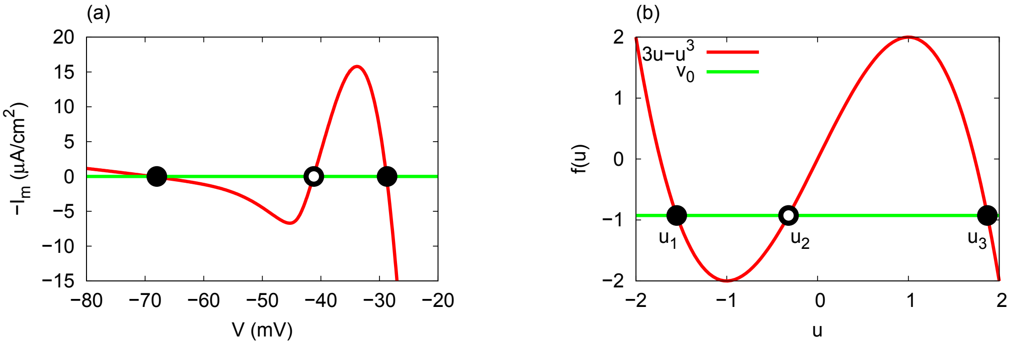

FIGURE 4.2: (a) Projection of the phase space of the voltage-clamped two-compartmental biophysical model Eqs. (2.42)-(2.47) on the V_m^n-space. At time T, a step voltage is applied. The negative sum over the transmembrane currents $-\sum_j I_j^n(t=T)$, which is proportional to $\frac{\partial V_m^n}{\partial t}$, is shown as a function of V_m^n. (b) Phase space of the homogeneous Schlögl model Eq. (4.1). You see the cubic reaction part $3u - u^3$ as a function of u (red) and the variable v_0 (green). Both systems (a) and (b) have two stable fixed points (black dots), and in between one unstable fixed point (hollow dot).

4.2 Comparing the FitzHugh-Nagumo model and the biophysically detailed model

As described by Casten, Cohen and Lagerstrom [78], the approximations made to reduce the HH model to the FHN model are based on a separation of timescales. In HH model, the voltage changes and the turning on of the sodium inflow are much faster than the recovery process that is due to turning on the potassium outflow and to turning off the sodium inflow. In FHN model, the activator variable is related to the fast changes of the electrical membrane potential, and the inhibitor variable is related to the slow gating mechanisms of the HH model.

Here, we discuss whether the FHN system is a reasonable approximation of the ion-based model for CSD proposed in Chapt. 2. The local two-compartmental ion-based model consisting of a NCS and a closed ECS is bistable, it has, besides the physiological state, a second stable state. This can be seen in Fig. 4.2(a), where the fast current response to a voltage step in the voltage-clamped system is shown, compare Sect. 2.4.2. Also the Schlögl model Fig. 4.2(b) has two homogeneous stable states. Spatially coupled by diffusion, in both systems, the ion-based biophysical model and the Schlögl model, fronts that connect the two stable states are the single stationary propagating solution.

However, Fig. 4.2(a) is a projection of the 4-dimensional phasespace of the ion-based system on the V_m-space, whereas the phasespace of the homogeneous Schlögl model only has one dimension. After a super-threshold excitation, the trajectory of the ion-based model exhibits extreme oscillations, Fig. 4.3, that correspond to the bursting at

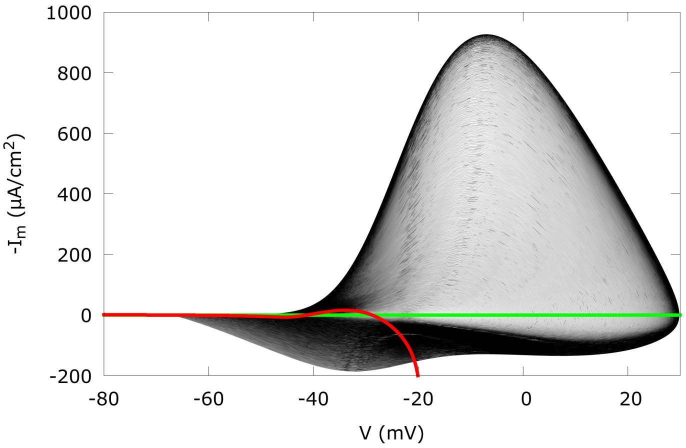

FIGURE 4.3: (black) Trajectory of a bursting rising front calculated with the two-compartmental ion-based model Eqs. (2.42)-(2.47) in the V_m-space. (red) Voltage-clamped curve, compare Fig. 4.2(a).

the rising front, before it arrives in the depolarized state. The Schlögl model doesn't capture this behaviour.

To change homogeneous dynamics from bistable to excitable, a buffer mechanism is needed in both systems, the Schlögl model and the ion-based model. In the FHN model, the activator u, whose dynamics are described by a rate equation identical to the Schlögl model, is buffered by a second dynamical variable, the slow inhibitor v Eq. (4.4). A simplified buffer mechanism for the ion-based model that has a similar structure as the inhibitor mechanism of the FHN model was proposed in [79]. If the extracellular potassium concentration deviates from a specific value, it is buffered by a bath with a linear dependency. Then, in the local two-compartmental system Eqs. (2.42)-(2.47), the potassium concentration in the ECS is calculated with

$$\frac{\partial K_e}{\partial t} \quad = \quad \frac{\gamma}{\omega_e}\left(I_K - 2I_P\right) - D\left(K_e - K_{bath}\right). \tag{4.5}$$

The buffer strength D is in the unit $1/s$. This buffer scheme can be translated in the inhibitor mechanism of the FHN model if we use the description for the neuronal membrane potential Eq. (2.63) $V_m^n = \frac{1}{2C_m\gamma}\left(\rho_n - \rho_e\right)$. The derivation of the membrane potential V_m^n with respect to time then reads

$$\frac{\partial V_m^n}{\partial t} = \frac{\omega_n}{2C_m\gamma}\left(\frac{\partial Na_n}{\partial t} + \frac{\partial K_n}{\partial t} - \frac{\partial Cl_n}{\partial t}\right) - \frac{\omega_e}{2C_m\gamma}\left(\frac{\partial Na_e}{\partial t} + \frac{\partial K_e}{\partial t} - \frac{\partial Cl_e}{\partial t}\right). \tag{4.6}$$

With Eq. (4.5), we obtain

$$\frac{\partial V_m^n}{\partial t} = -\frac{1}{C_m}\left(\sum_j I_j^n - \frac{1}{2}\frac{\omega_e}{\gamma} D\left(K_e - K_{bath}\right)\right). \tag{4.7}$$

As the FHN system, this system has an activator V_m^n Eq. (4.7), which at the rising front is increased by the fast sodium currents and inhibited by K_e. For small buffer strength D, dynamics of the inhibitor K_e occur on a much slower timescale. The potassium concentration of the bath K_{bath} determines the size of the threshold.

Excitability can be categorized in systems of type I or type II [80]. These differ in the transition to the oscillating regime: systems of type I start oscillating in a SNIPER bifurcation, systems of type II in a Hopf bifurcation. The excitable regime lies below the SNIPER and the Hopf bifurcation, respectively. As shown in [79], the ion-based model, with a buffer scheme according to Eq. (4.5), is monostable for values of K_{bath} around 4mmol/l, which is the physiological potassium concentration in the extracellular space. If K_{Bath} is increased, the fixed point changes from stable to unstable in a supercritical Hopf bifurcation (for $\frac{\omega_e}{\gamma} D = 10^{-5}$ μm A/mmol at $K_{bath} \approx 7$ mmol/l). Thus, the excitability of the system is of type II. This is analogous to the FHN model, where the transition from excitable to oscillating also occurs in a supercritical Hopf bifurcation, when the threshold parameter β is varied.

Throughout this thesis, another description for the buffer mechanism in the ion-based model was used, namely excess ions from the ECS are buffered into a third compartment, the ACS, see Sect. 2.4.1. This buffer also causes monostability if the volume fraction of the ACS isn't too small, see Fig. 2.7. However, this detailed buffer description cannot be translated in terms of the generic inhibitor equation of the FHN model, and we didn't investigate this scheme in a bifurcation analysis.

4.3 Inhomogeneous solutions in the FitzHugh-Nagumo model

In the following, we consider spatially inhomogeneous solutions, i.e., waves or wave segments in one (Chapt. 5) or two (Chapt. 6) spatial dimensions. As we are interested in stationary propagating solutions, i.e., waves that propagate with constant velocity c

and constant shape, Eqs. (4.3),(4.4) can be written as

$$c\frac{\partial u}{\partial \xi} = 3u - u^3 - v + D\nabla_\xi^2 u, \tag{4.8}$$

$$c\frac{\partial v}{\partial \xi} = \varepsilon(u + \beta), \tag{4.9}$$

with $\xi = x + ct$ being the co-moving coordinate. Thereby, without loss of generality, we only consider waves propagating in negative x-direction.

Chapter 5

Critical properties of reaction-diffusion waves in one spatial dimension

In this Chapter, we investigate the effect of advection on the propagation and, in particular, on the critical minimal speed of traveling waves. To this end, we introduce FHN model in one spatial dimension with additional differential advection, Sect. 5.1.

Several properties of waves propagating in a spatial 2D medium are captured by an effective 1D description. E.g., a wave infinitely extended orthogonal to its propagation direction can be described in 1D, and, in addition, an effective 1D description is useful to calculate properties of curved 2D wave segments.

In the excitable regime, i.e., $\beta > 1$ and ε and β below a critical value, the system has, besides the homogeneous steady state, two spatially inhomogeneous solutions, an unstable slow traveling wave and a stable fast traveling wave, that propagate with constant velocity c and constant wave profile $u(x,t)$, $v(x,t)$, see Fig. 5.1. Affected by differential advection, the propagation velocities of the fast and slow traveling wave converge and annihiliate at a critical value.

To derive an analytical approximation for this critical velocity and the corresponding critical advection strength, Sect. 5.4, we first define the propagation boundary, Sect. 5.2, and then we calculate the advection-velocity relation for the unstable slow wave, Sect. 5.3. We also analyze the two-variable reaction-diffusion-advection model numerically in a wide parameter range and compare theoretical predictions to numerical results, Sect. 5.5.

Parts of this chapter are published in [81].

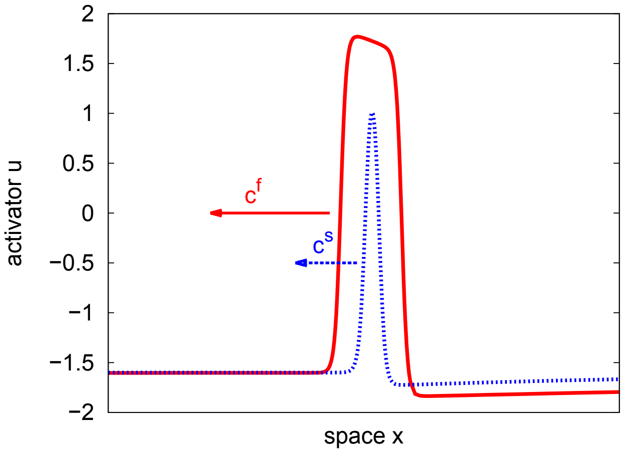

FIGURE 5.1: Snapshots of the profile of activator u as a function of space x of a stable fast wave (solid red line) and an unstable slow wave (dotted blue line) propagating to negative x-direction numerically computed from Eqs. (5.1),(5.2). $\varepsilon = 0.022$, $\beta = 1.6$.

5.1 Differential Advection

In one spatial dimension, Eqs. (4.3),(4.4) reduce to

$$\frac{\partial u}{\partial t} = 3u - u^3 - v + D\frac{\partial^2 u}{\partial x^2}, \tag{5.1}$$

$$\frac{\partial v}{\partial t} = \varepsilon(u + \beta), \tag{5.2}$$

with $D \neq 0$. Traveling waves are stationary solutions in the co-moving system, which in one spatial dimension reads

$$c\frac{\partial u}{\partial \xi} = 3u - u^3 - v + D\frac{\partial^2 u}{\partial \xi^2}, \tag{5.3}$$

$$c\frac{\partial v}{\partial \xi} = \varepsilon(u + \beta), \tag{5.4}$$

with $\xi = x + ct$.

An advection term added to Eq. (5.1) or Eq. (5.3) may arise through different mechanisms.

First, an advection term in an 1D medium is an approximation of curved reaction diffusion waves in spatially 2D media [51]. Propagating curved wave segments with $L \ll R$, where L is the width of the wave segment and R is the curvature radius of the front, can be locally approximated by

$$c(A)\frac{\partial u}{\partial \xi} = 3u - u^3 - v + D\frac{\partial^2 u}{\partial \xi^2} + A\frac{\partial u}{\partial \xi}, \tag{5.5}$$

$$c(A)\frac{\partial v}{\partial \xi} = \varepsilon(u + \beta), \tag{5.6}$$

with $A = \frac{D}{R}$, see Appendix. This effective 1D description is useful to calculate properties of curved 2D wave segments, e.g., the dependency of the propagation velocity on the curvature or the maximal possible curvature of a wave front. Examples of stable curved reaction diffusion waves are target pattern, spiral waves [82] or ring-shaped autowaves, that propagate on a torus and thus exhibit positive and negative Gaussian curvature [83, 84]. It has been shown that the ring-shaped autowaves break up, when the negative Gaussian curvature exceeds a critical value.

Second, the same set of equations, i.e., Eqs. (5.5),(5.6), can be obtained if advection due to a constant external driving force is considered. Both, activator u and inhibitor v can be associated with particles of different mobilities μ_u and μ_v. Particle motion can then be affected by a homogeneous external field, which is applied parallel to the propagation direction, e.g., ions or charged macromolecules are influenced by an homogeneous external electric field of strength E. This has been experimentally studied in the chemical BZ reaction with spiral waves [85], and Turing patterns influenced by external electrical fields have been studied in the chlorine dioxide-iodine-malonic acid reaction [86]. Then, Eqs. (5.3),(5.4) read

$$c\frac{\partial u}{\partial \xi} = 3u - u^3 - v + D\frac{\partial^2 u}{\partial \xi^2} + \mu_u F\frac{\partial u}{\partial \xi}, \tag{5.7}$$

$$c\frac{\partial v}{\partial \xi} = \varepsilon(u + \beta) + \mu_v F\frac{\partial v}{\partial \xi}, \tag{5.8}$$

where F is the strength of the field and $zE = -F$ with the valence z of the ion. Thereby, it is assumed that the force on the inhibitor v due to the electrical gradient is much stronger than the force due to the chemical gradient (inhibitor diffusion).

In [52] it is proposed to change the velocity of the co-moving frame to $\tilde{c} = c - \mu_v F$. For $\tilde{c} = c(A)$, this yields

$$c(A)\frac{\partial u}{\partial \xi} = 3u - u^3 - v + D\frac{\partial^2 u}{\partial \xi^2} + A\frac{\partial u}{\partial \xi}, \tag{5.9}$$

$$c(A)\frac{\partial v}{\partial \xi} = \varepsilon(u + \beta), \tag{5.10}$$

where $\xi = x - (c - \mu_v F)t$ and $A = F(\mu_u - \mu_v)$. Now, Eqs. (5.9),(5.10) and Eqs. (5.5),(5.6) are equal. In stationary coordinates, this reads

$$\frac{\partial u}{\partial t} = 3u - u^3 - v + D\frac{\partial^2 u}{\partial x^2} + A\frac{\partial u}{\partial x}, \tag{5.11}$$

$$\frac{\partial v}{\partial t} = \varepsilon(u + \beta). \tag{5.12}$$

Varying D accords to scaling x and A. In the remainder, D is set to unity.

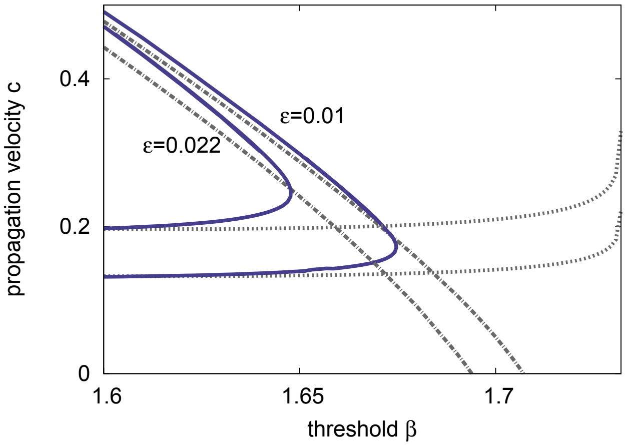

FIGURE 5.2: Propagation velocity c as a function of threshold β. The blue solid line shows the results from Eqs. (5.1),(5.2) computed with *AUTO* [69] by continuation of homoclinic solutions. The fast wave branch and the slow wave branch coalesce at a critical velocity ($c_{cr}|_{A=0}$). The grey dash-dotted lines show the fast wave velocity calculated with Eq. (5.17). The grey dashed lines show the slow wave velocity calculated with Eq. (5.18).

Let us briefly remark that in the excitable parameter regime, Eqs. (5.11),(5.12) have four wave solutions (two stable fast and two unstable slow ones) propagating in opposite direction. In the following, we only consider the two waves propagating in negative x-direction. This can be done without loosing information, as the two waves propagating in positive x-direction influenced by advection of strength A show the same behaviour as the two waves propagating in negative x-direction influenced by advection of strength $-A$.

5.2 Propagation boundary

FHN system without advection in the excitable parameter regime, Eqs. (5.1),(5.2) with $1 < \beta < \sqrt{3}$ and ε sufficiently small, has a stable fast wave solution and an unstable slow wave solution, Fig. 5.1, which correspond to homoclinic orbits of the related ODE problem Eqs. (5.3),(5.4), see [87]. There exists a critical line ∂P in the (ε, β) space, at which the fast wave branch coalesces with the slow wave branch, see Fig. 5.2. For values of β and ε above this critical line, propagation of traveling waves cannot be obtained. These properties carry over to the case of finite advection of strength A. Thus, it is reasonable to take into account the slow wave solution when calculating the critical properties, i.e., the critical surface in the (ε, β, A) space, which separates the excitable and the non-excitable parameter regime, and a critical velocity c_{cr} depending on advection of strength A.

5.3 Advection-velocity relation of the fast and slow wave solution

The advection-velocity relation of the slow wave can be derived in the same way as the known advection-velocity relation of the fast wave (nonlinear Eikonal equation [51]). Introducing c^* and ε^*

$$c^* = c(A) - A, \tag{5.13}$$

$$\varepsilon^* = \varepsilon \frac{c^*}{c(A)} \tag{5.14}$$

in Eqs. (5.9),(5.10) yields

$$c^* \frac{\partial u}{\partial \xi} = 3u - u^3 - v + D \frac{\partial^2 u}{\partial \xi^2}, \tag{5.15}$$

$$c^* \frac{\partial v}{\partial \xi} = \varepsilon^* (u + \beta), \tag{5.16}$$

which has the same form as the FHN model without advection Eqs. (5.3),(5.4). Thus, c^* has the same dependency on ε^* and β as the propagation velocity $c|_{A=0}$ (see Eqs. (5.3)-(5.4)) on ε and β. The velocity $c|_{A=0}$ for the fast and the slow wave can then be calculated approximately using a singular perturbation theory [78]. The propagation velocity of the fast $c^f|_{A=0}$ and the slow $c^s|_{A=0}$ wave is then obtained by

$$c^f|_{A=0} = c_0 + \varepsilon c_1^f, \tag{5.17}$$

$$c^s|_{A=0} = \sqrt{\varepsilon} c_1^s, \tag{5.18}$$

see Fig. 5.2. The expressions for c_0, c_1^f and c_1^s and their deviations are provided in the Appendix.

For c^* (see Eqs. (5.15),(5.16)), we therefore obtain the expressions

$$c^{f*} = c_0 + \varepsilon^* c_1^f, \tag{5.19}$$

$$c^{s*} = \sqrt{\varepsilon^*} c_1^s. \tag{5.20}$$

Inserting c^* and ε^* Eqs.(5.13),(5.14) and solving Eq. (5.19) for $c^f(A)$, we obtain the so-called nonlinear Eikonal equation

$$c^f_{\pm}(A) = \frac{1}{2}((A + c_0 + \varepsilon c_1) \pm \sqrt{(A + c_0 + \varepsilon c_1)^2 - 4\varepsilon A c_1}), \tag{5.21}$$

where $c^f_+(A)$ is the valid advection-velocity relation, see [51].

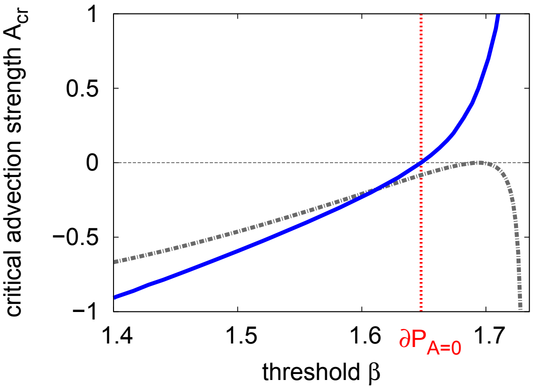

FIGURE 5.3: Critical advection strength A_{cr} as a function of threshold size β. The grey dashed line shows the results from Eq. (9), which was derived from the nonlinear Eikonal equation. The blue solid line shows the results computed from Eqs. (5.11),(5.12); the propagation boundary $\partial P_{A=0}$ is computed from Eqs. (5.1),(5.2). $\varepsilon = 0.022$ in each case. The blue solid line separates the excitable from the non-excitable parameter regime.

To get the advection-velocity relation of the slow wave, we solve Eq. (5.20) for $c^s(A)$. The three solutions are

$$\begin{aligned} c_+^s(A) &= \frac{1}{2}(A + \sqrt{A^2 + 4\varepsilon c_1^{s2}}), &(5.22)\\ c_-^s(A) &= \frac{1}{2}(A - \sqrt{A^2 + 4\varepsilon c_1^{s2}}), &(5.23)\\ c_3^s(A) &= A. &(5.24) \end{aligned}$$

The valid advection-velocity relation for the slow wave (with $c^s(A) > 0$) is $c_+^s(A)$ because $c^s|_{A=0} \equiv \sqrt{\varepsilon} c_1^s$.

5.4 Critical velocity and critical advection strength

In the (ε, β, A) parameter space, there exists a critical surface $(\varepsilon_{cr}, \beta_{cr}, A_{cr})$ of co-dimension one, that separates the excitable and the non-excitable parameter regime. At $(\varepsilon_{cr}, \beta_{cr}, A_{cr})$, the single homoclinic solution of Eqs. (5.9),(5.10) corresponds to the connection between the fast wave branch and the slow wave branch, and the propagation velocity of the stable fast wave is minimal $(c_{cr}(A_{cr}))$. This critical velocity $(c_{cr}(A_{cr}))$ is calculated here. Also an expression for A_{cr} is captured.

We want to mention that in [51] an analytical expression for the critical velocity and the critical advection strength derived from the nonlinear Eikonal equation Eq. (5.21) is proposed (see Appendix, Eq. (9)). This mathematical framework provides a good approximation for $A < 0$, but fails for $A > 0$, see Fig. 5.3.

To calculate $c_{cr}(A_{cr})$ and A_{cr}, we start from the FHN model without advection Eqs. (5.1)-(5.2). The critical surface of co-dimension one is a line in the (ε, β) parameter space. At this critical line $(\varepsilon_{cr}, \beta_{cr})$, the propagation velocity of the fast wave is minimal $(c_{cr}|_{A=0})$.

The critical time scale ratio ε_{cr} as a function of β can be approximated by solving

$$c^s|_{A=0} \quad = \quad c^f|_{A=0} \tag{5.25}$$

for ε_{cr}, where $c^f|_{A=0}$ and $c^s|_{A=0}$ are calculated using a singular perturbation theory Eqs. (5.17),(5.18). This yields

$$\varepsilon_{cr}^{\pm}(\beta) \quad = \quad \frac{-2c_0c_1^f + c_1^{s2} \pm \sqrt{-4c_0c_1^fc_1^{s2} + c_1^{s4}}}{2c_1^{f2}}, \tag{5.26}$$

where $\varepsilon_{cr}^- < \varepsilon_{cr}^+$ and thus $\varepsilon_{cr} = \varepsilon_{cr}^-$.

For the critical velocity $c_{cr}|_{A=0}$ as a function of β we obtain from Eqs. (5.17),(5.18)

$$c_{cr}|_{A=0} \quad = \quad c_0 + \varepsilon_{cr}c_1^f = \sqrt{\varepsilon_{cr}}c_1^s. \tag{5.27}$$

Advection changes the critical velocity. To obtain an analytical expression for $c_{cr}(A_{cr})$, we again start from Eqs. (5.15),(5.16), which have the same form as FHN model without advection Eqs. (5.3),(5.4). Substituting c^* for $c_{cr}|_{A=0}$ and ε^* for ε_{cr}, the homoclinic solution of Eqs. (5.15),(5.16) ceases to exist at the connection between the fast wave branch and the slow wave branch. Thus, the critical velocity $c_{cr}(A_{cr})$ in systems affected by advection can be derived from Eqs. (5.13),(5.14) by setting $c^* = c_{cr}|_{A=0}$ and $\varepsilon^* = \varepsilon_{cr}$. With $c^* = c(A) - A$ and $\varepsilon^* = \varepsilon\frac{c^*}{c(A)}$ it follows that

$$c_{cr}|_{A=0} \quad = \quad c_{cr}(A_{cr}) - A_{cr}, \tag{5.28}$$

$$\varepsilon_{cr} \quad = \quad \varepsilon\frac{c_{cr}|_{A=0}}{c_{cr}(A_{cr})}, \tag{5.29}$$

where $c_{cr}|_{A=0}$ is the minimal propagation velocity of the fast wave for $A = 0$ Eq. (5.27), and $c_{cr}(A_{cr})$ is the minimal propagation velocity of the fast wave, that can be achieved by influencing the system with critical advection of strength A_{cr}.

Solving Eq. (5.29) for $c_{cr}(A_{cr})$ and Eq. (5.28) for A_{cr}, we finally obtain

$$c_{cr}(A_{cr}) \quad = \quad \frac{\varepsilon}{\varepsilon_{cr}}c_{cr}|_{A=0}, \tag{5.30}$$

$$A_{cr} = c_{cr}(A_{cr}) - c_{cr}|_{A=0} \quad = \quad c_{cr}|_{A=0}(\frac{\varepsilon}{\varepsilon_{cr}} - 1). \tag{5.31}$$

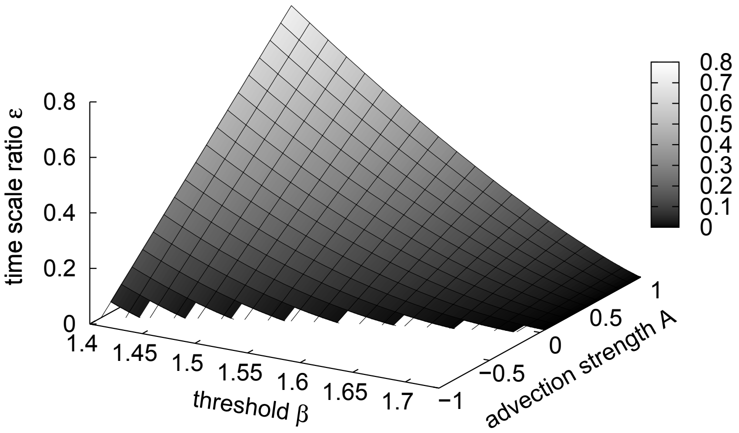

FIGURE 5.4: The critical surface in the (ε, β, A) parameter space derived from Eq. (5.32) separates the excitable (below) and the non-excitable (above) parameter regime. The colour code indicates the size of the time scale ratio ε.

The critical values $c_{cr}|_{A=0}$ Eq. (5.27) as well as ε_{cr} Eq. (5.26) are fully determined by β. Thus Eq. (5.31) is an approximation for the critical surface in the (ε, β, A) space, above which propagating waves are not supported. As a function of A and β, it reads

$$\varepsilon = \frac{(A + c_{cr}|_{A=0})\varepsilon_{cr}}{c_{cr}|_{A=0}}, \tag{5.32}$$

see Fig. 5.4. For values of ε above this critical surface, wave propagation is impossible.

5.5 Numerical validation

Here, the analytically calculated advection-velocity relation for the slow wave Eq. (5.22) as well as the nonlinear Eikonal equation Eq. (5.21), which provides the advection-velocity relation for the fast wave, are compared to the propagation velocity of the fast $c^f(A)$ and slow wave $c^s(A)$ numerically obtained from Eqs. (5.11),(5.12) as a function of A, Fig. 5.5 a,b.

Referring to systems without advection, the propagation velocity $c(A)$ is decelerated for negative advection $A < 0$ and accelerated for positive advection $A > 0$. We find that Eq. (5.22) is in good accordance with numerical results. Close to the point where the fast wave branch and the slow wave branch meet, the advection-velocity relation for the slow wave deviates from numerical results because perturbation theory does not capture the bifurcation behaviour. The deviation of the fast wave velocity calculated from Eq. (5.21) from the numerically obtained results is relatively large. This deviation is a consequence

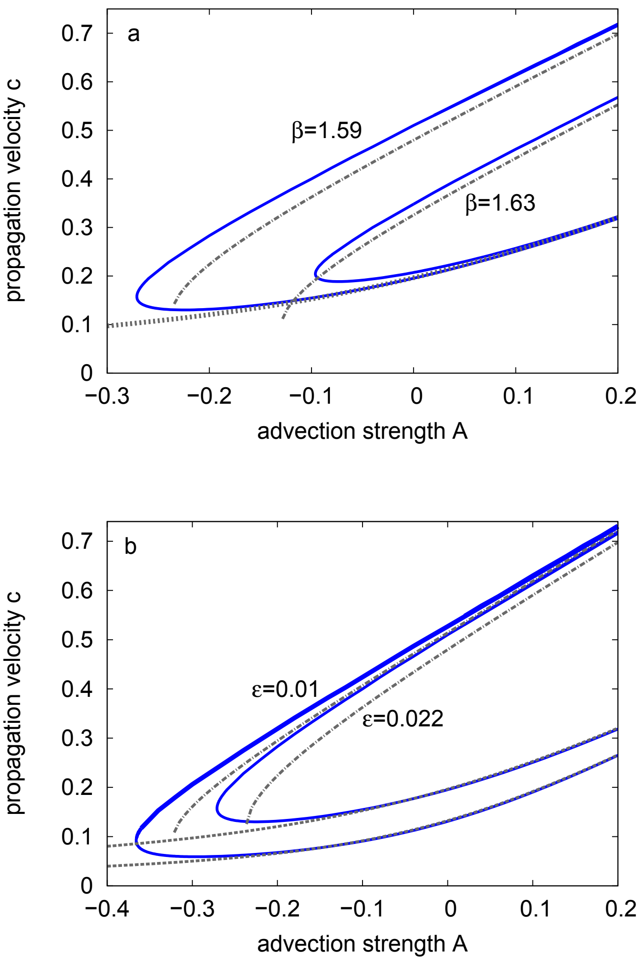

FIGURE 5.5: Propagation velocity c as a function of advection strength A. The grey dash-dotted lines show the velocity of the fast wave calculated from the nonlinear Eikonal equation ($c_+^f(A)$ of Eq. (5.21)). The grey dashed lines show the slow wave velocity derived from Eq.(5.22) ($c_+^s(A)$). The blue solid lines show the results numerically computed from Eqs. (5.11),(5.12). a) $\varepsilon = 0.022$, b) $\beta = 1.59$.

of the inaccuracy of the fast wave velocity $c^f|_{A=0}$ calculated from Eq. (5.17), which is a singular perturbation approximation up to first order of ε, see Fig. 5.2.

Furthermore, in Sect. 5.4, we found an analytical expression for the critical propagation velocity $c_{cr}(A_{cr})$ Eq. (5.30), which predicts an acceleration of the critical propagation velocity $c_{cr}(A_{cr})$ at larger threshold value β, see Fig. 5.6. For comparison, the propagation velocity of the fast $c^f(A)$ and slow wave $c^s(A)$ affected by advection of different strength A are numerically calculated as a function of β from Eqs. (5.11),(5.12), see Fig. 5.6. The fast and the slow wave branch meet at a critical velocity $c_{cr}(A_{cr})$. We find that Eq. (5.30) provides the same characteristic trend as numerical results.

Besides, numerical results in Fig. 5.6 show a shift of the propagation boundary ∂P (connection between fast and slow wave branch) to smaller threshold β for negative advection $A < 0$ and to larger threshold β for positive advection $A > 0$. This behaviour

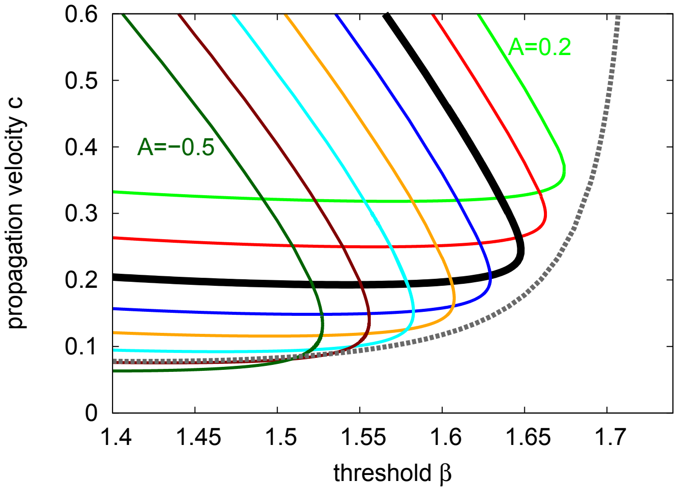

FIGURE 5.6: Critical propagation velocity $c_{cr}(A_{cr})$ as a function of threshold β (grey dashed line) derived from Eq. (5.30) with ε_{cr} from Eq. (5.26) and $c_{cr}|_{A=0}$ from Eq. (5.27). The coloured solid lines show the propagation velocity $c(A)$ of the fast and the slow wave numerically computed from Eqs. (5.11),(5.12) with varying advection strength A ($A = -0.5, -0.4, -0.3, -0.2, -0.1, 0.0, 0.1, 0.2$). $\varepsilon = 0.022$ in each case.

is predicted by Eq. (5.31), see Fig. 5.7. The critical line in the (β, A) parameter space separates the excitable ($A > A_{cr}$) and the non-excitable ($A < A_{cr}$) parameter regime. We find that Eq. (5.31) provides the same characteristic trend as numerical results, but deviates strongly from the numerical line for large negative advection strength $A < 0$. This is due to the fact that in this case, $\varepsilon^* = \varepsilon(1 - \frac{A}{c(A)})$ Eq. (5.14) is very large, and thus the singular perturbation theory is inaccurate.

A theoretical explanation of the stabilizing effect of positive advection has been found: every parameter point in the (ε, β) space can be allocated to a critical velocity Eq. (5.30). Media without advection are excitable if the propagation velocity of the fast wave is larger than this critical velocity (parameter regime above the critical line $\varepsilon_{cr}(\beta)$ Eq. (5.26)), and non-excitable if the propagation velocity of the fast wave is smaller than this critical velocity (parameter regime below the critical line $\varepsilon_{cr}(\beta)$). Negative advection $A < 0$ causes a deceleration of traveling waves, which in turn can induce a destabilization of an originally stable wave if the fast wave is decelerated below the critical velocity $c_{cr}(A_{cr})$ [51]. On the contrary, positive advection $A > 0$ causes an acceleration of traveling waves, which in fact can induce stable wave propagation in the former non-excitable parameter regime if the fast wave is accelerated above the critical velocity $c_{cr}(A_{cr})$.

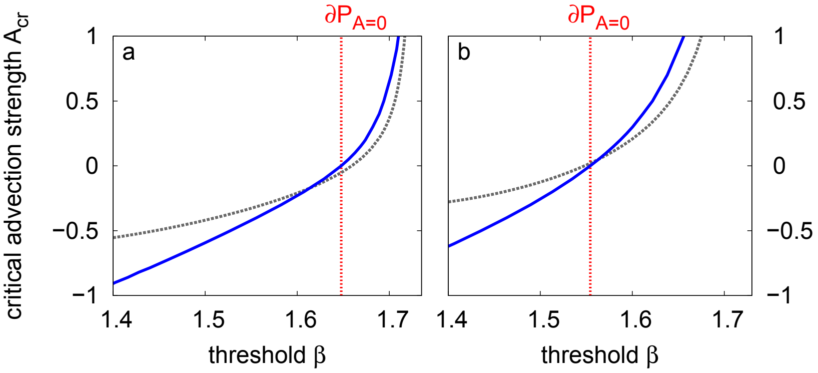

FIGURE 5.7: Critical advection strength A_{cr} as a function of threshold β for two different values of time scale ratio ε, (a) $\varepsilon = 0.022$, b) $\varepsilon = 0.1$). The grey dashed line shows the results derived from Eq. (5.31) with ε_{cr} from Eq. (5.26) and $c_{cr}(A_{cr})$ from Eq. (5.27); the blue solid lines show the results numerically computed from Eqs. (5.11),(5.12). The propagation boundary $\partial P_{A=0}$ is numerically computed from Eqs. (5.1),(5.2).

5.6 Conclusion

In this chapter, we described the dependency of the propagation velocity of an unstable slow traveling wave $c^s(A)$ on advection of strength A analytically Eq. (5.22) and numerically. Furthermore, we have shown that positive advection $A > 0$, corresponding to a constant field externally applied parallel to the propagation direction or, respectively, corresponding to small positive curvature of a wave front (V-shaped pattern), can induce stable propagation of traveling waves in the non-excitable parameter regime. This behaviour is explained analytically: Every point in the (ε, β) space, where ε is the time scale ratio and β is a measure for the threshold of the system, is related to a critical velocity $c_{cr}(A_{cr})$ Eq. (5.30). $c_{cr}(A_{cr})$ is the propagation velocity at a saddle-node bifurcation of an unstable slow and a stable fast traveling wave solution, thus the minimal possible velocity of the fast wave solution. Stable wave propagation in the non-excitable parameter regime now is induced by accelerating the fast wave velocity above the critical velocity by affecting it with advection larger than a critical advection strength A_{cr} Eq. (5.31). We derived an analytical approximation of a critical surface in the (ε, β, A) space Eq. (5.32), above which wave propagation is impossible. Finally, we confirmed numerically that the calculated dependencies of the critical velocity $c_{cr}(A_{cr})$ and the critical advection strength A_{cr} on β and ε are valid.

Chapter 6

Nucleation of reaction-diffusion waves on curved surfaces

In this Chapter, we study reaction-diffusion waves on curved 2D surfaces, and determine the influence of curvature upon the nucleation and propagation of spatially localized waves in an excitable medium modeled by the FHN system. In Sect. 6.1, we present the internal feedback control used to stabilize unstable localized waves and introduce the modeling of a curved medium. In Sect. 6.2, we discuss wave solutions on a torus, which represents a curved surface on which locally both positive and negative Gaussian curvature occurs. We consider ring waves, wave segments and particle-like waves (critical nuclei) stabilized by feedback control. Then, we specifically study ring wave break-up, Sect. 6.3, curvature-induced changes of nucleation, Sect. 6.4, and curvature-induced stabilization of wave-segments, Sect. 6.5. So far, the restriction is made that the center of mass of the critical nuclei is pinned on the torus inside and outside respectively. In Sect. 6.6, we analyze, how localized wave segments without this restriction evolve.

Parts of this chapter are published in [84].

6.1 Methods

In a spatial 2D medium, depending upon the set of parameters (ε, β), there exist different wave solutions [3, 88]. Here, we focus on localized wave segments, which may either shrink or expand, as they propagate, or, in the limit case, remain unchanged in size and shape, in which case they are called *particle-like waves* [31].

For each set of parameters (ε, β) with $\beta < \beta_{\partial R_\infty}$ (or $\varepsilon < \varepsilon_{\partial R_\infty}$, respectively) there exists a localized wave solution (wave segment), which represents a critical spatio-temporal structure, i.e., a particle-like wave.

In a co-moving frame Eqs. (4.8),(4.9), the localized critical structure is related to a saddle-point with a single unstable eigenvector (one-dimensional unstable manifold) in phase space. The curve representing this solution in a parameter plane of the bifurcation diagram is called the rotor boundary ∂R. In phase space, the stable manifold of states on ∂R separates the attractor of a spiral wave (spatially non-confined) and the stable, spatially uniform steady state. Thus, when the form of this particle-like wave is perturbed, it either grows to a spiral wave or shrinks and disappears. Perturbations above the critical size of the particle-like wave grow, while perturbations below that critical nucleus shrink to the stable uniform state, i.e., the wave segments retracts. The internal cortical control of such particle-like waves may be viewed as a strategy of the cortex to avoid re-entrant spiral waves, e.g., in migraine. Changing the nucleation size of this critical structure changes the susceptibility to pathological conditions such as spreading depression.

In Fig. 6.1, we show the rotor boundary ∂R (black dashed) in a schematic bifurcation diagram of wavesize S as a function of the threshold parameter β. It separates the weakly excitable parameter regime (perturbations grow to a spiral wave) from the subexcitable parameter regime (wave segments in 2D shrink in length, while in spatially 1D systems wave propagation is stable). There exists another boundary ∂R_∞ (dash-dotted vertical line), independent of size S, to the right of which all wave segments retract (corresponding to infinitely large critical size). Furthermore, the propagation boundary ∂P_{1D} is shown, which separates the subexcitable parameter regime from the nonexcitable regime. In the nonexcitable parameter regime, perturbations shrink also in width and wave segments collapse, i.e., even in spatially 1D systems no wave propagation is possible.

At this point, we would like to remark that the critical nucleus (particle-like wave), which has the dynamic signature of a saddle-point, can be stabilized by an internal feedback control loop, which controls the excitation threshold β in Eq. (4.4), that is,

$$\beta \quad = \quad \beta_0 + KS(t), \tag{6.1}$$

where K is the control strength, and the size of the wave segment

$$S(t) = \int_{\mathbb{R}^2} \Theta\left(u\left(\mathbf{r}, t\right) - u_e\right) \, d^2\mathbf{r} \tag{6.2}$$

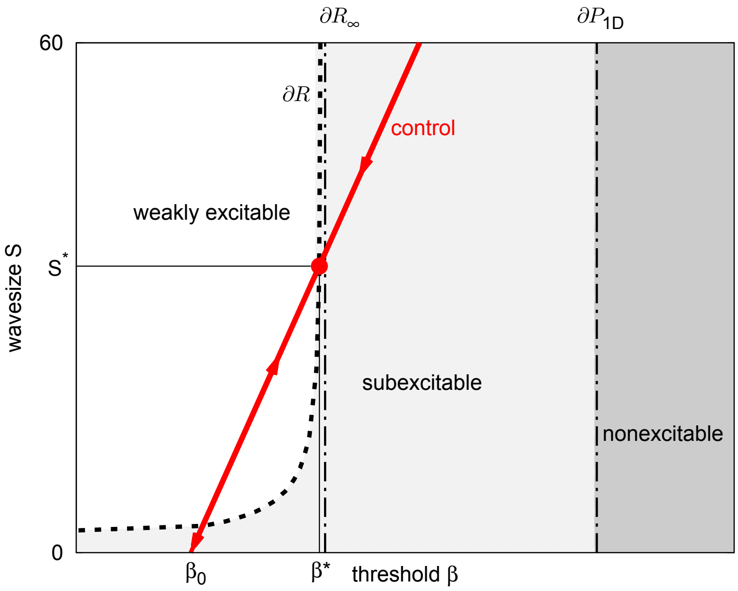

FIGURE 6.1: Schematic phase diagram of different regimes of the FithHugh-Nagumo model in the plane of wavesize S and threshold β for fixed ε: weakly excitable (perturbations grow to spiral waves); subexcitable (perturbations shrink in length); nonexcitable (perturbations shrink in width, no propagation in one dimension). The respective boundaries are marked by ∂R_∞ and ∂P_{1D}. ∂R denotes the boundary of the critical nucleus of size S below which perturbations shrink. The red solid line marks the control loop, which stabilizes the critical nucleus (S^*, β^*) indicated by a red dot.

is defined by the Heavyside function Θ. S represents a measure of the active area occupied by the wave segment, where u is larger than a defined threshold u_e. Here, u_e is chosen to be zero, compare Fig. 4.1.

Eq. (6.1) defines a control line (red solid line with arrows) in the (β, S) phase diagram Fig. 6.1. As the temporal evolution of a perturbation in a controlled system is confined to the control line, it asymptotically approaches a stable wave segment (β^*, S^*) if perturbed with convenient initial conditions. This follows from Fig. 6.1 since wave segments above ∂R, i.e., $\beta < \beta^*$, grow in size, while wave segments below ∂R, i.e., $\beta > \beta^*$, shrink.

In the following simulations we will apply the internal feedback mechanism Eq. (6.1) to stabilize the critical nucleus. Furthermore, we will study the influence of the curvature of the excitable medium on the stability of localized waves. Hence the Laplace operator ∇^2 must be replaced by the Laplace-Beltrami operator Δ_{LB} [89] for surfaces given in curvilinear coordinates α^i with $i = 1, 2$,

$$\Delta_{LB} = \sum_{i,j=1}^{2} g^{-\frac{1}{2}} \frac{\partial}{\partial \alpha^i} \left(g^{\frac{1}{2}} g^{ij} \frac{\partial}{\partial \alpha^j} \right), \tag{6.3}$$

where $g = \operatorname{Det} \mathbf{G}$ and $\mathbf{G}$ with the matrix elements g^{ij} is the metric tensor of the parametrization, see Appendix.

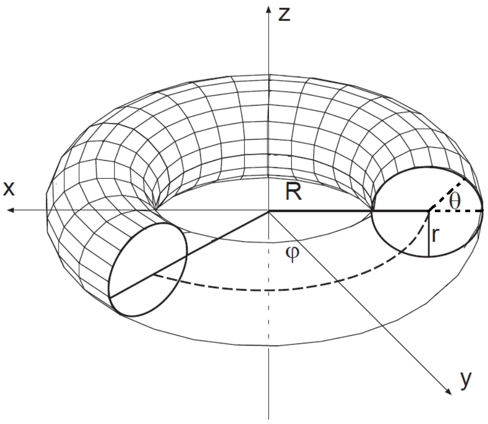

FIGURE 6.2: Parametrization of a torus by coordinates (θ, φ).

The surface of a torus in the Euclidian space $\mathbb{R}^3$ can be described by the parametrization (θ, φ) of the position vectors

$$(\theta, \varphi) \quad \mapsto \quad \begin{pmatrix} (R + r\cos\theta)\cos\varphi \\ (R + r\cos\theta)\sin\varphi \\ r\sin\theta \end{pmatrix} = \begin{pmatrix} x \\ y \\ z \end{pmatrix}. \tag{6.4}$$

The geometrical meaning of the major curvature radius R and the minor curvature radius r and of the angles θ and φ is visualized in Fig. 6.2.

The Laplace-Beltrami operator in torus coordinates reads

$$\boldsymbol{\Delta}_{LB} \quad = \quad -\frac{\sin\theta}{r(R + r\cos\theta)}\frac{\partial}{\partial\theta} + \frac{1}{r^2}\frac{\partial^2}{\partial\theta^2} + \frac{1}{(R + r\cos\theta)^2}\frac{\partial^2}{\partial\varphi^2}. \tag{6.5}$$

We investigate sections of a torus with Neumann boundary conditions (no flux boundary) on the equatorial section (at $\theta = 0$ and $\theta = \pi$) and periodic boundary conditions in the direction of the azimuthal angle φ. This restricts all traveling wave solutions, as they have to obey the symmetries defined by these boundary conditions, i.e., the center of mass of the critical nuclei is pinned either on the outside or inside of the torus.

6.2 Overview of wave solutions on a torus

The main results are twofold. First, by investigating excitation waves on a torus, we show that the Gaussian curvature of the excitable medium changes the nucleation threshold systematically. Second and more surprisingly, we observe that a curved medium can even induce a change of stability. Unstable critical nuclei are transformed into stable propagating localized wave segments.

We analyze the nucleation of excitation waves in reaction-diffusion media on curved 2D surfaces, specifically on tori. A torus has positive Gaussian curvature on the outside ($\theta = 0$) and negative Gaussian curvature on the inside ($\theta = \pi$) and a continuous transition in between, with vanishing Gaussian curvature on the top ($\theta = \frac{\pi}{2}$) and bottom ($\theta = \frac{3\pi}{2}$), see Fig. 6.2. In general, a torus has, in contrast to a sphere, not only locally varying and even negative Gaussian curvature, but a torus also admits a global isothermal coordinate system, called toroidal coordinates, that is, coordinates, where the metric is locally conformal to the Euclidean metric, see Appendix. Therefore, an intuitive understanding of some of our results can be based on the particularly simple form of the Laplace-Beltrami operator in these coordinates.

On tori, a stable solution besides the spatially homogeneous steady state are ring-shaped propagating wave solutions (autowaves). The stable manifold of states on the curve of the critical nucleus separates the attractor of a ring-shaped autowave and the spatially uniform steady state. Ring-shaped autowaves have been analyzed and, in particular, their critical properties have been discussed, namely autowave fronts with sufficiently large geodesic curvature break up on the torus inside [83]. We reconsider these autowaves in order to compare them with the dynamics of critical nuclei.

We restrict our study to nucleation of waves propagating strictly in the direction of the azimuthal angle φ (see Sect. 6.1) and, furthermore, the center of mass of the nucleation is pinned either on the outside or inside of the torus, i.e., the locations where the extreme values of the Gaussian curvature occur. In the following, we will simply refer to these solutions as inside or outside critical nuclei or, if stabilized, inside or outside traveling wave solutions. These solutions are the symmetric solutions with respect to the equatorial section of the torus. Examples of solutions on the torus without this restriction are shown in Sect. 6.6.

Note that the open ends of the two symmetric critical nuclei on the outside and inside extend in the direction of θ (perpendicular to the propagation direction), that is, into regions of decreasing and increasing Gaussian curvature, respectively. Our results are mainly explained by this gradient in the Gaussian curvature and not by the absolute value of the Gaussian curvature.

The results are displayed in two bifurcation diagrams. First, the same bifurcation diagram as already introduced in Sect. 6.1 to define the regimes of excitability (weakly, sub-, and nonexcitable, see Fig. 6.1) is shown in Fig. 6.3. The size S of the critical nucleus Eq. (6.2) is plotted versus the threshold parameter β of the local dynamics of the FHN system Eqs. (4.3),(4.4). The reference branch of the critical nucleus from simulation on a flat medium (black dashed), now labeled “flat” in Fig. 6.3, separates the

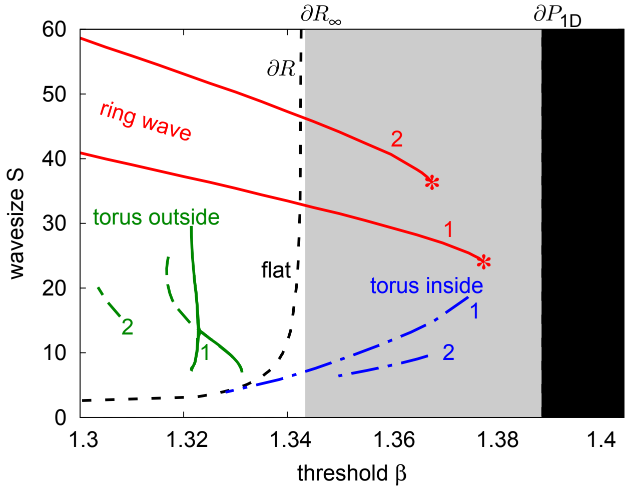

Figure 6.3: Bifurcation diagram of wavesize S as a function of threshold parameter β computed from Eqs. (4.3),(4.4) with $D = 0.12$ and $\varepsilon = 0.36$; critical nucleus on a flat surface (black dashed line); 1) solutions on a torus with minor curvature radius $r = \frac{20}{2\pi}$ and major curvature radius $R = \frac{80}{2\pi}$; 2) solutions on a torus with minor curvature radius $r = \frac{20}{2\pi}$ and major curvature radius $R = \frac{40}{2\pi}$; stable ring wave solutions (red solid lines) with points of excitation block, i.e., propagation suppression (red asterisks); unstable inside critical nucleus (blue dash-dotted lines); unstable outside critical nucleus (green dashed lines); stable stationary and maximum and minimum size of stable oscillating localized wave segment on the torus outside (green solid lines). Feedback Eq. (6.1) is applied to stabilize the states on the dashed and dash-dotted curves.

weakly excitable regime (to the left, decreasing β) from the subexcitable regime (to the right, increasing β), which ends at $\beta = \partial P_{1D}$, where the nonexcitable regime is reached.

In Fig. 6.3, we show further solution branches simulated on two different tori. The torus labeled 1 has lower absolute values of Gaussian curvature than the torus labeled 2, since the latter torus has a twice smaller value of major curvature radius R. For each torus, we show the branch of the ring-shaped autowave solutions (red solid). Furthermore, for each torus, we show the branch of the inside (blue dash-dotted) and outside (green dashed) critical nucleus. The states on the curves of the critical nucleus (dashed or dash-dotted) are stabilized by applying an appropriate global feedback Eq. (6.1) with suitably chosen β_0 and K such that the respective state (β^*, S^*) is at the intersection with the line given by Eq. (6.1). In addition, on the torus outside, we find stable wave segments and stable oscillating waves (green solid), see Sect. 6.5.

Second, Fig. 6.4 is a bifurcation diagram, where the propagation velocity c, see Eqs. (4.8),(4.9), is plotted versus the threshold parameter β. The reference branches are on the one hand the propagation velocities of the stable fast and the unstable slow wave solutions in spatially 1D systems (grey dashed), and, on the other hand, a critical velocity c_{cr} (black solid), below which stable wave propagation cannot be obtained, compare Sect. 5.4.

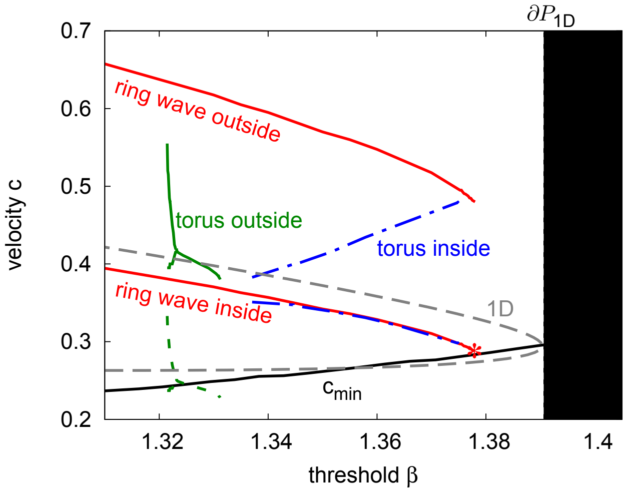

FIGURE 6.4: Bifurcation diagram of propagation velocity c as a function of threshold β computed from Eqs. (4.3),(4.4) with $D = 0.12$ and $\varepsilon = 0.36$ on a torus with minor curvature radius $r = \frac{20}{2\pi}$ and major curvature radius $R = \frac{80}{2\pi}$; propagation velocity of stable ring wave solutions (red solid lines) on the torus outside (upper line) and torus inside (lower line) with point of excitation block (red asterisk); propagation velocity of inside critical nuclei (blue dash-dotted lines) at center of mass (lower line) and open ends (upper line); propagation velocity of stable stationary and stable oscillating localized outside wave segment (green solid lines) at center of mass (upper line) and at open ends (lower line); hypothetical propagation velocity of outside stable wave segments (green dashed line) on torus inside; critical propagation velocity c_{cr} here denoted as c_{min} (black solid line) calculated from Eq. (5.30) with $c_{cr}|_{A=0}$ and ε_{cr} computed from Eqs.(4.3),(4.4) in one spatial dimension; propagation velocity of the stable and unstable wave solution in 1D (grey dashed). Feedback Eq. (6.1) is applied to stabilize the states on the blue dash-dotted curves.

Further, we show solution branches simulated on the less curved torus (torus 1). Two branches show the propagation velocity c in azimuthal (φ) direction of the ring-shaped autowave solution (red solid), the lower one is the propagation velocity on the torus inside, the upper one is the propagation velocity on the torus outside. Furthermore, for the inside critical nucleus (blue dash-dotted), we display the propagation velocity in azimuthal (φ) direction at the center of mass (lower line) and at the open ends (upper line), where the open ends are defined as the most distant lateral location where the activator concentration u equals zero.

For the outside stable wave segments, we show the propagation velocity c at the center of mass (green solid) and, after the bifurcation to the oscillating parameter regime with decreasing threshold parameter β, the maximum and minimum propagation velocity of the stable oscillating wave segments. In addition, for the outside critical nucleus (with propagation velocity c_o), we plot a “hypothetical” branch (green dashed) that shows the propagation velocity $c_i = c_o\frac{R-r}{R+r}$, which a point of this wave segment would have on the torus inside if it would exist there.

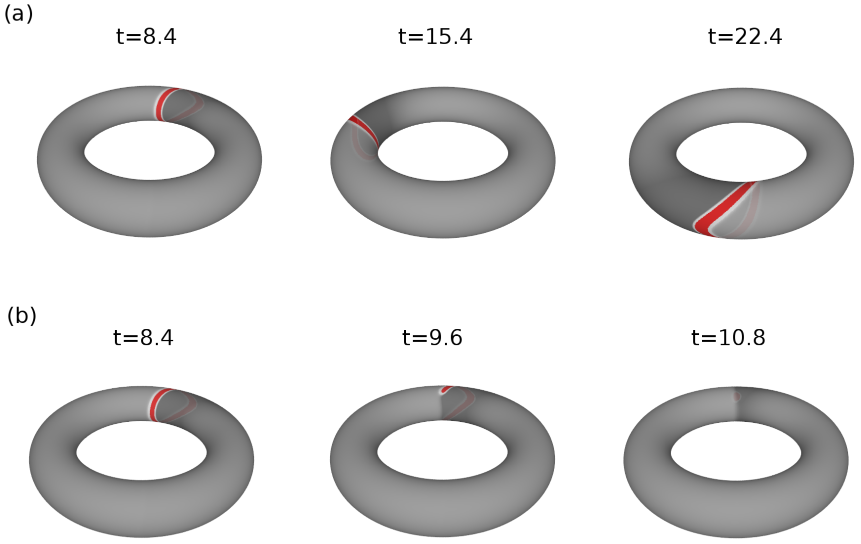

FIGURE 6.5: Snapshots of ring waves propagating counter-clockwise on a torus with minor curvature radius $r = \frac{20}{2\pi}$ and major curvature radius $R = \frac{80}{2\pi}$ computed from Eqs. (4.3),(4.4) with $D = 0.12$ and $\varepsilon = 0.36$. (a) Stable ring wave, $\beta = 1.378$. (b) Ring wave break-up, $\beta = 1.379$. (red) $u > 0$, (white) $u_s < u < 0$, (light grey) $u_s - 0.01 < u < u_s + 0.01$, (dark grey) $u < u_s - 0.01$.

6.3 Ring wave break-up at saddle-node bifurcation

First, we focus on the break-up of ring-shaped autowaves on tori. The ring-shaped autowave solution shown in Fig. 6.5 is a stable solution of Eqs. (4.3),(4.4). Thus the ring waves can be conceived as homoclinic solutions of the related ordinary differential Eqs. (4.8),(4.9) in a co-moving frame with $\xi = \varphi + ct$.

Ring waves have negative geodesic curvature on the torus inside and positive geodesic curvature on the torus outside, see Fig. 6.5(a). Thus, compared to 1D pulses (or infinitely extended wavefronts on a flat surface, respectively), ring waves propagate slower on the torus inside and faster on the torus outside, see Fig. 6.4 (red solid).

If the propagation velocity falls below the critical value c_{cr}, the ring waves break up on the torus inside [83], see Fig. 6.5(b). This excitation block is marked by an asterisk in Figs. 6.3 and 6.4. Below the critical velocity c_{cr}, stable wave propagation cannot be obtained.

For 1D waves, it is known that the excitation block is due to the coalescence of the homoclinic orbits of the fast and the slow wave (pulse) solution of the ODE problem Eqs. (4.8),(4.9) [87]. In the related PDE problem Eqs. (4.3),(4.4), the propagation boundary is a saddle-node bifurcation point of the stable fast wave branch and the unstable slow wave branch.

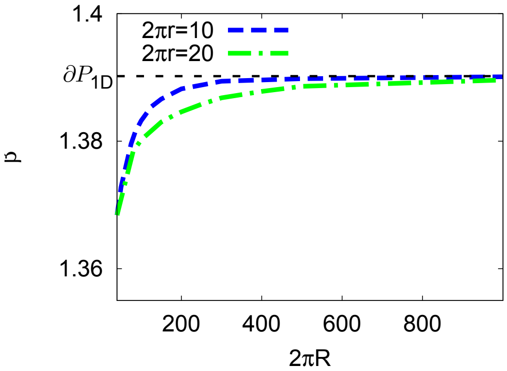

FIGURE 6.6: Excitation block of ring-shaped autowaves computed from Eqs. (4.3),(4.4) with $D = 0.12$ and $\varepsilon = 0.36$ on tori in the (R, β) parameter space. No propagation is possible above the critical curves for different r; ∂P_{1D} denotes the 1D propagation boundary.

In Fig. 6.4, the fast wave branch and the slow wave branch of 1D traveling wave solutions are shown (upper and lower dashed grey lines). At the propagation boundary ∂P_{1D}, they meet in a saddle-node bifurcation.

Also in curved 2D media, the excitation block is due to a saddle-node bifurcation, where the fast wave branch coincides with the slow wave branch in a saddle-node bifurcation. In the 1D limit $R \longrightarrow \infty$, the threshold β, at which the ring waves break up, converges to the propagation boundary ∂P_{1D}. This is shown in Fig. 6.6, where the lines show the excitation block in the (R, β) parameter space on two different tori; the upper line (dashed blue) is computed on a less curved torus with lower absolute values of Gaussian curvature compared to the lower line (dash-dotted green).

As shown in Sect. 5.4, the critical velocity c_{cr}, below which stable wave propagation is not possible, can be calculated with Eq. (5.30),

$$c_{cr} \quad = \quad \frac{\varepsilon}{\varepsilon_{cr}} c_{cr}|_{A=0}, \tag{6.6}$$

with ε_{cr} being the critical time separation parameter, where the homoclinic orbits of the 1D fast and slow wave (pulse) solution of the ODE Eqs. (4.8),(4.9) coincide, and $c_{cr}|_{A=0}$ is the corresponding critical velocity. For the line c_{cr} shown in Fig. 6.4, ε_{cr} and $c_{cr}|_{A=0}$ are computed with *AUTO* from Eqs. (4.3),(4.4) in one spatial dimension.

The propagation velocity c of ring waves is affected by both the parameters of the local dynamics (ε and β) and the Gaussian curvature Γ of the torus. An increase of β or ε causes a deceleration of the ring wave on the torus inside. Also an increase of the Gaussian curvature Γ of the torus causes an increase of the absolute values of the geodesic curvature of the ring wave, what results in a deceleration of the ring wave on the torus inside. Thus, on stronger curved tori (smaller R), the ring wave breaks up at smaller threshold β, see Fig. 6.6.

6.4 Curvature-induced changes of nucleation

Next, we analyze the nucleation of excitation waves on the torus inside (Sect. 6.4.1) and outside (Sect. 6.4.2), respectively.

6.4.1 Nucleation on the torus inside

The inside branches of the critical nucleus (blue dashed) in Fig. 6.3 are to the right (at larger threshold β) of the reference curve ∂R (rotor boundary on flat surfaces). The larger the size S of the critical nucleus is, the stronger is the shift towards larger threshold β. On the stronger curved torus (torus 2), the branch of the critical nucleus is shifted further. Thus, on the torus inside, critical nuclei exist in a parameter regime that is subexcitable on flat surfaces, compare Fig. 6.1.

A qualitiative explanation for this behaviour can be given by the relation of the Gaussian curvature Γ at the center of mass of the critical nucleus ($\theta = \pi$) and at the open ends of the critical nucleus. Mathematically, the Gaussian curvature is described by the Laplace-Beltrami operator Eq. (6.3) in torus coordinates [89]. A torus admits a global isothermal coordinate system, so-called toroidal coordinates $(\theta_i, \tilde{\varphi})$, i.e., orthogonal coordinates where the metric is locally conformal to the Euclidean metric. The Laplace-Beltrami operator Eq. (6.3) given in toroidal coordinates reads

$$\Delta_{LB} = \frac{(\cosh\eta - \cos\theta_i)^2}{a^2}\left(\frac{\partial^2 u}{\partial\theta_i^2} + \frac{\partial^2 u}{\partial\tilde{\varphi}^2}\right), \qquad (6.7)$$

where

$$a = (R^2 - r^2)^{\frac{1}{2}} \qquad (6.8)$$

is a measure for the scaling of the space,

$$\eta = \operatorname{arcoth}\left(R/\left(R^2 - r^2\right)^{\frac{1}{2}}\right) \qquad (6.9)$$

is a measure for the relation between the major radius R and the minor radius r and

$$\tilde{\varphi} = \varphi \sinh\eta. \qquad (6.10)$$

The derivation can be found in the Appendix.

Introducing an effective coupling strength $C(\theta_i) = (\cosh\eta - \cos\theta_i)^2/a^2$, a torus can mathematically be interpreted as a flat medium with diffusion being a function of the location θ (θ_i can be expressed in terms of θ, see Appendix), i.e., $\tilde{D}(\theta) = DC(\theta)$. The coupling strength $C(\theta)$ is strictly monotonically increasing from the torus outside ($\theta = 0$) to the torus inside ($\theta = \pi$), see Fig. 6.7. For stronger curved tori, the gradient of $C(\theta)$ is larger.

The effective coupling strength $C(\theta)$ of the inside critical nucleus is larger at the center of mass than at the open ends. Thus, the resultant diffusion perpendicular to the propagation direction is directed towards the open ends. This counteracts the retraction of the open ends in the parameter regime which is subexcitable in a flat medium. Larger critical nuclei reach over a region of larger difference in effective coupling strength, thus the shift towards larger threshold β is stronger.

The propagation velocity c at the center of mass of the inside critical nucleus is similar to the propagation velocity of the ring-shaped autowaves at the torus inside, see Fig. 6.4.

6.4.2 Nucleation on the torus outside

On the torus outside, we find that, under certain conditions, unstable critical nuclei bifurcate into stable propagating wave segments (green solid line in Fig. 6.3). Furthermore, we find stable oscillating wave segments, whose size oscillates periodically in a self-sustained way. This striking bifurcation pattern will be explained in Sect. 6.5.

The outside branches (green) in Fig. 6.3 are to the left (at smaller threshold β) of the flat reference branch ∂R (black dashed). On more strongly curved tori, the branch of the critical nucleus is further shifted.

The coupling strength relation between the torus inside and outside also explains this behaviour. As the coupling strength $C(\theta)$ at the center of mass of the outside critical nucleus is smaller than at the open ends, the resultant diffusion perpendicular to the propagation direction is directed towards the center of mass, what enhances the retraction of the open ends.

On the torus outside, critical nuclei with increasing size S are found at decreasing threshold β. This is distinct from the inside nucleation branch and the flat reference branch: the larger the size S of the critical nucleus is, the larger is the difference between the coupling strength at the center of mass and the coupling strength at the open ends. Thus, larger critical nuclei at the torus outside are shifted to smaller threshold β, whereas on the torus inside larger critical nuclei are shifted to larger threshold β.

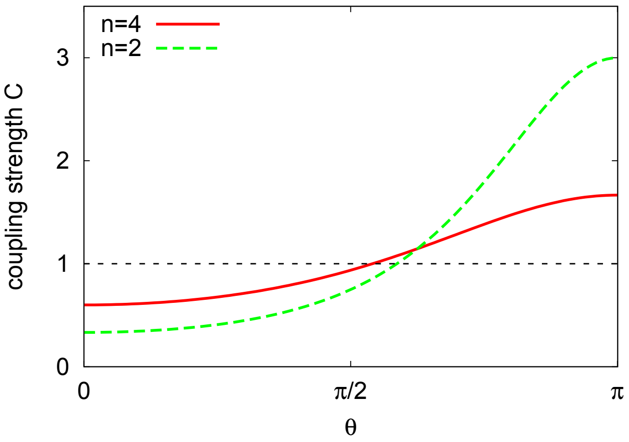

FIGURE 6.7: Coupling strength C as a function of common toroidal angular variable θ for two tori with different Gaussian curvature Γ with $n = R/r$ and $r = 1$.

Critical nuclei with small size S extend over an area with almost constant coupling strength C, see Fig. 6.7. This supports the assumption that the branches of the inside and outside critical nuclei with small wavesize S (not shown in Fig. 6.3) lie close to the flat reference branch. They probably are shifted parallel with respect to size S, as a constant coupling strength C equals a scaling of space. On the torus inside, they are shifted up to larger size S, on the torus outside down to smaller size S. This implies that at large threshold β the stable outside branch (green solid line in Fig. 6.3) terminates in a saddle-node bifurcation, and an unstable outside nucleation branch parallel to the flat reference branch exists at small wavesize S; this was, however, not resolved numerically.

6.5 Curvature-induced stabilisation

Depending upon the excitation parameter β, different space-time patterns occur, Fig. 6.8. Localized wave segments either may grow towards stable ring waves, Fig. 6.8(a), or they may shrink and vanish, Fig. 6.8(d). Additionally, as an effect of the curved surface, on the torus outside, we find stable propagating localized wave segments, see Fig. 6.8(c). Furthermore, we find stable oscillating wave segments, whose size oscillates periodically, see Fig. 6.8(b).

In Fig. 6.9, we show the activator profile of a stable wave segment propagating with a stationary profile, and in Figs. 6.10(a),(b), we show snapshots of the activator profile of an oscillating wave segment at its minimum size S and at its maximum size S, respectively.

The existence of stable wave segments on surfaces with positive Gaussian curvature can qualitatively be explained with the help of the space-dependent effective coupling

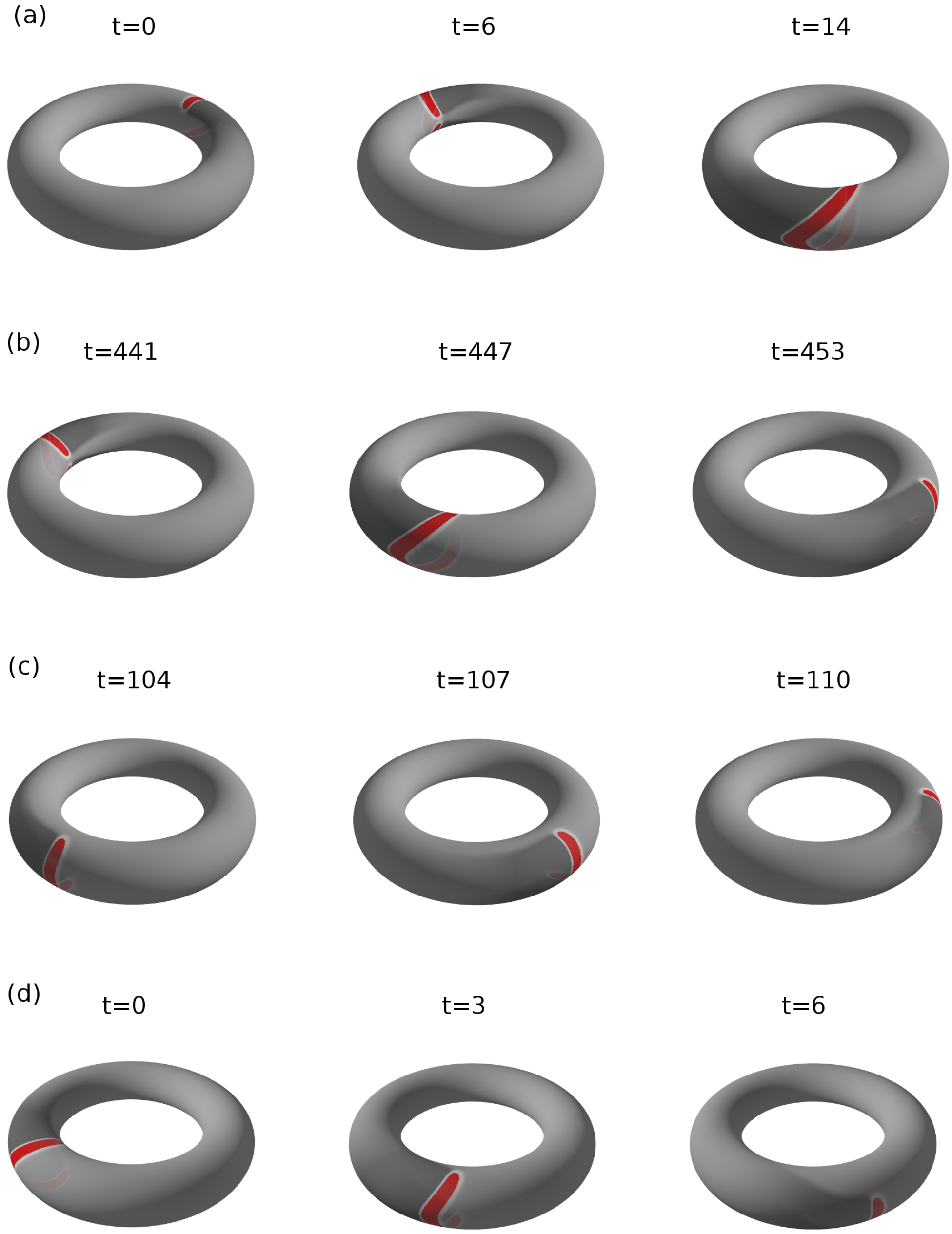

FIGURE 6.8: Snapshots of wave segments propagating counter-clockwise on a torus with minor curvature radius $r = \frac{20}{2\pi}$ and major curvature radius $R = \frac{80}{2\pi}$ computed from Eqs.(4.3),(4.4) with $D = 0.12$ and $\varepsilon = 0.36$. (a) Wave segment growing towards ring-shaped autowave, $\beta = 1.315$. (b) Oscillating wave segment, $\beta = 1.321476$. (c) Stable propagating wave segment, $\beta = 1.325$. (d) Wave segment shrinking towards homogeneous steady state, $\beta = 1.33$. (red) $u > 0$, (white) $u_s < u < 0$, (light grey) $u_s - 0.01 < u < u_s + 0.01$, (dark grey) $u < u_s - 0.01$.

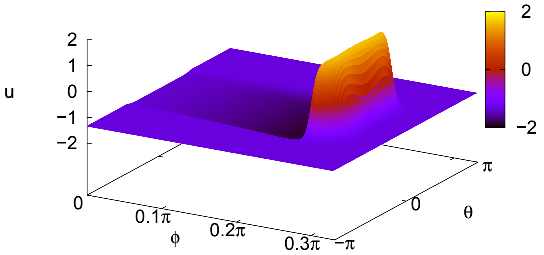

FIGURE 6.9: Snapshot of a stable propagating wave segment on the torus outside: activator concentration $u(\varphi, \theta)$ on a torus with minor curvature radius $r = \frac{20}{2\pi}$ and major curvature radius $R = \frac{80}{2\pi}$ computed from Eqs.(4.3),(4.4) with $\beta = 1.324$, $D = 0.12$ and $\varepsilon = 0.36$.

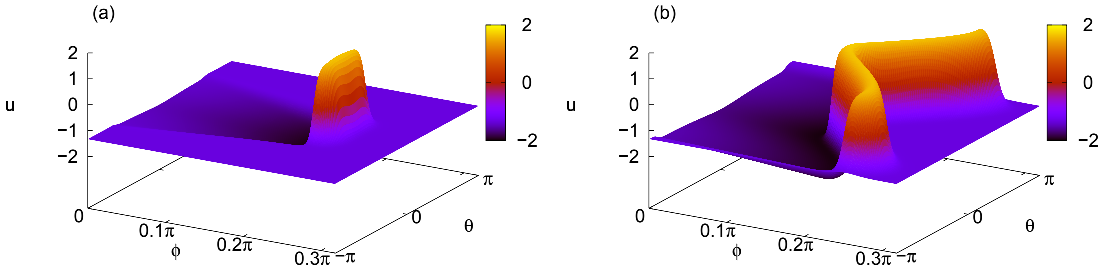

FIGURE 6.10: Snapshots of oscillating wave segment on the torus outside: same system as in Fig. 6.9 with $\beta = 1.321476$. (a) Minimum size, (b) maximum size. Time between minimum and maximum size $\Delta t = 14$.

strength C, as discussed in Sect. 6.4. The open ends of a stable wave segment on the torus outside lie in an area of the torus where the coupling strength C is larger than the coupling strength at $\theta = 0$, where the center of mass of the wave segment is located. Thus, the resultant effective diffusion perpendicular to the propagation direction caused by curvature is directed towards the center of mass of the wave segment. The larger the size S of the perturbation is, the stronger is this effect. At the same time, in the excitable parameter regime (see Fig. 6.1), small perturbations grow in length. If these two effects are balanced, we find stable propagating wave segments. In Fig. 6.3, we show the branch of stable wave segments (green solid). Perturbations with size S larger than the stable wave segments (and smaller than ring waves) shrink, as the difference in effective coupling strength between the center of mass and the open ends is large. Perturbations with size S smaller than the stable wave segments and larger than the small outside critical nucleus (which is not shown in Fig. 6.3 but supposed to lie close to the flat reference branch, see Sect. 6.4) grow, as the difference in coupling strength

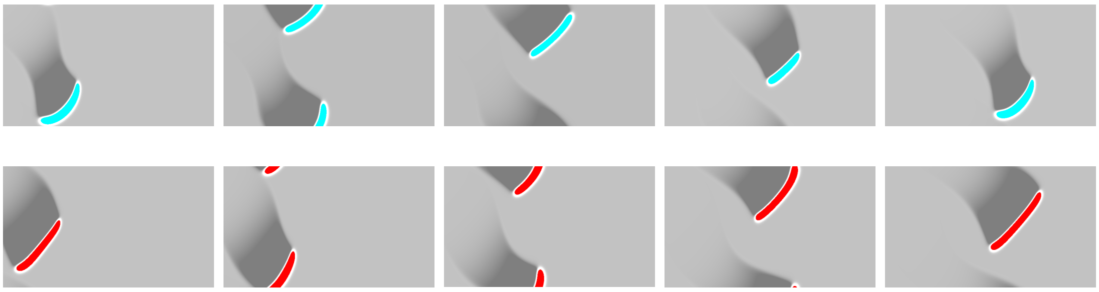

FIGURE 6.11: Snapshots over one cycle ($\Delta t = 8$) of wave segments on a section of a torus with minor curvature radius $r = \frac{20}{2\pi}$ and major curvature radius $R = \frac{80}{2\pi}$ computed from Eqs.(4.3),(4.4) with (cyan) and without (red) feedback control Eq. (6.1). $D = 0.12$, $\varepsilon = 0.36$. Left → right: $\varphi = 0 \to 7/6\pi$, up → down: $\theta = -\pi \to \pi$. (red/cyan) $u > 0$, (white) $u_s < u < 0$, (light grey) $u_s - 0.01 < u < u_s + 0.01$, (dark grey) $u < u_s - 0.01$. Areal distortions due to projection.

between the center of mass and the open ends is small.

In Fig. 6.4, we show the branch of the propagation velocity c at the center of mass of the stable wave segments and the stable oscillating wave segments (green solid). Furthermore, we show a hypothetical branch, the related propagation velocity at the torus inside (green dashed).

It is impossible that the stable wave segments grow to ring-shaped autowaves (without enlarging their geodesic curvature), as the hypothetical propagation velocity at the torus inside is smaller than the critical velocity c_{cr} (black solid line in Fig. 6.4).

For decreasing threshold β, the hypothetical propagation velocity at the torus inside of the stable outside wave solution (green dashed) accelerates, whereas the critical velocity c_{cr} (black solid) slows down. At the intersection point of these two branches, the stable wave solution bifurcates into a stable oscillating wave segment and an unstable critical nucleus. The stable oscillating wave segments grow in length, until the propagation velocity c of the open ends falls below the critical velocity c_{cr}. The open ends become unstable and decrease in width. Even if they continue growing in length, after the critical velocity c_{cr} is reached, the open ends asymptotically vanish.

6.6 Asymmetric solutions on a torus

In the previous sections (Sect. 6.4 and Sect. 6.5), we analyzed waves on tori propagating strictly in the direction of the azimuthal angle φ, with the center of mass being pinned either on the outside or on the inside of the torus. Here, we show examples of solutions on a torus without these restrictions. A symmetric perturbation on a torus that is not pinned does not propagate strictly in the direction of the azimuthal angle φ, but starts spiraling around the torus due to spontaneous symmetry breaking, see Fig. 6.11.

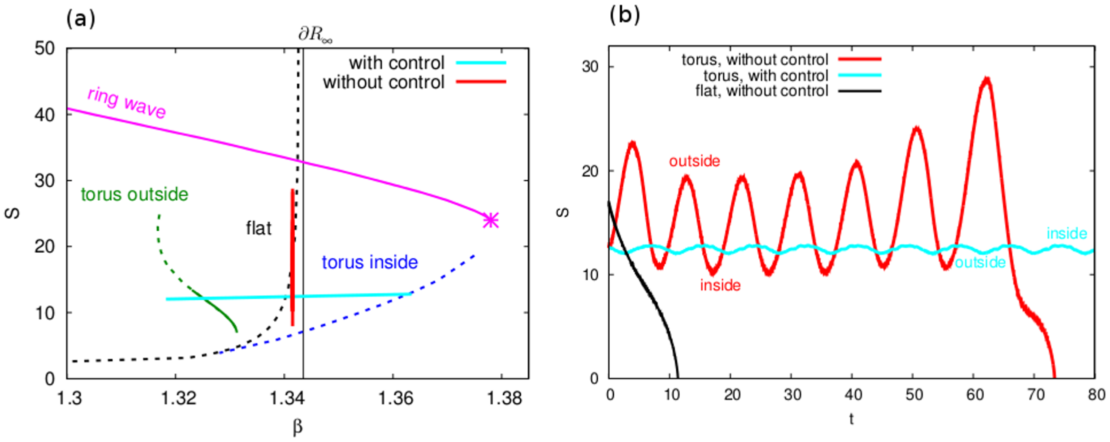

FIGURE 6.12: Evolution of wave segments on a torus with minor curvature radius $r = \frac{20}{2\pi}$ and major curvature radius $R = \frac{80}{2\pi}$ computed from Eqs. (4.3),(4.4) with and without feedback control Eq. (6.1). $D = 0.12$, $\varepsilon = 0.36$. (a) Evolution of wave segments in the (S, β)-bifurcation diagram Fig. 6.3. (b) Temporal evolution of wave size S on flat and curved surfaces.

In the FHN system with feedback control Eq. 6.1, the evolution of wave segments is determined by the control line, see Fig. 6.12(a). According to Eq. 6.1, a small wave segment has a small threshold β, the wave segment is in the excitable parameter regime and hence grows. Thereby, the threshold β is increased, until the wave segment is in the subexcitable parameter regime and starts shrinking on the torus inside. Spiraling around the torus, the wave segment remains oscillating in size, see Fig. 6.12(b).

In the FHN system without control, on flat surfaces, subthreshold excitations shrink and disappear very fast, see Fig. 6.12(b) (black line). On a torus, however, such localized wave segments can have a much longer lifetime, Fig. 6.12(b) (red line). This is due to the fact that the excitability of a medium depends on its curvature. On the torus inside, a comparatively small wave segment is in the weakly excitable parameter regime and thus grows. Meanwhile it propagates to the torus outside and now is in the subexcitable parameter regime and thus shrinks again, compare Fig. 6.12(a) (solid red line).

6.7 Conclusion

Here, we study the influence of the curvature of the cortex on CSD. For this purpose, nucleation and propagation of spatially localized reaction-diffusion waves are investigated on the surface of tori. These unstable structures, here denoted as critical nuclei, are stabilized by an internal feedback control Eq. (6.1). The restriction is made that the center of mass of the critical nuclei is pinned on the torus inside and outside respectively.

We showed that negative Gaussian curvature (torus inside) causes a shift of the nucleation branch to larger threshold β, i.e., superthreshold excitations grow in a parameter regime that is subexcitable on flat surfaces. On the torus outside with positive Gaussian curvature, the opposite effect is found, namely that in a parameter regime that is excitable on flat surfaces each excitation shrinks. In view of SD waves on the cortex, this might indicate, that SD is more likely to initiate and propagate in negative Gaussian curved areas. In addition, we made the surprising finding that curvature can induce a change of stability, i.e., on the torus outside, we found localized wave segments and wave segments periodically oscillating in size, that are stable propagating in systems without feedback control. The numerically calculated results are qualitatively explained with a so-called effective coupling strength, that can be found as a mathematical description of the Gaussian curvature on surfaces that admit isothermal coordinates.

Furthermore, we reinvestigated the behaviour of ring-shaped wave solutions (autowaves), which were first described by Davydov in 2003 [83]. Putting special remark on critical propagation effects, we confirmed that the propagation boundary of ring-shaped waves, constituting in a break-up on the torus inside, is caused by a saddle node bifurcation, where the fast wave branch coalesces with the slow wave branch. Thereby, the propagation velocity of ring-shaped waves is compared to the analytically calculated critical velocity c_{cr} Eq. 5.30 derived in Sect. 5.4.

Finally, we analyzed the evolution of wave segments on tori without pinning them on the torus inside or outside. We found that the lifetime of unstable wave segments spiraling around the torus is elongated due to curvature effects.

Chapter 7

Discussion

Knowledge about cellular processes involved in CSD and interference of CSD with external forces is of great relevance, not only for comprising the functionality of the human brain, but also for developing novel future therapies for this pathological states. In this thesis, we help to get a better understanding of the mechanisms that are causal for CSD by investigating both, cellular processes involved in CSD and interference of CSD with external forces.

Composing a biophysical neuronal model for CSD, we could evaluate the importance of specific cellular processes such as the ability of ion movement across the neuronal and glial membrane and clearance of excess ions by the vasculature and by lateral diffusion in the extracellular space and through glial and neuronal gap junctions. This has enabled us to develop hypotheses about when and why ionic homeostasis fails.

In detail, in Chapt. 2, we showed in a local system consisting of a neuronal, a glial and an extracellular compartment that uptake of excess ions from the extracellular space by astrocytes is crucial for ionic homeostasis. If the currents crossing the glial membrane are too weak or if the astrocytic reservoir is too small, ionic homeostasis fails. Then, after a super-threshold excitation, the system ends up in a pathological state, that is the second stable state of the system besides the physiological state. The pathological state with a depolarized neuronal membrane potential is close to Donnan equilibrium, i.e., the thermodynamic equilibrium of the system. The neuron cannot fire action potentials, because the electric energy that is usually stored in the ion gradients is almost fully dissipated. We showed that recovery succeeds if the astrocytic buffer mechanism is enhanced by increasing the strength of the glial transmembrane currents and, in particular, by enlarging the volume of the astrocyte. Depending on the parameter values, the pathological state becomes transient or disappears. In a parameter exploration, we identified the respective parameter regime.

However, we did not investigate the transition of the system from bistable to monostable in a bifurcation analysis. Especially knowledge about stability properties of the pathological state in the parameter regime, in which it is transient with a long relaxation time would be of interest, as we suppose that this state represents the temporary depolarization, that occurs during CSD.

In addition, we approximated the glial compartment as a bath. In this open system, we addressed the problem of electroneutrality and identified a model description, that ensures electroneutrality in all compartments. Furthermore, we found that in this monostable system the buffer mechanism is very strong, as the bath has infinite capacity to absorb excess ions from the extracellular space.

It is known that an increased potassium concentration in brain tissue can trigger CSD. Thus, it would be of interest, how variations of the ion concentration of the glial bath affect system dynamics. In detail, it could be analyzed by numerical trials, or better still, in a bifurcation analysis, whether increasing the potassium concentration of the bath changes system dynamics, e.g., as in the FHN model, from excitable to oscillatory.

To analyze whether lateral diffusion of ions in the extracellular space and through glial and neuronal gap junctions contributes to ionic homeostasis, we composed a spatially one-dimensional reaction-diffusion model consisting of three-compartmental neuronal elements, Chapt. 3. Thereby, we paid attention to electroneutral lateral diffusion. We investigated the stable propagating solutions of the system, i.e., excitation pattern, that propagate with constant shape and velocity. The system has, depending on the parameter values of the local elements and on the diffusion strength within the respective compartments, propagating front solutions, i.e., the buffer fails completely, or propagating pulse solutions, i.e., the system recovers after a transient period of depolarization. In addition, we identified a parameter regime, where no propagating solution exists. This behaviour is expected in healthy brain, where the buffer works regularly.

Our results in the ion-based reaction-diffusion model are won by numerical trials. We stimulated the medium by switching of the ion pumps at the neuronal membrane in an area of varying size for different durations. Then, we analyzed, which inhomogeneous solutions are triggered. However, we did not prove the uniqueness of the found solutions. This could be done in a bifurcation analysis, e.g., using the continuation software $AUTO$. However, this is not trivial for systems consisting of partial differential equations.

Another issue that was neglected throughout this thesis is the spatial coupling among the neurons by chemical synapses. We argued that the influence of chemical synapses on CSD is small, as action potentials occur on a much shorter timescale and, in addition, during the depolarization of CSD, no action potentials are generated. However, during the initial bursting of CSD, fast signal transmission through chemical synapses affects the tissue surrounding the current depolarization. That changes the properties of the medium for the incoming wave.

Nevertheless, our model provides a good overview of the neuronal mechanisms responsible for CSD. In future, it can be used to analyze effects of further cellular processes involved in CSD by including or leaving out specific currents.

To investigate the role of external influences such as the curvature of the cortex or an externally applied electrical field on CSD, we used the FHN model. This generic reaction-diffusion model also allows for analytical approximations, what provides more insight into the mathematical processes involved. In Chapt. 4, we showed that, although the approximate equations lose some of the physical meaning of the more complete biophysical model, the basic structure of bistability still holds. With a convenient inhibitor mechanism, both, the FHN model and the ion-based model, are excitable systems of type II. However, some of the characteristic features of the biophysical model are not captured by the FHN model, e.g., the bursting at the rising front.

With the FHN model, we studied the effect of advection in a one-dimensional medium, Chapt. 5. The advection term can describe an electrical field externally applied parallel to propagation direction and, in addition, advection in a one-dimensional medium is an approximation of the effect of front curvature on wave propagation in a two-dimensional medium. We derived an analytical expression for the advection-velocity relation of the slow wave, i.e., an unstable stationary propagating solution of the FHN model. This enabled us to calculate a critical advection strength, below which no stable wave propagation is possible. The critical advection strength depends on the parameter values of the system. This curve predicates, that negative advection can suppress wave propagation in the excitable parameter regime, whereas positive advection can induce wave propagation in the otherwise non-excitable parameter regime. We confirmed the calculated dependencies numerically.

However, modeling a wave affected by an externally applied electrical field with this reaction-diffusion-advection model implies that the wave consists of equally charged particles. In brain, positive and negative charged ions contribute to CSD. Thus, investigating the influence of an externally applied electrical field on wave propagation using the biophysical model would be of interest.

Last, to study the influence of the geometry of the brain on wave propagation, we studied FHN waves on curved two-dimensional surfaces, i.e., on the surface of a torus, Chapt. 6. We showed that negative Gaussian curvature (torus inside) can induce excitability in a parameter regime that is subexcitable on flat surfaces. In addition, we detected that curvature can induce a change of stability, i.e., on the torus outside, we found stable propagating localized wave segments, which are unstable structures on flat surfaces. Furthermore, we reviewed the behaviour of ring-shaped wave solutions, which were first described by Davydov in 2003 [83]. Using the results from Chapt. 5, we showed that the propagation boundary of ring-shaped waves, constituting in a break-up on the torus inside, is caused by a saddle-node bifurcation, where the fast wave branch coalesces with the slow wave branch. The critical minimal propagation velocity of ring-shaped waves hence can be calculated analytically.

In literature, the FHN system is frequently used to model several physiological systems. In Chapt. 4, we shortly motivated the application of the FHN model as a simplification of the ion-based model. However, there are many unanswered questions. E.g., a direct interpretation of the FHN parameter values in terms of biophysical properties is not possible. In addition, in spatially extended systems, it is still unknown whether the FHN model reflects macroscopic properties such as nucleation and propagation of ion-based models. Thus, thoroughly comparing the FHN model to biophysical more detailed models would be an interesting future project.

Bibliography

[1] H. Martins-Ferreira, M. Nedergaard, and C. Nicholson. Perspectives on spreading depression. *Brain Res. Rev.*, 32(1):215–234, 2000.

[2] J. P. Dreier. The role of spreading depression, spreading depolarization and spreading ischemia in neurological disease. *Nat. Med.*, 17:439–447, 2011.

[3] M. A. Dahlem, R. Graf, A. J. Strong, J. P. Dreier, Y. A. Dahlem, M. Sieber, W. Hanke, K. Podoll, and E. Schöll. Two–dimensional wave patterns of spreading depolarization: retracting, re-entrant, and stationary waves. *Physica D*, 239:889–903, 2010.

[4] R. FitzHugh. Impulses and physiological states in theoretical models of nerve membrane. *Biophys. J.*, 1:445, 1961.

[5] J. Nagumo, S. Arimoto, and S. Yoshizawa. An active pulse transmission line simulating nerve axon. *Proc. IRE*, 50:2061, 1962.

[6] A. L. Hodgkin, A. F. Huxley, and B. Katz. Measurement of current–voltage relations in the membrane of the giant axon of Loligo. *J. Physiol.*, 116:424–448, 1952.

[7] A. L. Hodgkin and A. F. Huxley. Currents carried by sodium and potassium ions through the membrane of the giant axon of Loligo. *J. Physiol.*, 116, 1952.

[8] A. L. Hodgkin and A. F. Huxley. The components of membrane conductance in the giant axon of Loligo. *J. Physiol.*, 116:473–496, 1952.

[9] A. L. Hodgkin and A. F. Huxley. The dual effect of membrane potential on sodium conductance in the giant axon of Loligo. *J. Physiol.*, 116:497–506, 1952.

[10] A. L. Hodgkin and A. F. Huxley. A quantitative description of membrane current and its application to conduction and excitation in nerve. *J. Physiol.*, 117:500, 1952.

[11] R. E. McAllister, D. Noble, and R. W. Tsien. Reconstruction of the electrical activity of cardiac Purkinje fibres. *J. Physiol.*, 251:1–59, 1975.

[12] D. DiFrancesco and D. Noble. A model of cardiac electrical activity incorporating ionic pumps and concentration changes. *Phil. Trans. R. Soc. B*, 307(1133):353–398, 1985.

[13] A. Karma. Spiral breakup in model equations of action potential propagation in cardiac tissue. *Phys. Rev. Lett.*, 71:1103–1106, 1993.

[14] C. Morris and H. Lecar. Voltage oscillations in the barnacle giant muscle fiber. *Biophys. J.*, 35:193, 1981.

[15] M. J. Gutnick and W. E. Crill. *The cortical neuron as an electrophysiological unit*, pages 33–51. Oxford University Press, 1995.

[16] R. D. Traub, R. K. Wong, R. Miles, and H. Michelson. A model of a CA3 hippocampal pyramidal neuron incorporating voltage-clamp data on intrinsic conductances. *Journal of Neurophysiology*, 66(2):635–650, 1991.

[17] R. D. Traub, J. G. Jefferys, R. Miles, M. A. Whittington, and K. Tóth. A branching dendritic model of a rodent CA3 pyramidal neurone. *J. Physiol. (Lond.)*, 48:79–95, 1994.

[18] H. Kager, W. J. Wadman, and G. G. Somjen. Simulated seizures and spreading depression in a neuron model incorporating interstitial space and ion concentrations. *J. Neurophysiol.*, 84:495–512, 2000.

[19] H. Kager, W. J. Wadman, and G. G. Somjen. Conditions for the triggering of spreading depression studied with computer simulations. *J. Neurophysiol.*, 88(5): 2700, 2002.

[20] H. Kager, W. J. Wadman, and G. G. Somjen. Seizure–like afterdischarges simulated in a model neuron. *J. Comput. Neurosci.*, 22:105–128, 2007.

[21] G. G. Somjen, H. Kager, and W. J. Wadman. Computer simulations of neuron–glia interactions mediated by ion flux. *J. Comput. Neurosci.*, 25(2):349–365, 2008.

[22] J. R. Cressman Jr., G. Ullah, J. Ziburkus, S. J. Schiff, and E. Barreto. The influence of sodium and potassium dynamics on excitability, seizures, and the stability of persistent states: I. Single neuron dynamics. *J. Comput. Neurosci.*, 26:159–170, 2009; Ibid., 30, 781 (2011).

[23] E. Barreto and J. R. Cressman. Ion concentration dynamics as a mechanism for neural bursting. *J. Biol. Phys.*, 37(3):361–373, 2010.

[24] N. Hübel, E. Schöll, and M. A. Dahlem. Bistable dynamics underlying excitability of ion homeostasis in neuron models. *PLoS Comp. Biol.*, 10:e1003551, 2014.

[25] B. Grafstein. Neuronal release of potassium during spreading depression. *Brain function*, 1:87–124, 1963.

[26] H. C. Tuckwell and R. M. Miura. A mathematical model for spreading cortical depression. *Biophys. J.*, 23:257–276, 1978.

[27] H. Huang, R. M. Miura, and W. Yao. A simplified neuronal model for the instigation and propagation of cortical spreading depression. *Adv. Appl. Math. Mech.*, 3:759–773, 2011.

[28] W. Yao, H. Huang, and R. M. Miura. A continuum neural model for the instigation and propagation of cortical spreading depression. *Bull. Math. Biol.*, 73:2773–2790, 2011.

[29] Y. Mori. A multidomain model for ionic electrodiffusion and osmosis with an application to cortical spreading depression. *arXiv*, 2014. URL `http://arxiv.org/abs/1410.8391`.

[30] I. Rubinstein. *Electro-Diffusion of Ions*. Studies in Applied Mathematics. Society for Industrial and Applied Mathematics, 1990.

[31] Tatsunari Sakurai, Eugene Mihaliuk, Florin Chirila, and K. Showalter. Design and control of wave propagation patterns in excitable media. *Science*, 296:2009–2012, 2002.

[32] K. Krischer and A. S. Mikhailov. Bifurcation to traveling spots in reaction-diffusion systems. *Phys. Rev. Lett.*, 73(23):3165–3168, 1994.

[33] M. Bode and H. G. Purwins. Pattern formation in reaction-diffusion systems-dissipative solitons in physical systems. *Physica D*, 86:53, 1995.

[34] C. P. Schenk, M. Or-Guil, M. Bode, and H. G. Purwins. Interacting pulses in three-component reaction-diffusion systems on two-dimensional domains. *Phys. Rev. Lett.*, 78:3781, 1997.

[35] M. Kim, M. Bertram, M. Pollmann, A. von Oertzen, A. S. Mikhailov, H. H. Rotermund, and G. Ertl. Controlling chemical turbulence by global delayed feedback: Pattern formation in catalytic CO oxidation on Pt(110). *Science*, 292:1357, 2001.

[36] V. S. Zykov, G. Bordiougov, H. Brandtstädter, I. Gerdes, and H. Engel. Global control of spiral wave dynamics in an excitable domain of circular and elliptical shape. *Phys. Rev. Lett.*, 92(1):018304, 2004.

[37] J. Schlesner, V. Zykov, H. Engel, and E. Schöll. Stabilization of unstable rigid rotation of spiral waves in excitable media. *Phys. Rev. E*, 74:046215, 2006.

[38] A. S. Mikhailov and K. Showalter. Control of waves, patterns and turbulence in chemical systems. *Phys. Rep.*, 425:79–194, 2006.

[39] M. A. Dahlem, F. M. Schneider, and E. Schöll. Failure of feedback as a putative common mechanism of spreading depolarizations in migraine and stroke. *Chaos*, 18:026110, 2008.

[40] F. M. Schneider, E. Schöll, and M. A. Dahlem. Controlling the onset of traveling pulses in excitable media by nonlocal spatial coupling and time delayed feedback. *Chaos*, 19:015110, 2009.

[41] Y. N. Kyrychko, K. B. Blyuss, S. J. Hogan, and E. Schöll. Control of spatio-temporal patterns in the Gray-Scott model. *Chaos*, 19(4):043126, 2009.

[42] J. Maselko and K. Showalter. Chemical waves on spherical surfaces. *Nature*, 339 (6226):609–611, 1989.

[43] A. Y. Abramychev, V. A. Davydov, and V. S. Zykov. Drift of spiral waves on nonuniformly curved surfaces. *J. Exp. Theor. Phys.*, 70:666, 1990.

[44] V. A. Davydov and V. S. Zykov. Kinematics of spiral waves on nonuniformly curved surfaces. *Physica D*, 49(1):71–74, 1991.

[45] V. A. Davydov and V. S. Zykov. Spiral autowaves in a round excitable medium. *J. Exp. Theor. Phys.*, 76(3):414–419, 1993.

[46] A. S. Mikhailov, V. A. Davydov, and V. S. Zykov. Complex dynamics of spiral waves and motion of curves. *Phys. D*, 70(1-2):1–39, 1994.

[47] V. A. Davydov, N. Manz, O. Steinbock, V. S. Zykov, and S. C. Müller. Excitation fronts on a periodically modulated curved surface. *Phys. Rev. Lett.*, 85:868–871, 2000.

[48] V. A. Davydov, V. G. Morozov, and N. V. Davydov. Ring-shaped autowaves on curved surfaces. *Phys. Lett. A*, 267(5):326–330, 2000.

[49] V. A. Davydov, N. Manz, O. Steinbock, and S. C. Müller. Critical properties of excitation waves on curved surfaces: Curvature-dependent loss of excitability. *Europhys. Lett.*, 59:344, 2002.

[50] N. Manz, V. A. Davydov, S. C. Müller, and M. Bär. Dependence of the spiral rotation frequency on the surface curvature of reaction–diffusion systems. *Phys. Lett. A*, 316(5):311–316, 2003.

[51] V. S. Zykov. *Simulation of Wave Processes in Excitable Media.* John Wiley & Sons Ltd (english translation from 1992), Moscow, 1984.

[52] M. Gómez-Gesteira, J. Mosquera, V. A. Davydov, V. Pérez-Muñuzuri, A. P. Muñuzuri, V.G. Morozov, and V. Pérez-Villar. Link between the effect of an electric field on wave propagation and the curvature-velocity relation. *Phys. Lett. A*, 231 (5–6):389, 1997.

[53] J. J. Tyson and J. P. Keener. Singular perturbation theory of traveling waves in excitable media (a review). *Physica D*, 32(3):327, 1988.

[54] G. Zhao and S. Ruan. Time periodic traveling wave solutions for periodic advection-reaction-diffusion systems. *J. Diff. Eq.*, 257(4):1078–1147, 2014.

[55] R. Friedrichs and A. Engel. Non-linear analysis of the Rosensweig instability. *Europhys. Lett.*, 63(6):8614, 2003.

[56] G. Bordyugov and H. Engel. Creating bound states in excitable media by means of nonlocal coupling. *Phys. Rev. E*, 74:016205, 2006.

[57] P. Colet, M. A. Matías, L. Gelens, and D. Gomila. Formation of localized structures in bistable systems through nonlocal spatial coupling I: General framework. *Phys. Rev. E*, 89(1):012914, 2014.

[58] J. Siebert, S. Alonso, M. Bär, and E. Schöll. Dynamics of reaction-diffusion patterns controlled by asymmetric nonlocal coupling as limiting case of differential advection. *Phys. Rev. E*, 89(5):052909, 2014.

[59] B. van der Pol. On relaxation oscillations. *Phil. Mag.*, 2:978–992, 1926.

[60] K. F. Bonhoeffer. Activation of passive iron as a model for the excitation of nerve. *J. Gen. Physiol.*, 32(1):69–91, 1948.

[61] K. F. Bonhoeffer. Modelle der Nervenerregung. *Naturwissenschaften*, 40(11):301–311, 1953.

[62] C. Lenk, M. Einax, and P. Maass. Irregular excitation patterns in reaction-diffusion systems due to perturbation by secondary pacemakers. *Phys. Rev. E*, 87:042904, 2013.

[63] S. Alonso, M. Bär, and A. V. Panfilov. Negative tension of scroll wave filaments and turbulence in three-dimensional excitable media and application in cardiac dynamics. *Bull. Math. Biol.*, 75(8):1351–1376, 2013.

[64] J. T. C. Schwabedal, A. B. Neiman, and A. L. Shilnikov. Robust design of polyrhythmic neural circuits. *Phys. Rev. E*, 90:022715, 2014.

[65] I. Omelchenko, A. Provata, J. Hizanidis, E. Schöll, and P. Hövel. Robustness of chimera states for coupled FitzHugh-Nagumo oscillators. *Phys. Rev. E*, 91:022917, 2015.

[66] M. Kantner, E. Schöll, and S. Yanchuk. Delay-induced patterns in a two-dimensional lattice of coupled oscillators. *Sci. Rep.*, 5:08522, 2015.

[67] M. A. Dahlem and S. C. Müller. Reaction-diffusion waves in neuronal tissue and the window of cortical excitability. *Ann. Phys. (Leipzig)*, 13(7-8):442–449, 2004.

[68] Z. F. Mainen and T. J. Sejnowski. Influence of dendritic structure on firing pattern in model neocortical neurons. *Nature (London)*, 382:363–366, 1996.

[69] E. J. Doedel and B. E. Oldeman. *Auto-07P: Continuation and bifurcation software for ordinary differential equations.* Concordia University, Montreal, Canada, 2009.

[70] E. M. Izhikevich. *Dynamical Systems in Neuroscience.* MIT Press, Cambridge, MA, 2007.

[71] G. B. Ermentrout and D. H. Terman. *Mathematical Foundations of Neuroscience.* Springer, New York, NY, 2010.

[72] G. Halnes, I. Østby, K. H. Pettersen, S. W. Omholt, and G. T. Einevoll. Electrodiffusive model for astrocytic and neuronal ion concentration dynamics. *PLoS Comput. Biol.*, 9(12):e1003386, 2013.

[73] T. Höfer, A. Politi, and R. Heinrich. Intercellular Ca^{2+} wave propagation through gap-junctional Ca^{2+} diffusion: A theoretical study. *Biophys. J.*, 80(1):75–87, 2001.

[74] C. Elphick, A. Hagberg, B. A. Malomed, and E. Meron. On the origin of traveling pulses in bistable systems. *Physics Letters A*, 230(1–2):33–37, 1997.

[75] M. A. Dahlem and S. C. Müller. Migraine aura dynamics after reverse retinotopic mapping of weak excitation waves in the primary visual cortex. *Biol. Cybern.*, 88: 419–424, 2003.

[76] M. A. Dahlem and E. P. Chronicle. A computational perspective on migraine aura. *Prog. Neurobiol.*, 74(6):351–361, 2004.

[77] M. A. Dahlem and S. C. Müller. Reaction–diffusion waves in neuronal tissue and the window of cortical excitability. *Ann. Phys.*, 13(7):442–449, 2004.

[78] R. G. Casten, H. Cohen, and P. A. Lagerstrom. Perturbation analysis of an approximation to the Hodgkin-Huxley theory. *Quart.Appl.Math.*, 32(4):365, 1975.

[79] N. Hübel and M. A. Dahlem. Dynamics from seconds to hours in Hodgkin-Huxley model with time-dependent ion concentrations and buffer reservoirs. *PLoS Comp. Biol.*, 10(12):e1003941, 2014.

[80] G. B. Ermentrout. Neural networks as spatio-temporal pattern-forming systems. *Rep. Prog. Phys.*, 61:335–430, 1998.

[81] F. Kneer, K. Obermayer, and M. A. Dahlem. Analyzing critical propagation in a reaction-diffusion-advection model using unstable slow waves. *Eur. Phys. J. E*, 38: 10, 2015.

[82] G. Bordyugov and H. Engel. Continuation of spiral waves. *Physica D*, 228(1):49–58, 2007.

[83] V. A. Davydov, V. G. Morozov, and N. V. Davydov. Critical properties of autowaves propagating on deformed cylindrical surfaces. *Physics Letters A*, 307:265–268, 2003.

[84] F. Kneer, E. Schöll, and M. A. Dahlem. Nucleation of reaction-diffusion waves on curved surfaces. *New J. Phys.*, 16:053010, 2014.

[85] J. Schütze, O. Steinbock, and S. C. Müller. Forced vortex interaction and annihilation in an active medium. *Nature*, 356(6364):45–47, 1992.

[86] B. Schmidt, P. De Kepper, and S. C. Müller. Destabilization of Turing structures by electric fields. *Physical review letters*, 90(11):118302, 2003.

[87] M. Krupa, B. Sandstede, and P. Szmolyan. Fast and slow waves in the FitzHugh-Nagumo equation. *J. Diff. Eq.*, 133(1):49, 1997.

[88] A. T. Winfree. Varieties of spiral wave behaviour: An experimentalist's approach to the theory of excitable media. *Chaos*, 1:303–334, 1991.

[89] W. Kühnel. *Differentialgeometrie.* Friedr. Vieweg & Sohn Verlag/GWV Fachverlage GmbH, Wiesbaden, 2005.

[90] A. S. Mikhailov. *Foundations of Synergetics Vol. I.* Springer, Berlin, 1994.

[91] P. Moon and D. E. Spencer. *Field Theory Handbook.* Springer, Berlin, 1971.

Appendix

A.1 1D description of curved 2D waves

As described in [90], FHN system in two spatial dimensions

$$\frac{\partial u}{\partial t} = f(u,v) + D\frac{\partial^2 u}{\partial x^2} + D\frac{\partial^2 u}{\partial y^2}, \tag{1}$$

$$\frac{\partial v}{\partial t} = \varepsilon g(u,v), \tag{2}$$

can be written in polar coordinates with the variables r and φ,

$$\frac{\partial u}{\partial t} = f(u,v) + D\frac{\partial^2 u}{\partial r^2} + \frac{D}{r}\frac{\partial u}{\partial r} + \frac{D}{r^2}\frac{\partial^2 u}{\partial \varphi^2}, \tag{3}$$

$$\frac{\partial v}{\partial t} = \varepsilon g(u,v). \tag{4}$$

The curvature of pulse segments can be approximated by a section of a circle. Then, the front of the pulse segment lies at $r = R$, with R being the curvature radius. As the pulse segment is locally symmetrical in φ, $\frac{\partial^2 u}{\partial \varphi^2} = 0$ holds. The gradient of the activator $\frac{\partial u}{\partial r}$ only has considerable values at the location of the pulse segment, elsewhere $\frac{\partial u}{\partial r}$ is negligible. If the width of the pulse L is much smaller than the curvature radius R, the approximation $\frac{D}{r}\frac{\partial u}{\partial r} \approx \frac{D}{R}\frac{\partial u}{\partial r}$ is valid, and thus curved 2D wave segments can be described by the 1D approximation

$$\frac{\partial u}{\partial t} = f(u,v) + D\frac{\partial^2 u}{\partial r^2} + \frac{D}{R}\frac{\partial u}{\partial r}, \tag{5}$$

$$\frac{\partial v}{\partial t} = \varepsilon g(u,v). \tag{6}$$

A.2 Critical advection strength derived from nonlinear Eikonal equation

The nonlinear Eikonal equation is given by (see Eq. (5.21))

$$c_{\pm}^{f}(A) = \frac{1}{2}((A + c_0 + \varepsilon c_1) \pm \sqrt{(A + c_0 + \varepsilon c_1)^2 - 4\varepsilon A c_1}). \tag{7}$$

The propagation velocity $c_{+}^{f}(A)$ remains real only if the discriminant is larger than zero. Hence the limiting allowable advection strength A_{cr} is determined by

$$(A_{cr} + c_0 + \varepsilon c_1)^2 - 4\varepsilon A_{cr} c_1 = 0. \tag{8}$$

Solving Eq. (8) for A_{cr} yields

$$A_{cr}^{\pm} \;=\; -(c_0 - \varepsilon c_1 \pm 2\sqrt{-c_0 \varepsilon c_1}). \tag{9}$$

The critical advection strength A_{cr} is A_{cr}^{-}, because $|A_{cr}^{+}| > |A_{cr}^{-}|$.

A.3 Calculating $c^f|_{A=0}$ and $c^s|_{A=0}$ using a singular perturbation theory

As propsed in [78], singular perturbation theory is used to find an approximation for the propagation velocity of the fast wave $c^f|A = 0$ and the slow wave $c^s|A = 0$. Since ε is a small parameter, the velocities $c^f|A = 0$, $c^s|A = 0$ and the profiles of the activator $u(\xi)$ and the inhibitor $v(\xi)$ can be represented as power series in ε and $\sqrt{\varepsilon}$ respectively.

A.3.1 Fast wave velocity $c^f|_{A=0}$

In power series of ε, $c^f|_{A=0}$,$u(\xi)$ and $v(\xi)$ read

$$\begin{aligned} c^f|_{A=0} &\approx c_0 + \varepsilon c_1^f + \varepsilon^2 c_2^f + \mathcal{O}(\varepsilon^3), && (10)\\ u(\xi) &\approx u_0(\xi) + \varepsilon u_1(\xi) + \varepsilon^2 u_2(\xi) + \mathcal{O}(\varepsilon^3), && (11)\\ v(\xi) &\approx v_0(\xi) + \varepsilon v_1(\xi) + \varepsilon^2 v_2(\xi) + \mathcal{O}(\varepsilon^3). && (12) \end{aligned}$$

Substituting this expressions into Eqs. (5.3),(5.4) and equating terms with the same power series of ε gives in zeroths and first order

$$\begin{aligned} D\frac{\partial^2 u_0}{\partial \xi^2} - c_0 \frac{\partial u_0}{\partial \xi} + f(u_0) = v_0, && (13)\\ c_0 \frac{\partial v_0}{\partial \xi} = 0, && (14)\\ D\frac{\partial^2 u_1}{\partial \xi^2} - c_0 \frac{\partial u_1}{\partial \xi} + \frac{\partial f}{\partial u}|_{u=u_0} u_1 = v_1 + c_1^f \frac{\partial u_0}{\partial \xi}, && (15)\\ c_0 \frac{\partial v_1}{\partial \xi} = u_0, && (16) \end{aligned}$$

with $f(u) = 3u - u^3$.

For $c_0 \neq 0$, $v(\xi) = const.$ Thus, Eq. (13) equals the so-called Schlögl-equation, which has an exact analytical solution.

For $u_2^* < \frac{u_1^* + u_3^*}{2}$ with u_1^*, u_2^* and u_3^* being the intersection points of the u-nullcline with the inhibitor fixpoint $v_0 = -3\beta + \beta^3$, $u_1^* = -\beta$, $u_2^* = \frac{\beta}{2} - \sqrt{3 - 3/4\beta^2}$, and

$u_3^* = \frac{\beta}{2} + \sqrt{3 - 3/4\beta^2}$, and with the boundary conditions $u_0(-\infty) = u_1^*$, $u_0(\infty) = u_3^*$, Eq. (13) describes a wave front that propagates to negative x-direction, with the profile

$$u_0(\xi) = \frac{u_1^* + u_3^*}{2} + \frac{u_1^* - u_3^*}{2} \tanh\Bigg(\sqrt{\frac{1}{2D}}\Big(\frac{u_1^* - u_3^*}{2}\Big)\xi\Bigg). \tag{17}$$

From multiplying Eq. (13) with $\frac{\partial u_0}{\partial \xi}$ and integrating over ξ follows

$$c_0 \quad = \quad \frac{\int_{u_1^*}^{u*3} f(u_0)\mathrm{d}u_0}{\int_{-\infty}^{\infty}\left(\frac{\partial u_0}{\partial \xi}\right)^2 \mathrm{d}\xi}. \tag{18}$$

This yields

$$c_0 \quad = \quad \sqrt{\frac{D}{2}}(u_1^* + u_3^* - 2u_2^*). \tag{19}$$

To calculate c_1^f, Eq. (15) is analyzed. The parameter c_1 is an eigenvalue. Since $\frac{\partial u_0}{\partial \xi}$ is an eigensolution of the corresponding homogeneuos equation, the right hand side is subject to the orthogonality condition

$$c_1 \int_{-\infty}^{\infty} \Big(\frac{\partial u_0}{\partial \xi}\Big)^2 e^{-c_0\xi}\mathrm{d}\xi + \int_{-\infty}^{\infty} v_1 \frac{\partial u_0}{\partial \xi} e^{-c_0\xi}\mathrm{d}\xi \quad = \quad 0. \tag{20}$$

The correction to first order of ε of the propagation velocity of the inner stable fast wave solution considering solitary waves thus is

$$c_1^f \quad = \quad -\frac{\int_{-\infty}^{\infty} v_1 \frac{\partial u_0}{\partial \xi} e^{-c_0\xi}\, d\xi}{\int_{-\infty}^{\infty}\left(\frac{\partial u_0}{\partial \xi}\right)^2 e^{-c_0\xi}\, d\xi}. \tag{21}$$

v_1, the correction to first order of ε of the inhibitor concentration (inner solution) of the fast wave, can be derived from Eq. (16),

$$v_1(\xi) \quad = \quad \frac{1}{c_0}\int_{-\infty}^{\xi} (u_0(\mu) - u_0(-\infty))\mathrm{d}\mu, \tag{22}$$

$$v_1(\xi) \quad = \quad \frac{1}{c_0}(u_3 - u_1)\Bigg(\xi + \Big(\frac{\sqrt{2}}{u_3 - u_1}\ln(1 + e^{-\frac{u_3 - u_1}{\sqrt{2}}\xi})\Big)\Bigg). \tag{23}$$

A.3.2 Slow wave velocity $c^s|_{A=0}$

By checking various possibilities, one finds that the following assumptions yield reasonable reults,

$$\begin{aligned} c^s_{A=0} &\approx c^s_0 + \sqrt{\varepsilon}c^s_1 + \mathcal{O}(\varepsilon), &(24)\\ u(\xi) &\approx u_0(\xi) + \sqrt{\varepsilon}u_1(\xi) + \mathcal{O}(\varepsilon), &(25)\\ v(\xi) &\approx v_0(\xi) + \sqrt{\varepsilon}v_1(\xi) + \mathcal{O}(\varepsilon). &(26)\end{aligned}$$

We know, that $c^s_0 = 0$ (critical nucleus solution of Schlögl model has velocity zero). Substituting this expressions into Eqs. (5.3),(5.4) and equating terms with the same power series of $\sqrt{\varepsilon}$ gives

$$D\frac{\partial^2 u_0}{\partial \xi^2} + f(u_0) = v_0, \tag{27}$$

$$D\frac{\partial^2 u_1}{\partial \xi^2} + \frac{\partial f}{\partial u}|_{u=u_0}u_1 = v_1 + c^s_1\frac{\partial u_0}{\partial \xi}, \tag{28}$$

$$c^s_1\frac{\partial v_1}{\partial \xi} = u_0 + \beta. \tag{29}$$

To solve this for c^s_1, an orthogonality condition on the right hand side of Eq. (28) has to be imposed (this is possible, as the homogeneous equation corresponding to Eq. (28) has $\frac{\partial u_0}{\partial \xi}$ as a solution), and v_1 has to be replaced by integration of Eq. (29). This yields

$$(c^s_1)^2 = \frac{\int_{-\infty}^{\infty} u_0^2 \mathrm{d}\xi}{\int_{-\infty}^{\infty}\left(\frac{\partial u_0}{\partial \xi}\right)^2 \mathrm{d}\xi}. \tag{30}$$

The positive value of the square root should be used, thus

$$c^s_1 = \sqrt{\frac{2\sqrt{2m} - 2l\ln\alpha}{\frac{(2m)^{(3/2)}}{3} - \frac{l^2}{2}\sqrt{2m} + \frac{l(l^2-2m)}{2}\ln\alpha}}, \tag{31}$$

where $\alpha = \sqrt{\frac{l+\sqrt{2m}}{l-\sqrt{2m}}}$ and $l = \frac{2}{3}(-2u_1 + u_2 + u_3)$ and $m = (u_2 - u_1)(u_3 - u_1)$. For details, see [78].

A.4 Toroidal coordinates

A parametrization $f : \{\alpha^i\} \mapsto \{x^j\}$ gives the Laplace-Beltrami operator in curvilinear coordinates

$$\mathbf{\Delta}_{LB} \quad = \quad \sum_{i,k} \frac{1}{\sqrt{g}} \frac{\partial}{\partial \alpha^i} \left(g^{ik} \sqrt{g} \frac{\partial}{\partial \alpha^k} \right), \tag{32}$$

where $\mathbf{G}$ is the metric tensor with matrix elements g_{ik}, which is the product of the transposed Jacobian matrix of f multiplied with the Jacobian matrix of f, and $g = \text{Det}\,\mathbf{G}$, see [89]. The single components of the metrical tensor thus are the scalar product

$$g_{ik} \quad = \quad \sum_j \frac{\partial f_j}{\partial \alpha^i} \frac{\partial f_j}{\partial \alpha^k} =: \left\langle \frac{\partial f}{\partial \alpha^i} \mid \frac{\partial f}{\partial \alpha^k} \right\rangle. \tag{33}$$

A parametrization f is isothermal, if the derived coordinate system is orthogonal and conformal. In two spatial dimensions, a parametrization

$$f : (\alpha^1, \alpha^2) \quad \mapsto \quad \begin{pmatrix} x \\ y \\ z \end{pmatrix} \tag{34}$$

is orthogonal, if the scalar product of the basis vectors for $i \neq k$ equals zero,

$$\left\langle \frac{\partial f}{\partial \alpha^i} | \frac{\partial f}{\partial \alpha^k} \right\rangle \quad = \quad 0. \tag{35}$$

The condition for conformal mapping is

$$\left\langle \frac{\partial f}{\partial \alpha^i} | \frac{\partial f}{\partial \alpha^i} \right\rangle \quad = \quad \left\langle \frac{\partial f}{\partial \alpha^k} | \frac{\partial f}{\partial \alpha^k} \right\rangle, \tag{36}$$

see [89].
This yields the following form of the Laplace-Beltrami operator

$$\mathbf{\Delta}_{LB} \quad = \quad \sum_{i,k} \frac{1}{\sqrt{g}} \frac{\partial}{\partial \alpha^i} \frac{\partial}{\partial \alpha^k} \delta^{ik} = \frac{1}{\sqrt{g}} \nabla^2. \tag{37}$$

To derive a global isothermal coordinate system for the surface of a torus, we start from the parametrization [91]

$$(\theta_i, \varphi) \quad \mapsto \quad \begin{pmatrix} \frac{a \sinh \eta \cos \varphi}{\cosh \eta - \cos \theta_i} \\ \frac{a \sinh \eta \sin \varphi}{\cosh \eta - \cos \theta_i} \\ \frac{a \sin \theta_i}{\cosh \eta - \cos \theta_i} \end{pmatrix} = \begin{pmatrix} x \\ y \\ z \end{pmatrix}, \tag{38}$$

where $a > 0$ is a scaling factor of space and $\eta > 0$ is a measure for the ratio of major curvature radius R and minor curvature radius r. As can easily be proved, these are orthogonal coordinates.
As

$$g_{\theta_i\theta_i} = \frac{a^2}{(\cosh\eta - \cos\theta_i)^2}$$

and

$$g_{\varphi\varphi} = \frac{a^2\sinh^2\eta}{(\cosh\eta - \cos\theta_i)^2},$$

$g_{\theta_i\theta_i} \neq g_{\varphi\varphi}$, thus the parametrization Eq. (38) is not conformal. Introducing the variable

$$\tilde{\varphi} = \varphi\sinh\eta$$

yields

$$g_{\tilde{\varphi}\tilde{\varphi}} = g_{\theta_i\theta_i} = \sqrt{g} = \frac{a^2}{(\cosh\eta - \cos\theta_i)^2}. \tag{39}$$

Thus the Laplace-Beltrami operator in isothermal torus coordinates reads

$$\mathbf{\Delta}_{LB} = \frac{(\cosh\eta - \cos\theta_i)^2}{a^2}\left(\frac{\partial^2 u}{\partial\theta_i^2} + \frac{\partial^2 u}{\partial\tilde{\varphi}^2}\right). \tag{40}$$

To obtain the dependencies of a and η upon the major curvature radius R and the minor curvature radius r, which are parameters of the common parametrization

$$(\theta, \varphi) \mapsto \begin{pmatrix} (R + r\cos\theta)\cos\varphi \\ (R + r\cos\theta)\sin\varphi \\ r\sin\theta \end{pmatrix} = \begin{pmatrix} x \\ y \\ z \end{pmatrix}, \tag{41}$$

one needs to compare Eq. (41) with the isothermal parametrization

$$(\theta_i, \tilde{\varphi}) \mapsto \begin{pmatrix} \frac{a\sinh\eta\cos(\frac{\tilde{\varphi}}{\sinh\eta})}{\cosh\eta - \cos\theta_i} \\ \frac{a\sinh\eta\sin(\frac{\tilde{\varphi}}{\sinh\eta})}{\cosh\eta - \cos\theta_i} \\ \frac{a\sin\theta_i}{\cosh\eta - \cos\theta_i} \end{pmatrix} = \begin{pmatrix} x \\ y \\ z \end{pmatrix}. \tag{42}$$

A necessary and sufficient condition that a point from the domain of definition of the parametrization Eq. (41) lies on the twodimensional surface of a torus in the Euclidian $\mathbb{R}^3$ is

$$\left(\sqrt{x^2 + y^2} - R\right)^2 + z^2 - r^2 = 0. \tag{43}$$

In toroidal coordinates, Eq. (42) yields

$$x^2 + y^2 + z^2 - 2a\frac{\cosh\eta}{\sinh\eta}\sqrt{x^2+y^2} + a^2 \quad = \quad 0. \tag{44}$$

By comparing the coefficients, one obtains from Eqs. (43) and (44)

$$\begin{aligned} R &= a\frac{\cosh\eta}{\sinh\eta} = a\coth\eta, &(45)\\ r &= a\frac{1}{\sinh\eta}, &(46)\end{aligned}$$

and the inverse relations

$$\begin{aligned} a &= \sqrt{R^2-r^2}, &(47)\\ \eta &= \operatorname{arcoth}\frac{R}{\sqrt{R^2-r^2}} = \operatorname{arcoth}\frac{n}{\sqrt{n^2-1}}, &(48)\end{aligned}$$

where $n = \frac{R}{r}$.
As can be seen from the parametrizations Eqs. (41) and (42), the transformation $\tilde{\varphi}(\varphi)$ is

$$\tilde{\varphi}(\varphi) \quad = \quad \varphi\sinh\eta. \tag{49}$$

To derive the dependency between θ_i and θ, the expressions $\sqrt{x^2+y^2} - R$ of both coordinate systems are compared. This yields

$$r\cos\theta \quad = \quad a\frac{\sinh\eta}{\cosh\eta - \cos\theta_i} - R. \tag{50}$$

Replacing R and r with Eqs. (45) and (46), this yields

$$\theta \quad = \arccos\left(\tfrac{\cosh\eta\cos\theta_i - 1}{\cosh\eta - \cos\theta_i}\right)\cdot\left\{\begin{smallmatrix} +1 & \theta_i \geq 0\\ -1 & \theta_i < 0.\end{smallmatrix}\right. \tag{51}$$

The inverse function is

$$\theta_i \quad = \arccos\left(\tfrac{R}{r} - \tfrac{R^2-r^2}{r(R+r\cos\theta)}\right)\cdot\left\{\begin{smallmatrix} +1 & \theta \geq 0\\ -1 & \theta < 0.\end{smallmatrix}\right. \tag{52}$$